PROCESS DEVELOPMENT FOR THE PRODUCTION OF

OPTICALLY TRANSPARENT MICRO-FEATURES

A Thesis
Presented to
The Academic Faculty

by

Nishant Srinivasan

In Partial Fulfillment
of the Requirements for the Degree
Master of Science in the
G. W. Woodruff School of Mechanical Engineering

Georgia Institute of Technology
August 2015

PROCESS DEVELOPMENT FOR THE PRODUCTION OF

OPTICALLY TRANSPARENT MICRO-FEATURES

Approved by:

Dr. J. Rhett Mayor, Advisor
G. W. Woodruff School of Mechanical
Engineering
Georgia Institute of Technology

Dr. Jonathan S. Colton
G. W. Woodruff School of Mechanical
Engineering
Georgia Institute of Technology

Dr. Christopher J. Saldana
G. W. Woodruff School of Mechanical
Engineering
Georgia Institute of Technology

Date Approved: 04/17/2015

ACKNOWLEDEGMENTS

TABLE OF CONTENTS

LIST OF TABLES

LIST OF FIGURES

SUMMARY

The emergence of biofluidics devices and "Lab-on-a-Chip" testing platforms has resulted in a need for the low cost production of optically transparent micro-features. The goal of the study was to develop a process to fabricate optically transparent microfeatures. Two biofluidics chips were used as a case study to explore possible production pathways. The process developed was used for low unit production, but also provided a stepping stone for high volume production. The goal was accomplished by exploring two phases of the manufacturing process: Tool production and casting. Micro-feature tool production was explored through the micro-machining of mold cavities and surface enhancement using electrochemical polishing techniques. A computational model was developed to predict material removal rates of the electropolishing process and optimize process parameters. The candidate parts were fabricated and replicated through low pressure casting with the machined micro-molds. The process provided insight to the feasibility of injection molding of the two candidate devices. The knowledge gained from this study will act as a stepping stone to aid in developing techniques for the mass production of optically transparent micro-features.

CHAPTER 1

INTRODUCTION

1.1 Emergence of Microfeature Production

The miniaturization of products has been occurring over a large spectrum of industries over the past decade. Consequently, the necessity to produce features on the microscale has become vital to the product development process for the consumer electronic, biomedical, and optical industries. Microfeatures provide an array of benefits ranging from exponential increases in surface area to aid in thermal management, to the ability to interact with biological mechanisms on a cellular level [1, 2]. As microfeatures become better integrated into products, the necessity to research and improve aspects of the product development processes to aid in the manufacturing of these microfeatures increases dramatically. In particular, optically transparent microfeatures have emerged as a need in optical and biomedical industries.

1.2 Optically Transparent Microfeatures

1.2.1   Industry Needs and Uses

Optically transparent microfeatures have been in popular demand recently. In the optical industry, micro-lenses are needed for an array of applications. For example, fiber optic cables utilize internal reflection and precise lens arrays to transmit light over long distances. The benefits include faster data transfer rates and smaller sized cable bundles as compared to standard copper wires. Recently, fiber optics cables use transparent lenses with diameters as small as 27 μm to transmit high fidelity data at high rates [3]. In addition to fiber optics, optically transparent materials were also used to develop the first

telescopic contact lens to aid the visually impaired [4]. Transparent channels and pores were embedded in the lens to allow for a 2.8x magnification for the user. Images of the two examples are shown below in Figure 1.1 [5].
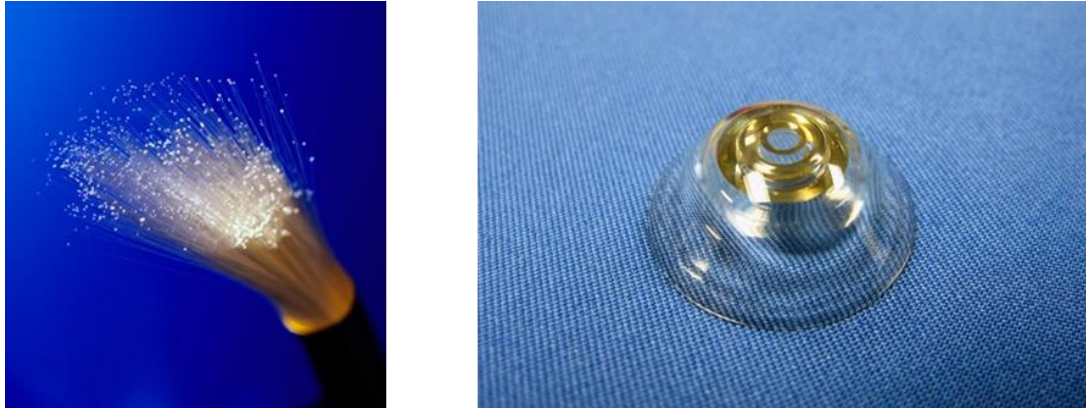
Figure 1.1: Fiber optic cables and telescopic lenses are emerging uses of optically transparent microfeatures.

In addition to the optical industry, the biomedical industry has been reliant on manufacturing optically transparent microfeatures to aid in testing microfluidics. Microfluidics devices have provided the ability to perform dispensable ubiquitous testing for an array cellular deficiencies and diseases. By having transparent microfeatures, scientists can observe cellular reactions and mechanisms during testing. An example of a microfluidics device is shown below in Figure 1.2 [6].
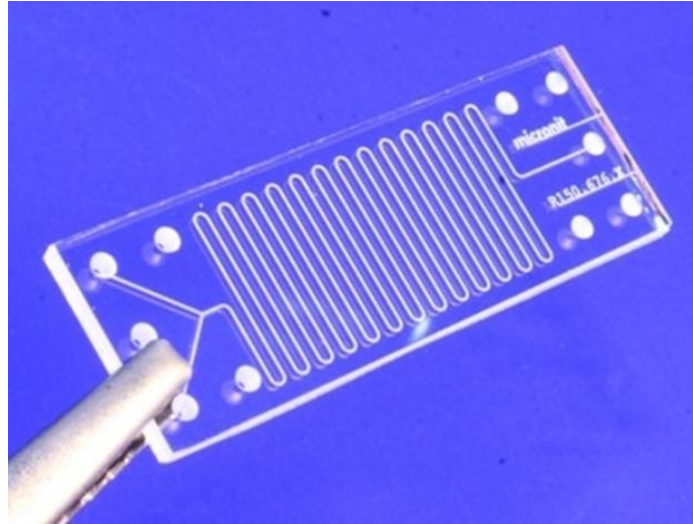
Figure 1.2: Lab-on-a-chip devices utilize optically transparent microfeatures to allow for visual inspection of microfluidic channels.

In particular, lab-on-a-chip (LOC) devices have been able to integrate one or more laboratory tests or functions within a palm sized chip measuring several square centimeters. The small chip size allows for low fluid consumption and waste, faster analysis, and the ability to perform tests out in the field in non-laboratory environments. Examples of LOCs include microbial detection devices, thrombosis formation tests, and intracellular medication devices [7-9]. Challenges involved with LOCs primarily revolve around the physical and chemical effects that occur on the microscale. The sensitivity to capillary forces, surface roughness and chemical reactions are magnified at the microscale and provide design, manufacturing, and testing challenges.

1.2.2 Challenges with Optically Transparent Materials

While creating microfeatures is a challenge in and of itself, fabricating optically transparent microfeatures is even tougher due to material constraints. The two most common optically clear materials are glass and various types of plastic. Glass is a difficult material to create microfeatures out of due to its brittleness. It is difficult to

machine as it fractures easily, and is very difficult to thermoform as it has an extremely high glass transition temperature (1475 K) [10]. Plastic on the other hand is quite ductile compared to glass or metals. Thus, machining plastic is also difficult as it is tough to form clean chips while cutting due to increased chip formation energy caused by heat generation from the tool. The stress stain curve of glass, metal and polymers are shown below in Figure 1.3, and illustrate the challenges of machining optically transparent materials [10].
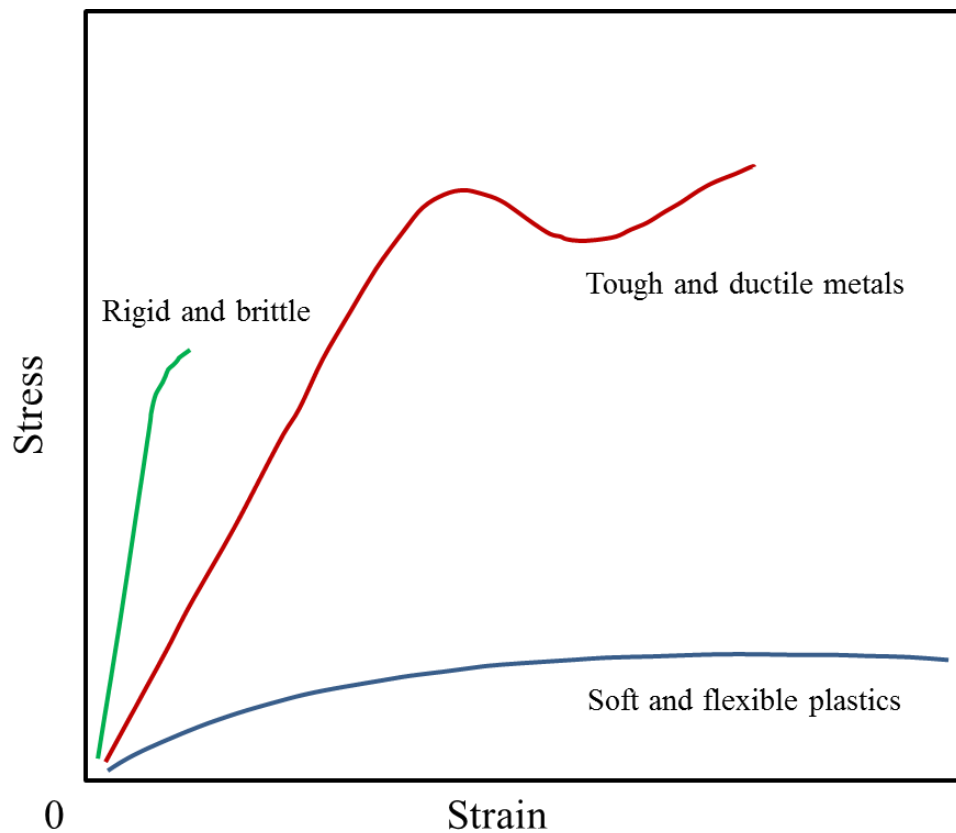
Figure 1.3: The stress-strain curves for optically transparent materials are predominantly represented by rigid brittle materials (glass) or soft flexible plastics.

In addition to creating geometries in optically transparent materials, the material must maintain clarity after the fabrication process. Thus, surface roughness is an important

factor as smoother surfaces will promote better optical clarity. If traditional machining processes are used, the part can be polished after the cutting process. If the part is molded, only the master mold needs to be polished as the cast parts will replicate the mold's surface. Polishing parts and reducing surface roughness is not an issue with macroscopic parts and features, but with delicate microfeatures it is a challenge to polish without damaging the microfeatures. Traditional mechanical polishing techniques such as buffing, tumbling, and lapping are not viable as they cannot polish in between microgrooves and microchannels, and they can mechanically deform the delicate microfeatures. Thus, a passive more gentle approach towards reducing surface roughness is needed. Techniques such as abrasive slurries, ultrasonic polishing and electrochemical polishing can be used to reduce surface roughness without excessive mechanical force.

1.3 Manufacturing Microfeatures

Introducing microfeatures to conventional manufacturing processes has been a pressing challenge in recent years, and is currently being explored to speed up, reduce costs, and improve the accuracy of the fabrication of microfeatures. Fabrication techniques can be divided up into two types, high volume and low volume processes. Low volume processes typically revolve around direct material removal from a stock piece of material. These processes are typically reserved for early stage prototyping as they are cheap and quick to implement. High volume processes are often based on creating a master mold to replicate the geometry thousands of times. While the initial cost of implementing high volume processes are expensive, they encounter cost savings from small wastage per part, and fast processing time per part.

1.3.1 Low Volume Processes

Typical methods utilized include material removal techniques such as micro-milling and micro-turning as well as non-mechanical techniques such as laser ablation. The primary drawback of these processes is that they do not scale efficiently for mass production as their process time and cost per part is quite high.

Micro-milling utilizes the same processes that standard conventional milling uses with the difference residing in the size of the tool. Endmills with diameters below 1 mm are considered micro-endmills. These tools are typically constructed out of tungsten carbide and can reach sizes as small as 5 μm in diameter. The process can be time consuming as well as expensive, as micro-tools are fragile and expensive. An example of a micromill and micromachined parts is shown below in Figure 1.4.
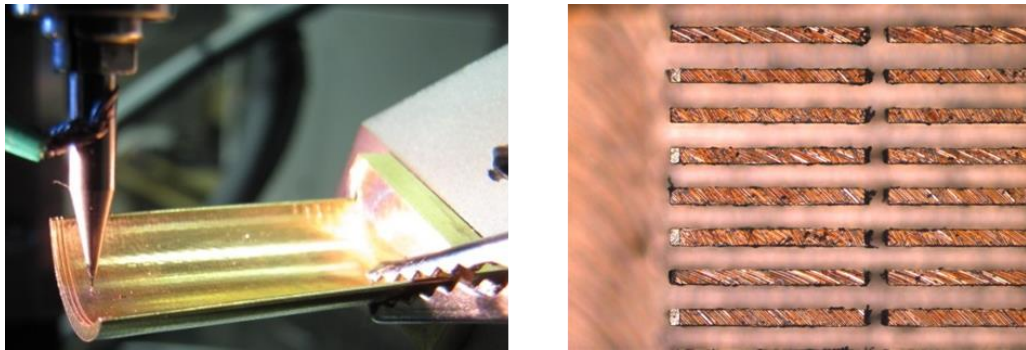
Figure 1.4: High speed High precission Micromilling machine at MAYORLab (Left). 100 μm wide microchannels with 10:1 aspect ratio machined using micromill (Right).

Laser ablation utilizes high powered lasers to etch and breakdown plastics. While the lasers retain extremely high precision and accuracy, they are very expensive and have long process times. In many ways the process is very similar to micromilling, but through a different medium.

1.3.2 High Volume Processes

For high volume production, injection molding is a common method used for polymers. Injection molding involves melting a plastic pellets and injecting the molten plastic into a mold cavity. Once the plastic cools, the mold is opened and the part is removed. The primary benefit of injection molding resides in its low process time and low cost per unit [11]. With the ability of casting multi-cavity molds, numerous parts can be fabricated simultaneously without significant wastage. Also, the process only requires one step to convert plastic pellets into the final part, as illustrated by the process chain shown below in Figure 1.5.

Figure 1.5: The process chain for injection molded parts converts plastic pellets to final parts in one step. Image on bottom is the Sumitomo SH75 injection molding machine in the Manufacturing Research Center at Georgia Tech.

Hot embossing is an alternative forming method that can be used to form plastic parts in high-volume. The process involves heating a thin polymer just above its glass

transition point and stamping it with a mold to form a shape. When compared to milling and laser ablation, the process time for hot embossing is much less, making it much more suitable for mass production (2-5 minutes) [12]. However, when compared to injection molding, hot embossing is not as efficient of a process as the process chain is longer and more waste is produced. This can be seen in Figure 1.6, where a rolling and cutting process is necessary for from the final part. Injection molding on the other hand takes plastic pellets and forms the final part in one step. Thus it can be deduced that injection mold contains the shortest process chain and would provide a reduction in energy at high volumes when compared to other manufacturing processes.
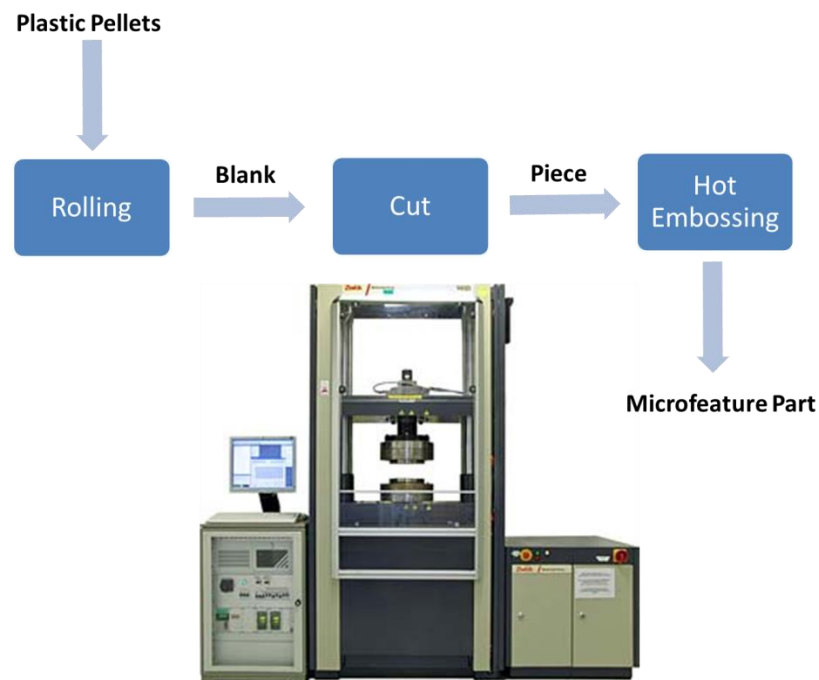
Figure 1.6: The process chain for hot embossing requires the extra steps of creating of individual pieces to be embossed. The image on the bottom is of a hot embossing machine at Karlsrhue Institute of Technology.

Challenges involved with injection molding and hot embossing lie in the fabrication of the complex micro-molds, as well as the finishing and polishing processes used to

improve the surface roughness of the delicate microfeatures. Obtaining a smooth mold surface leads is vital to achieving a cleaner and smoother surface finish for the final product. Exploring and understanding process parameters attributed to micromachining and injection molding is crucial to enabling high volume production of microfeature components.

1.4 High Volume Process Plan

A preliminary fabrication study was performed to explore the possibility of direct machining plastic to create the parts quickly. Details regarding the preliminary fabrications study can be found in Appendix A. Results showed that prototyping plastic parts through direct machining proved futile as geometric dimensions and optical transparency could not be maintained. Thus, the direct machining plastic of was not a viable solution for low scale or large volume production. Results of machining the microfeature geometry directly into plastic and brass are shown below in Figure 1.7.
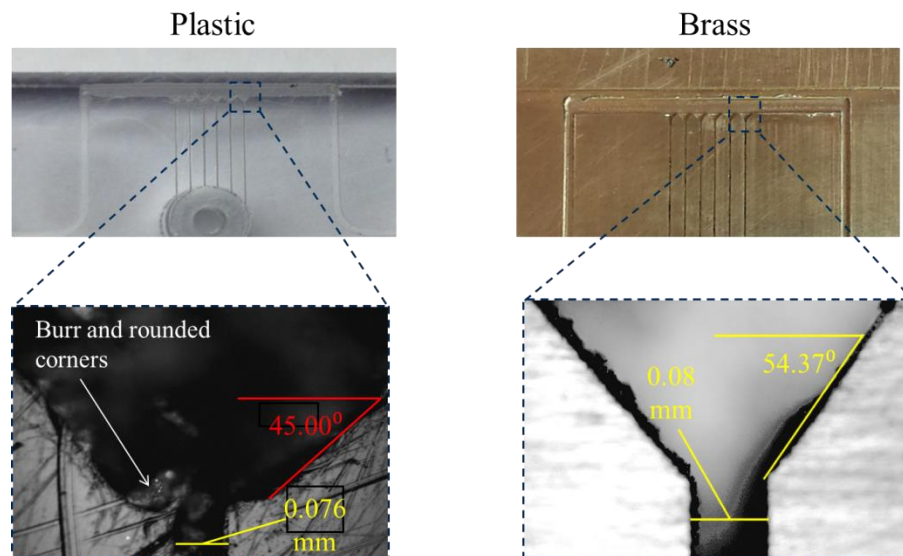
Figure 1.7: Direct machining plastic resulted in poor surface finish, incorrect dimensions (nozzle angle) and burr. The same geometry was machined in brass with cleaner straighter edges, along with correct dimensions.

Injection molding provides the shortest process chain for high volume production and will be utilized to mass produce the part. In order to mold the part, a mold cavity must first be machined. While machining plastic was difficult, machining brass yielded positive results. Thus, machining a microfeature mold is a possible pathway for high volume production. The proposed process chain is displayed below in Figure 1.8.
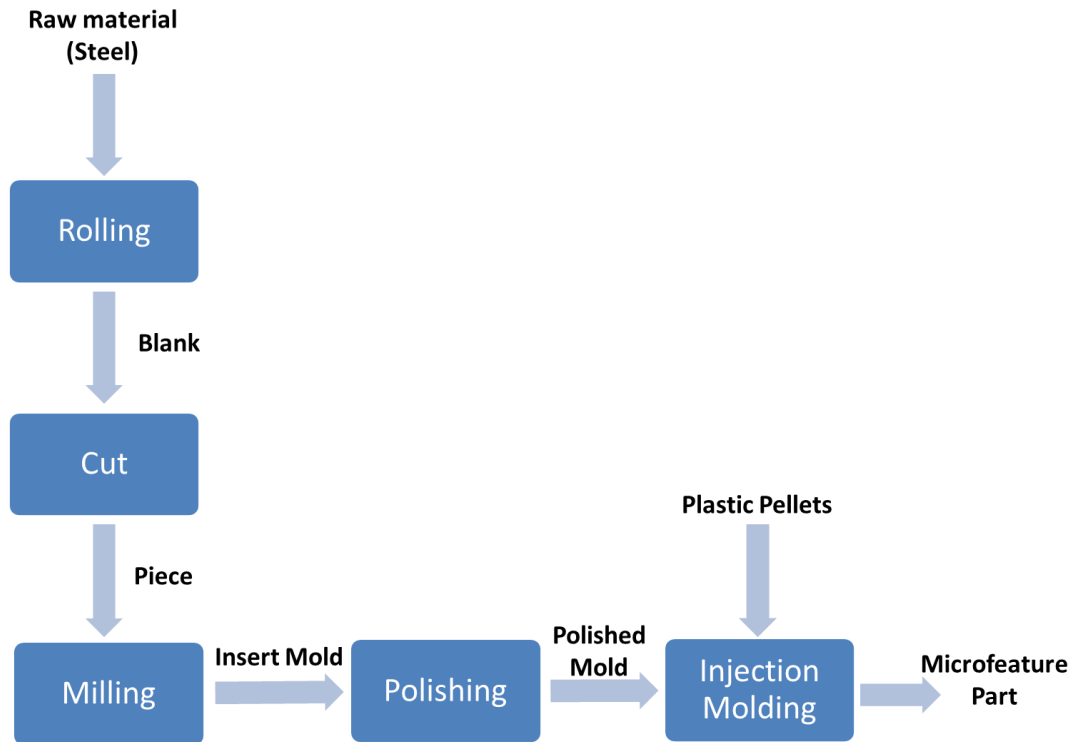
Figure 1.8: The process chain developed to manufacture optically transparent microfeatures utilizes the machining of a micromold to enable injection molding of the desired part.

In order to prove feasibility of injection molding, low pressure casting was attempted to act as a stepping stone and a proof of concept for high volume manufacturing as well as provide low cost prototype parts for testing. The challenges involved with low pressure casting will be that actual fabrication of the mold (geometric tolerances),

polishing the delicate microfeatures, and determining the process parameters necessary to achieve a repeatable robust process yield for a low unit production.

1.5 Case Study: Biofluidics MEMS transfection Device

The candidate device in this study is an acoustically controlled cell transfection device. Cell transfection is the process of introducing media, such as nucleic acids, into cells. The MEMS device performs this action by using ultrasonic vibrations to force cells through nozzles [9]. During the process, the cell walls will open, allowing for media to be placed inside the cell. Once the cell exits the orifice of the nozzle, the cell wall will close with the media inside of it. The device can allow for certain treatments such as medicine to help treat disease or any cellular deficiencies. An illustrated concept of the device is shown below in Figure 1.9 [13].
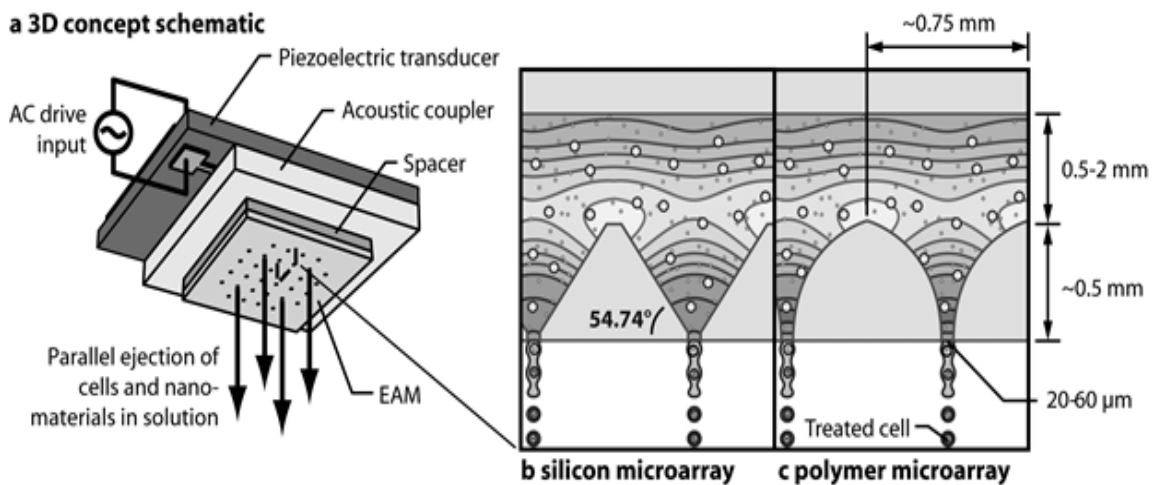
Figure 1.9: Concept of cell transfection device depicting micro-nozzle array.

The microarray consisted of nozzles that were 0.5 mm tall with 0.750 mm openings and 0.02 mm-0.06 mm orifices. Previously, the component was made out of silicon. In order to scale for mass production, the component was to be made out of an optically transparent, biocompatible material. Two different versions of the microarray were to be

made and fabricated out of a transparent plastic: A 2D nozzles array and a 3D nozzle array.

1.5.1 Part 1: 2D Feature Array

The overall dimensions of 2D array component are 50 mm long, 20 mm tall, and 11 mm thick. The microarray is a set of nozzles comprised of triangular and prismatic geometries. The nozzle array is depressed 0.2 mm deep on the front face of the piece. The array is a repeated set of 0.75 mm wide by 0.5 mm tall triangles with a 0.08 mm - 0.1 mm wide channel stemming from the tip of the triangle. In addition to the nozzle array are two larger 0.50 mm wide channels that curve up and connect to the nozzles. The biofluidics chip is depicted below in Figure 1.10.
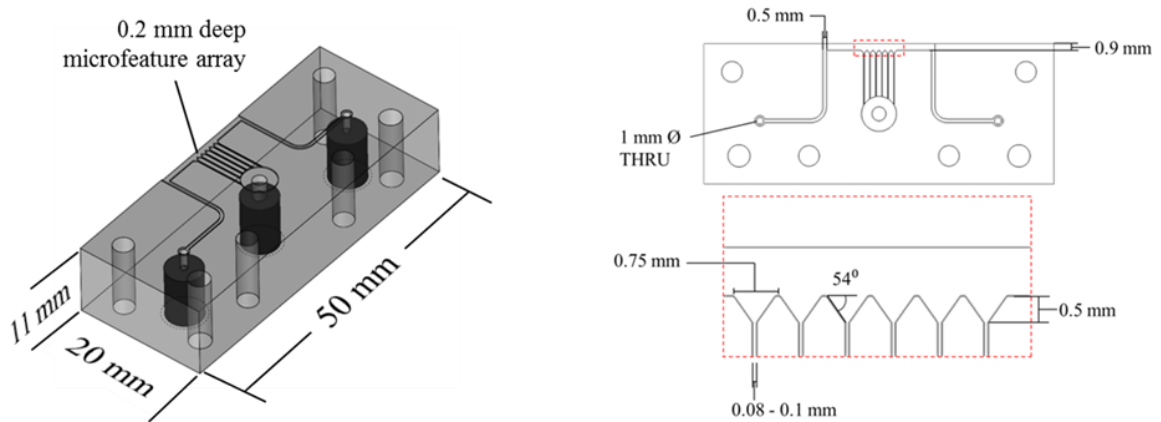
Figure 1.10: The transparent biofluidics chip to be made is 11mm thick and has a 0.2 mm deep microfeature array comprised of prismatic triangles and channels.

The major constraint of the part was that it had to be transparent. Transparency was required to allow for visual inspection through a microscope from the backside of the part. Visual inspection involved viewing the fluid flow through the channels as well as monitoring cell as they travel through the nozzles. Optical transparency was defined by

visibility of the features. If the microfeatures were visible from the backside through a microscope, the part was deemed transparent. The setup for the testing of the part is illustrated below in Figure 1.11.
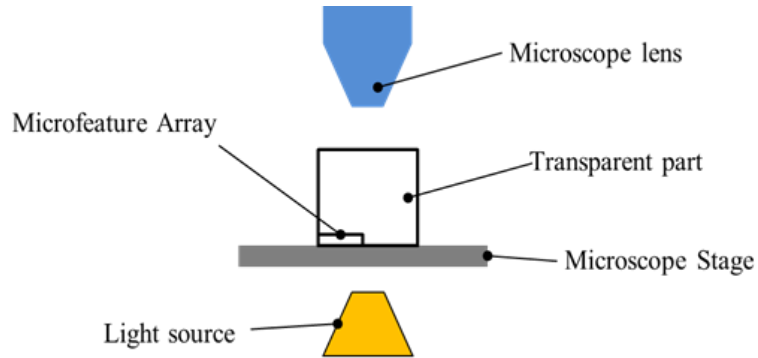
Figure 1.11: The chip is placed face down on the microscope stage and viewed through the back side through the microscope lens.

1.5.2   Part 2: 3D nozzle array

The second microfeature component was the 3D nozzle array. The overall dimensions of the part were 7 mm x 7 mm x 0.5 mm. The nozzles were conical instead of triangular prisms. The nozzles were 0.5mm tall with an opening diameter of 0.750 mm and orifices no larger than 0.05mm in diameter. The array was comprised of 31 nozzles and was to be inserted into a cartridge for testing. The 3D micronozzle part is depicted below in Figure 1.12.
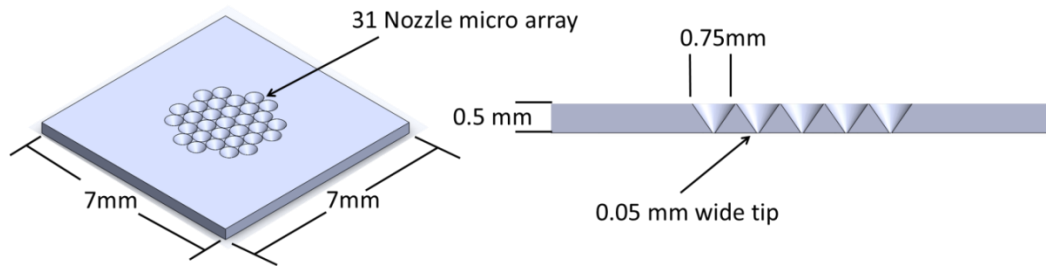
Figure 1.12: The 3D nozzle part was comprised of 31 micronozzle on a chip only 0.5 mm thick.

CHAPTER 2

LITERATURE REVIEW

2.1 Introduction

The ability to produce microfeatures in optically transparent materials is a unique manufacturing challenge present in the biofluidics and optics communities. While fabricating microfeatures in any material is an arduous task, the characteristics of optically transparent materials make creating the microfeatures even more difficult than compared to soft metals. As discussed in the introduction, the direct machining of optically transparent materials with high precision is a difficult task, specifically at the micro-scale. Thus, in order to effectively mass produce optically transparent microfeatures, casting techniques such as injection molding are to be explored. This work presents an exploration and analysis on the feasibility of mass production of optically transparent microfeatures. This is accomplished by investigating micro-machining mold cavities, delicate polishing techniques, and low-pressure casting in order to fabricate a biofluidics device.

The following sections present existing literature regarding fundamental research and development of techniques used to fabricate microfeatures into optically transparent materials as well as delicate and passive polishing techniques for microfeatures.

2.2 Fabrication of Transparent Microfeatures

2.2.1   Soft lithography and wet chemical etching

Casting micro-features is a common method for fabricating as it allows for replicability. The process of casting microfeatures is primarily comprised of two key aspects: Fabricating a mold cavity, and casting a polymer.

Fabricating a mold cavity for macroscopic features is often times performed using conventional milling techniques or electron discharge machining (EDM). At the microscale it is not so simple. To mill microfeatures with enough fidelity and strength to cast materials is difficult. To counter this, soft lithography has been a commonly used technique in the microfluidics world to replicate micro-features [14]. The process involves utilizing a master mold to replicate elastomeric microfeatures. The master mold is created using photolithography of wet chemical etching techniques. The molds are often fabricated out of thin layers silicon-oxide. A mask with a pattern is placed on top of the silicon-oxide layer while a photo-activated etching agent is used to carve away the unmasked parts of the silicon-oxide (SiO_2). While the SiO_2 material is quite expensive, the etching process is a low cost procedure that can yield very accurate features.

In 2005, Mills was able to create rectangular channels as narrow as 2 μm in silicon-oxide utilizing wet chemical etching [15]. The etched silicon oxide acted as a master mold to imprint polylactic acid (PLA), and successfully transferred the geometry from the to the cast resin. Microchannels from 2.5 μm to 40 μm wide and 5 μm to 0.35 μm were fabricated in PLA. The work was performed on thin plastic sheets 125 μm thick. While the process presented can fabricate very narrow channels accurately, it is limited to thin plastic sheets as the workpiece.

In 2009, Friend developed ways to cast PDMS specifically for microfluidics devices [16]. The benefits of using PDMS are that it is optically transparent, very viscous (fill mold cavities and reduce bubble propagation), and is hydrophobic which reduces adhesion and aids in flow properties. The process simply states that PDMS can be mixed and poured into the mold. Also stated is the process of degassing in vacuum chamber to

aid in the removal of bubbles and voids. The cast part is released by peeling the PDMS part out of the mold. This is possible because of the low elastic modulus of PDMS (1.4 GPa) [17]. Friend's work focuses primarily on casting PDMS which is a relatively soft and rubbery polymer compared to acrylic and polycarbonate. Thus, the mold ejection process for stronger polymers, specifically for micro-casting, is more difficult, as the material is not as compliant and can fracture.

Hug utilized both photolithography etching techniques and casting PDMS to create transparent microfluidic channels used to make atomic force microscope (AFM) cantilevers [18]. Channels with heights and widths as small as 140 μm long, 4 μm wide and 3.4 μm tall were etched into a SiO_2 sheet. The mold was pretreated with oxygen plasma to enhance the bonding interaction between the PDMS resin and the mold. A single SiO_2 sheet could produce 160 AFM cast cantilevers. Although the work presented a possibility of high volume production through the casting of micro-mold, it did so casting PDMS, a soft polymer rather than a rigid polymer such as PMMA or polycarbonate.

Vivanco utilized micro milling techniques to machine micro-feature molds to cast bone scaffolds [19]. Features with dimensions as small as 500 μm were machined into 6061 aluminum. PDMS resin was pours into the mold and allowed to cure. The total thickness of the cast parts were 1 mm.

2.2.2 Alternative manufacturing methods

Besides casting, several forming and direct machining methods have been explored to fabricate microfeatures in polymers and glass. Hot embossing is a common method that

has successfully been implemented in creating microfeatures in optically transparent materials.

In 2004, Wang was able to combine precision automation and alignment equipment to emboss hard plastics such as polymethlymethacrylate (PMMA) [20]. Wang was able to create micro-features with 1 μm of accuracy, but only did so on plastic films of 200 μm. While this work is scalable for mass production, the process was only operable on thin films. The candidate parts fabricated for this study are much thicker, (0.500 mm and 11 mm). The challenge of forming microfeatures on such a thick bulk surface is one of the unique challenges associated with this study.

In 2010, Iliescu used wet etching techniques to fabricate microchannels in glass specifically for a microfluidics device [21]. A silicon mask was placed ontop of the glass sheet as a template for the microchannels. He was able to create micro-channels 80 μm wide and 25 μm deep directly into glass, but the channels were left with a draft angle on each side. While providing insightful information on how to fabricate microfeatures into glass, the process used is not one that is easily scalable for mass production. Also the draft angle left from the acid etching technique is a significant concern when rectangular prismatic features are necessary.

Laser ablation is a relatively new form of manufacturing that has been trending due to the advances in laser technology. In 2006, Pfleging used Carbon Dioxide lasers to micro-print on PMMA [22]. Microchannels with widths of 30 μm and aspect ratios up to 30 were fabricated successfully. The lasers were also used to weld components together. Welding capabilities allowed for assembly of various microchannels to create complex microfluidic channels that flow in three dimensions. While laser ablation is an effective

way to fabricate high aspect microfeatures on a bulk surface, its primary drawback is the high cost and limited scalability.

Sugioka's work in 2012 combined the use of lasers and wet chemical etching to create optically transparent microfeatures in glass [23]. A high powered femtosecond laser was used to treat the glass in specific selected areas. The glass was then subjected to a hydrofluoric acid (HF) bath that would etch only the laser treated portions of the glass. Only the laser treated portions are etched because the reaction rate occurs 50 times faster on the laser treated portions of the glass compared to untreated glass. Thus, intricate microfeatures could be traced with the femtosecond laser, and then created using the wet chemical etching techniques. Microchannels with 200 μm widths were fabricated on 2mm thick glass substrates. Several layers of etch glass were then stacked on top of each other to form three-dimensional microfluidics pathways.

2.3 Polishing micro-features

When casting polymers for high-volume production, the surface roughness of the mold plays an important factor in the outcome of the final part. In order to optimize optical clarity and surface finish of cast transparent parts, the metal mold cavity used to cast the resin should as smooth as possible because the mold surface gets replicated to the final part. Reducing surface roughness is typically is not an issue when casting macroscopic features and parts, but when dealing with an array of microfeatures, improving surface finish becomes a challenge. Mechanical polishing is not possible with microfeatures as there is often not enough space to polish in between the micro protrusions. Also applying direct force to the microfeature array could deform the

features [24]. Thus, a passive form of polishing must be utilized in order reduce the surface roughness without damaging the micro-features.

2.3.1 Methods of polishing micro-features

In 2007, Perry explored laser polishing as a method of reducing surface roughness of micro-features [25]. Nickel samples with microfeatures were fabricated using electrochemical etching techniques. An yttrium aluminum garnet (YAG) laser was used to enhance the surface roughness of the samples. By pulsing the laser for 200-300 ns bursts, surface roughness features greater than $200mm^{-1}$ in spatial frequency were removed. The laser polishing process that is presented provides a non-mechanical method of surface enhancement that does not harm microfeatures, but is not practical when dealing with large area microfeature arrays, as the focused laser does not cover large areas.

Suzuki published work in 2005 on polishing glass micro lenses using ultrasonic vibrations [26]. An ultrasonic vibrator was used to vibrate a stylus that was placed onto the workpiece. An abrasive slurry was then introduced as a medium between the stylus and workpiece to polish the surface. The workpiece was a molding die made out of tungsten carbide. The stylus was comprised of polyurethane with a radius of 250 μm. Media comprised of diamond bits with a diameter of 0.50 μm was used as the polishing agent. After polishing, the tungsten carbide workpiece's roughness profile was reduced from 30 nm Ry to 10 nm Ry. The work presents an innovative way to polish molds specifically for microfeatures, but is limited by the diameter of the stylus.

2.3.2 Electrochemical Polishing

Electropolishing is a derivative of the common process of electroplating, which is used to deposit layers of metal ions onto a surface. Both processes are based on the principle of electrochemical reactions. The reactions involve passing DC current through metal pieces submerged in an electrolytic solution. The current initiates an oxidation reduction reaction, which pulls electrons from the valence shells of the metal ions of the cathode [27]. The process causes positively charged metal ions to leave the anode.

Kim presented a method of forming disk shaped features using electrochemical techniques [28]. A stainless steel wire was used as an electrode, and was used high aspect ratio features in hard metals. By localizing the current distribution in one area, only certain parts of the workpeice were subjected to the etching. While not necessarily polishing the workpeice, the work presented a method of localizing the electrochemical reaction to gain further control of the reaction.

Jeong presented a method to deburr microfeatures utilizing a micro EDM [29]. A cylindrical tool was used to localize the reaction and polish the burr off of the micro milled features. The work showed that the high surface charge densities in the micro-burr allowed for the process to clean burr off without harming or damaging the microfeatures.

Kissling utilized electropolishing as a burr removal technique as well in 2010. High aspect ratio nickel RF systems with 10 μm features and aspect ratios up to 40 were fabricated using lithography and electroplating techniques [30]. Electropolishing with current densities of 80 A/dm were used to remove burr from the fragile elements. Edge rounding on the features was noticeable when the reaction was left to run for longer periods of time.

Gietzelt utilized electropolishing to remove burr specifically for micro-molding applications [31]. Micro-molds for the mass production of gears underwent an electropolishing process to remove burr and ultimately improve the surface finish of the tools. The molds were machined out of Corrax using 100 μm micro-endmills. After being subjected to a current density of 0.4 A for 3 min, almost all of the burr on the features was removed. Deep grooves could not be smoothed as the electrode could not fit inside the spaces. Corners and edges also experienced rounding due to prolonged exposure to the process.

2.3.3 Modeling Electropolishing

Predicting the effects of electropolishing is quite difficult as there are numerous factors that can affect the material removal rate of the process. Optimizing parameter such as voltage and electrolyte concentration varies based on the workpiece material and geometry. When dealing with micro-sized features, the sensitivity to parameter changes increases tenfold, and the ability to optimize and control parameters becomes a necessity. Thus, developing models to help predict material removal rates of electropolishing is a powerful is a powerful tool when trying to polish micro-features.

Jain used the electrochemical process as a form of machining in 2012 [32]. A 47 μm stainless steel needle was used as an electrode to localize the reaction. The localization of the reaction allowed for controlled formation of micro holes and micro channels. By running sets of experiments, a mathematical model was developed to help optimize process parameters for the reaction. The primary parameters that were studied were the voltage and electrolyte concentration. This work presents a method of process parameter optimization and control for electrochemical machining.

Bhuyan developed mathematical models to predict the material removal rates of electropolishing a stainless steel wire [33]. Models were developed from experimental testing. Parameters such as electrolyte temperature, concentration, current density, puled current, ultrasonic agitation and time were tested. Increasing temperature and concentration of the electrolyte produced smoother surfaces. Also, pulsed currents and agitation prevented pitting on the surface or the parts, and resulted in smoother surfaces.

Recently in 2014, Dickinson developed electropolishing models using COMSOL [34]. The models would account for the surface charge density in the geometry, and calculate material removal rates accordingly. Moreover, the model would constantly calculate new surface charge densities as the geometry changes over time. This was important, as surface charge density is typically not accounted for mathematical equations, but heavily impacts reaction rates at a microscale. Also, the ability to monitor the change in surface charge density allows for accurate parameter optimization.

2.4 Summary

The review of the relevant literature finds that while extensive work has been done in the research fabrication techniques of optically transparent materials and micro feature polishing techniques, existing published work does not provide several requirements for the intended work. First, none of the papers surveyed microfeatures fabricated on a bulk surface. The microfeature array for the 2D nozzle array is situated on an 11 mm thick surface. The disparity between size of the microfeatures and the bulk surface can add issues during the curing process of casting and forming process during hot embossing. Also, maintaining optical transparency throughout the 11mm depth was not discussed in any of the surveyed papers. Second, the papers that utilized casting or lithography only

used PDMS as their material of choice. Very few used rigid polymers such as polycarbonate or acrylic. The part to be fabricated for this study is to be made of a rigid transparent polymer. Mold ejection for rigid polymers will be more difficult than more compliant polymers such as PDMS. Ejection will be an item of interest, as both thick (11 mm) and thin (0.5 mm) parts will be fabricated, and the ease of ejection will be an important marker for scalability to high volume production. Thirdly, few of the papers utilize micromilling techniques to fabricate the mold used. Using conventional CNC milling operations to create a mold is representative techniques used for tool making for high-volume production and is more relevant to the intent of this study.

CHAPTER 3

MICRO-FEATURE MOLD MANUFACTURING

3.1   Introduction

As mentioned in Chapter 1, the first method utilized was the direct machining of the features into polycarbonate. For single unit production, this was the fastest and cheapest form of fabrication. Micromilling techniques were used to machine pockets to form the features into the polycarbonate. The primary challenge with machining optically clear materials was that it was difficult to tune the spindle speed and feedrates. Direct machining plastic yielded parts with incorrect geometric dimensions as well and nontransparent parts. Based on prior work done in the field, casting optically transparent microfeatures has been proven to be an effective form of fabrication. Because of the success found from machining brass, micro-molds will be fabricated by machined using micro-milling techniques, and then used to cast a polymer resin. The proposed process is a natural stepping stone to high volume injection molding, and acts as a feasibility study. The process of manufacturing a mold requires the micro-machining process, as well as the polishing and surface enhancement. Electropolishing techniques were used to polish delicate features of the mold. A multi-physics model was developed to help predict material removal rates and optimize parameters for the electrochemical etching process.

3.2   Machining Micro-Feature Molds

3.2.1   Candidate Parts: 2D and 3D Microfeature Arrays

The two candidate parts for this study are to be used in a biofluidics device. Each part was comprised of a micro-nozzle array that was used as a vehicle for cell transfection. The first part that was fabricated was the 2D nozzle array. The part drawing and

dimensions are shown below in Figure 3.1. Two 500 μm wide channels lead into a central

chamber where the 2D micro-nozzle array is located. The micro nozzles are triangular in

shape, with a base of 750 μm and height of 500 μm. This formed a 55° angle for the

nozzle. At the tip of the nozzle stemmed a long narrow micro-channel 80 μm wide.
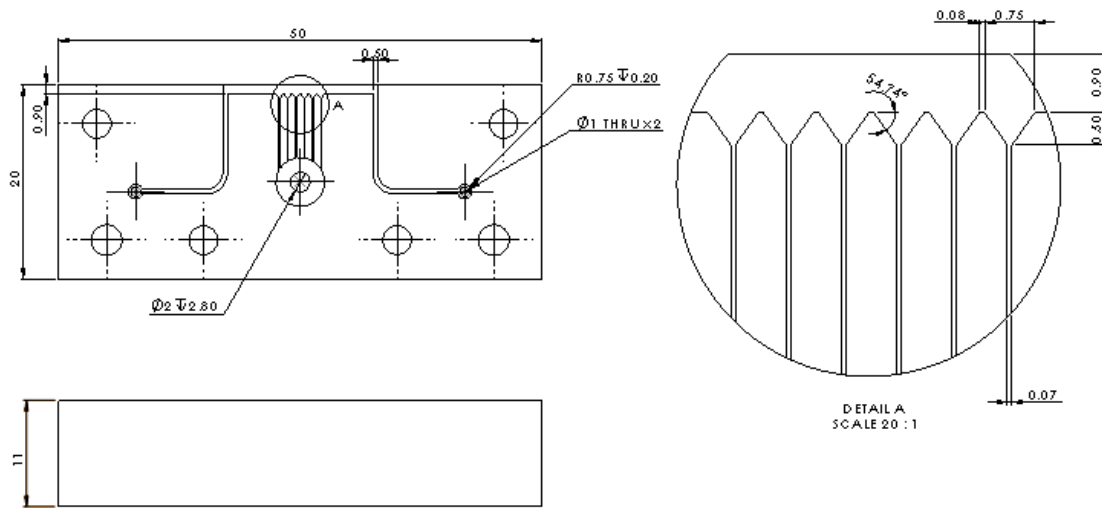
Figure 3.1: The 2D array was comprised of microchannels and 2D triangular nozzles all
of which are 0.2 mm deep. The microfeature array is situated on a bulk material 11 mm
thick.

The second part was a 3D micro-nozzle array. The part was a very small chip that

was to be inserted into a cartridge. The part was only 7 mm x 7 mm x 0.5 mm and has 31

micro nozzles. The nozzles were funnel shaped with the large opening being 750 μm in

diameter, and the orifice only 50 μm in diameter. The part drawing and dimensions are

shown below in Figure 3.2.
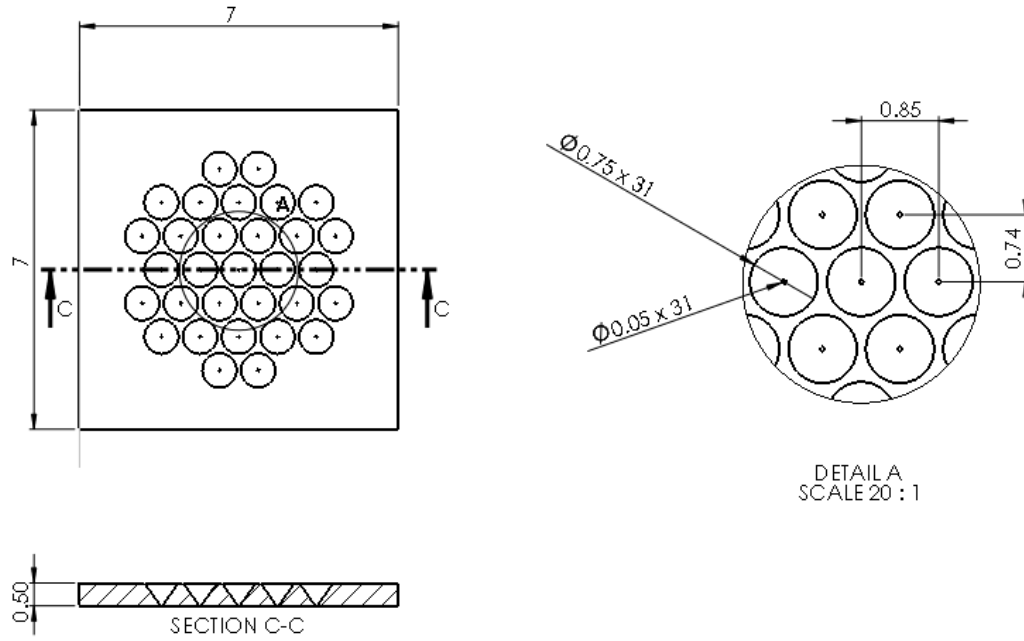
Figure 3.2 The 3D conical array was a thin 0.5 mm thick chip with 31 micro cones arranged in the middle of the piece.

3.2.2   Micro-Machining Challenges

Milling microfeatures efficiently is a challenge, as often times it is impossible to reach optimum process parameters for micromilling. The feedrate required for milling is described in Equation (3.1) where F_r is the feedrate, N is the spindle speed (RPM), f_t is the feed per tooth (mm), and n_t is the number of teeth.

$$F_r = N \cdot f_t \cdot n_t \qquad (3.1)$$

To find the optimum machining parameters for micromilling the microfluidics arrays, Equation (3.1) was used to determine a range of speeds and feeds for cutting brass. The value for f_t was assumed to be 2% of the tool diameter [35]. The assumption takes into account the minimum edge radius of the cutting edge of microtools.

The microtool selected for the analysis was a 100 μm 2 flute endmill as this was the smallest tool to be used for the fabrication. Thus, an equation relating spindle speed (N)

and feedrate (F_r) was developed to determine the machining parameters. In order to determine what spindle speed to use, the surface speed was used to calculate a recommended spindle speed. The equation for spindle speed is shown below in Equation (3.2), where F_s is the surface speed (m/min), and D is the diameter of the endmill (m).

$$N = \frac{F_S}{\pi \cdot D}$$ (3.2)

The recommended surface speed for cutting brass is between 180 and 450 m/min [36]. Thus, to cut brass with a 100 μm tool, the optimal spindle speed required is between 560,000 and 1,400,000 RPM. These spindle speeds are currently not attainable with current technology. While some dental drills have been reported to having speeds of 400,000 RPM, the runout of these drills can be as large as 10 μm [37]. Thus, due to the high-speed requirements and technological limitations of spindle hardware, it is almost impossible to reach optimum cutting parameters required for micro-machining. The corresponding feedrates and spindle speeds for a 100 micron tool is shown below in Figure 3.3.

Spindle speeds and feedrates for 0.100 mm tool
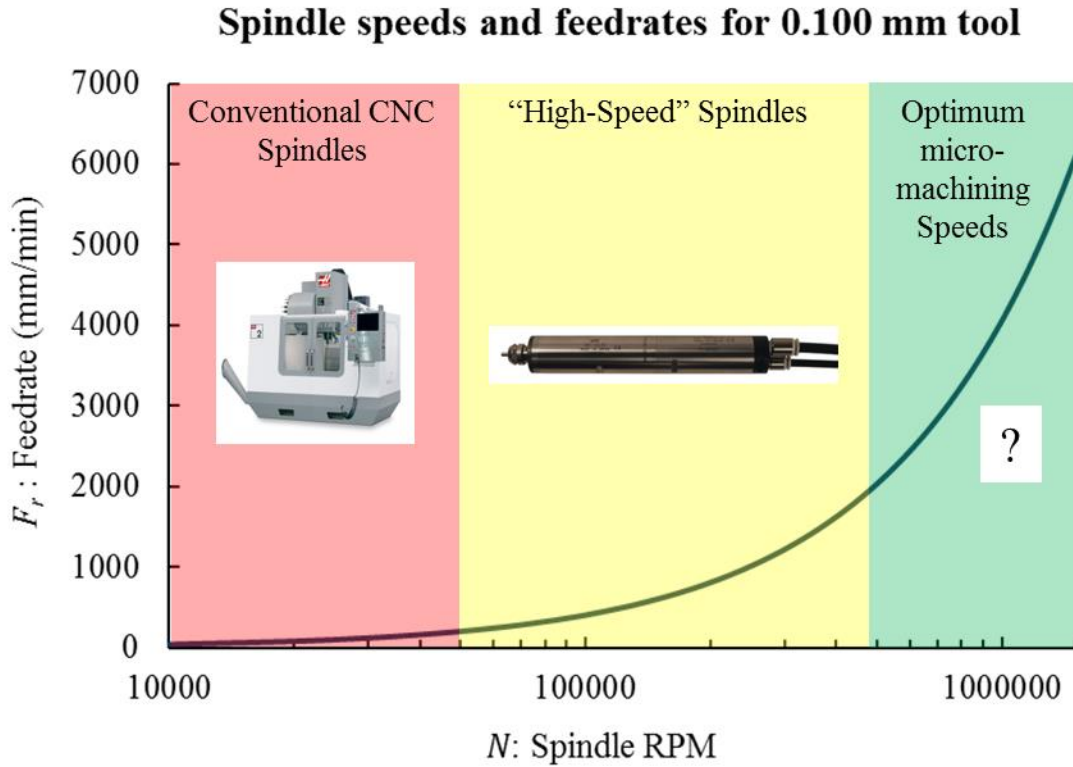
Figure 3.3: Optimum micromachining speeds are highlighted in the green area. Currently it is not possible to reach those machining parameters. Current high speed spindles are located in the yellow region.

3.2.3   Micro-Machining Strategy for 2D array

A machining strategy was developed and utilized to facilitate the spindle speed shortcomings. A 3-axis CNC mill (Prototrak DPM SX2) coupled with a 150,000 RPM air spindle (Nakanishi HTS15001S-M2040) was used to machine the microfeatures. Tool paths were generated using computer-aided manufacturing (CAM) software. Micro-endmills with diameters of 100 μm, 500 μm, and 794 μm were used to machine to features of the biofluidics chip. The CNC mill and high speed spindle are shown below in Figure 3.4.
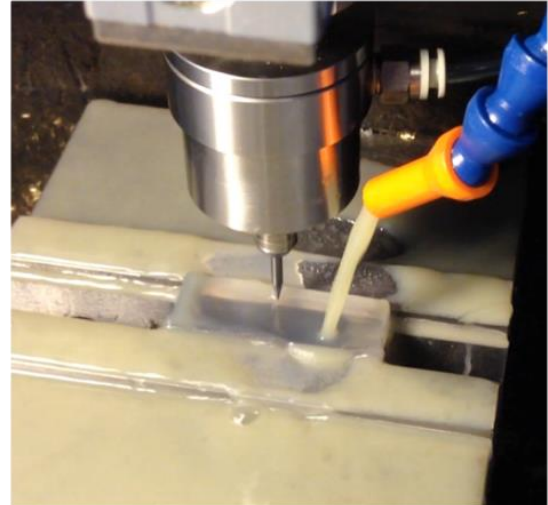
Figure 3.4: The Prototrak 3-Axis CNC mill utilized a 150,000 RPM spindle that allowed for the use of micro endmills.

In order to minimize tool breakage several precautions and steps were taken. First, all micro-tools used an electronic touch off method to register and zero the Z-Axis [38]. This method involved creating a circuit between the tool and workpiece, and measuring current as the tool is lowered. A complete circuit is created the moment the tool is in contact with the workpiece, providing an extremely accurate form of registering the Z-Axis of the CNC machine. Second, the smallest features with the smallest tools were machined first. Having smaller tools machine first avoided tool breakages due to registration errors between tool changes. Third, the tool paths were programmed and generated to allow for overlap between tools and features. Larger tools would clean up machining and burr left by smaller previously used tools. Fourth, the surface of the workpiece was faced using a 4-flute, 1 mm tool spinning at 150,000 RPM and moving at 200 mm/min. The slow feed and high spindle speed created a smooth surface that was vital in preventing the micro-endmills from breaking. Lastly, the feedrates were programmed five times higher than the desired speed. When the program was run on the

29

machine, the feed rates were scaled back to 20% to prevent jerk during the CNC's rapid movements.

In order to create a mold, the inverse geometry of the desired part must be machined. Thus, prismatic protrusions were machined instead of pockets. Machining protrusions provided the advantage of cutting the outsides of the features, which in turn allowed for sharper corners to be machined as corners were not limited by the tool radius as they are when machining pockets. Also, by machining the outside of the features, thinner microchannels could be formed, as tool diameter is not a limiting factor. Feedrates for each tool were calculated using Equations (3.1) and (3.2). The speeds, feeds, and machining order for the 2D array are presented in Figure 3.5.

Order used		Tool Diameter (μm)	Feed Rate (mm/min)	Spindle Speed (RPM)
1		100	500	150,000
2		500	1000	150,000
3		794	1200	150,000
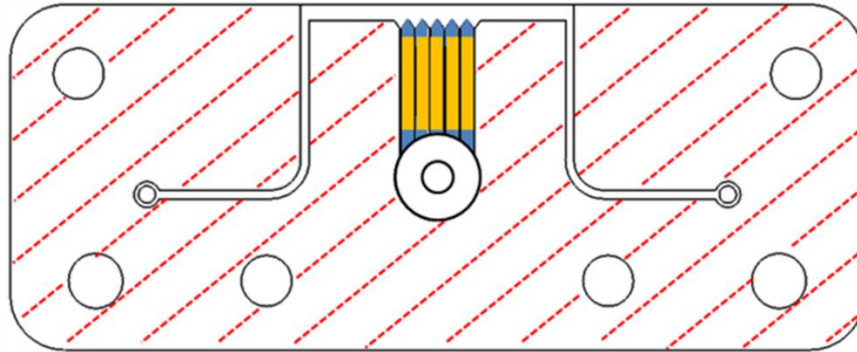
Figure 3.5: The smallest tools were used first to machine the nozzles. Afterwards the microchannels were machined using larger tools.
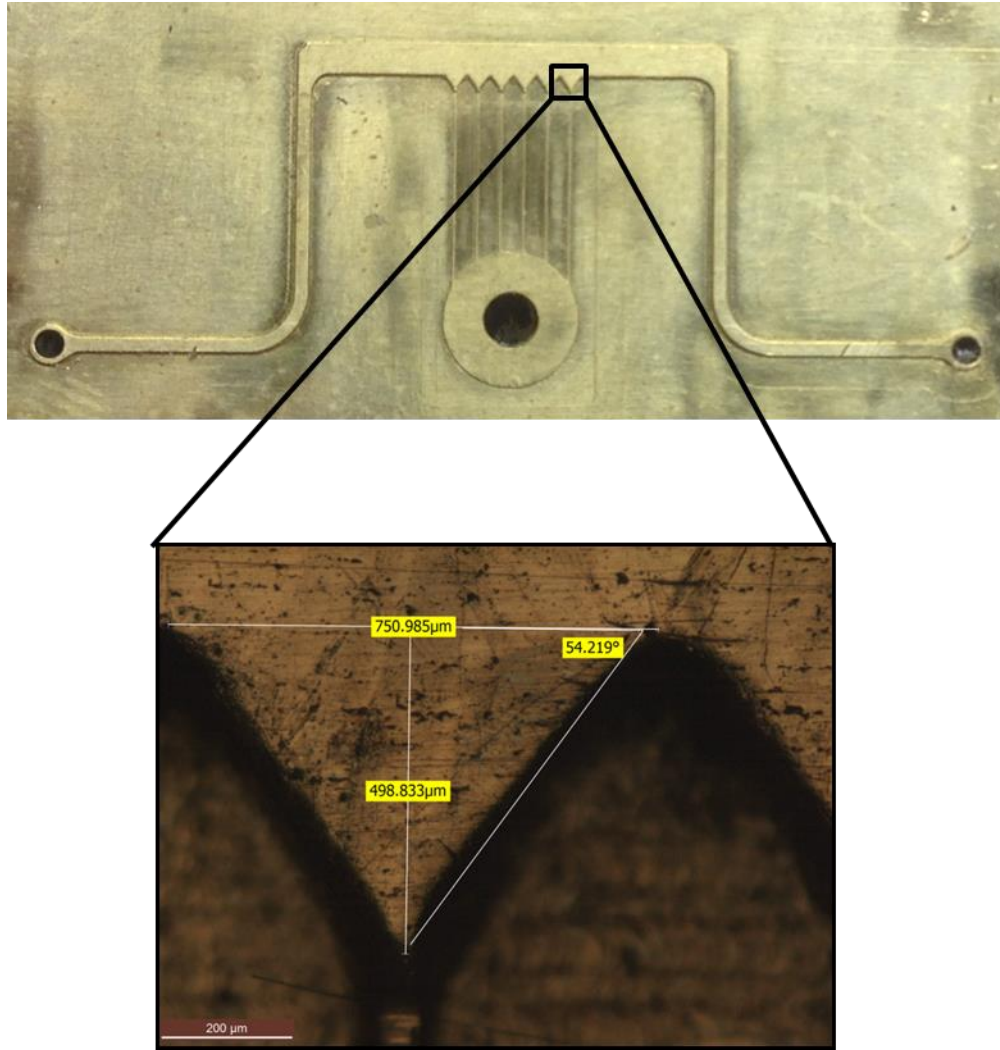
Figure 3.6: The nozzle micro-features in final machined mold were verified under a microscope to have the correct dimensions.

3.2.4 Micro-machining strategy for 3D array

Machining the 3D nozzle array was much more challenging, as the part had a more features, and was tapered in the Z direction. In order to create a mold with the 3D nozzles, the inverse geometry had to be machined. Thus, an array of conical frustums was machined to be protruding from the base of the workpiece. Two strategies were developed and tested to fabricate the cones.

The first method was the "Layered Cake" pattern. The technique consisted of using a micro-endmill to cut concentric circles with increasing diameters at progressive depths. The result was terraced steps that form a cone. The tool path generated to perform the layered cake pattern is shown in Figure 3.7. A 100 μm endmill running at 80,000 RPM and traveling at 275 mm/min was used to cut the feature. A depth of cut of 5 μm was used creating 20 total passes and steps for the cone. Each cone took approximately 10 minutes to cut.
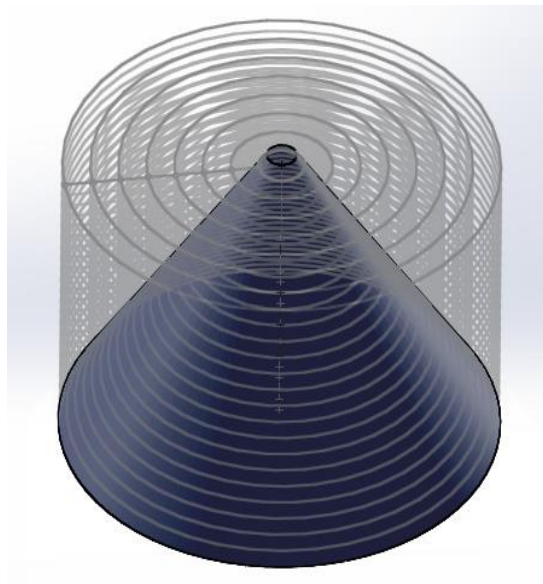
Figure 3.7: The tool path for a 100 μm tool cutting the layered cake pattern consisted of concentric radiating circles.

The layered cake method proved futile, as the resulting structure of the feature did not form a smooth conical surface. Each step was well defined and was not suitable for the cell transfection application. A light interferometer (ZYGO OMP-03680) was used to map and measure the surface profile of the cones. A surface plot of the terraced cone is shown in Figure 3.8. Also the machine time for an array of cones took too long, as an array of 31 cones took almost 6 hours to complete.
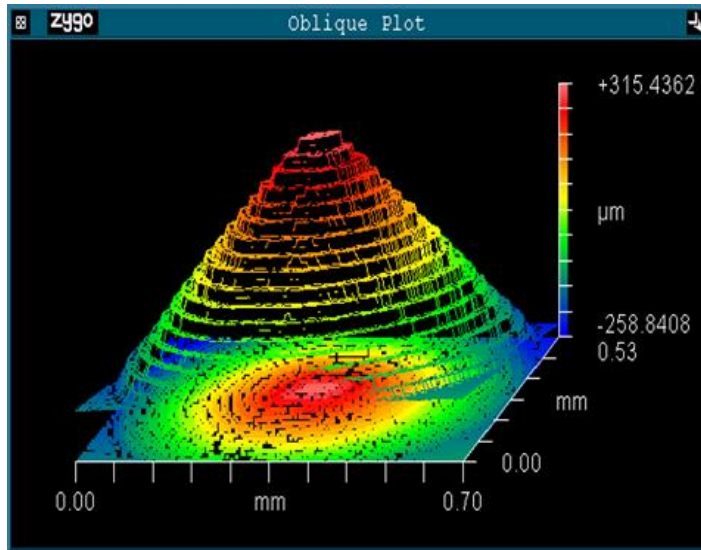
Figure 3.8: Surface profile of the layered cake pattern. The steps from the terracing are prominent and do not make a smooth surface.

To counter the length machining time and rough steps, a second machining method was developed. An angled cutting edge was used to machine the cones. The cutting tool was a single flute cutting edge with a 70° taper. The cone was formed by cutting a circle with a radius of the base of the cone, and stepping downwards in the Z direction. With this method, steps are not created as only one circular profile was cut (base radius). Also, because only one circular profile was cut, the machining time was reduced to 1 minute per cone, and 31 minutes for an array. An illustration of the tool and the surface profile of the cone is shown below in Figure 3.9, and the final machined piece is shown in Figure 3.10.
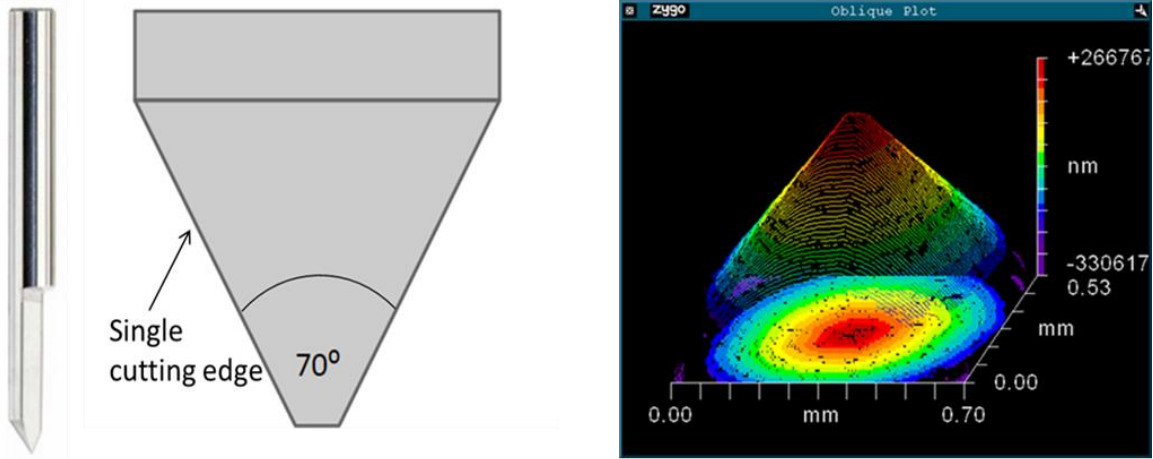
Figure 3.9: The surface profile of the cone using the angled cutting tool was much smoother and consistent than the layered cake method.
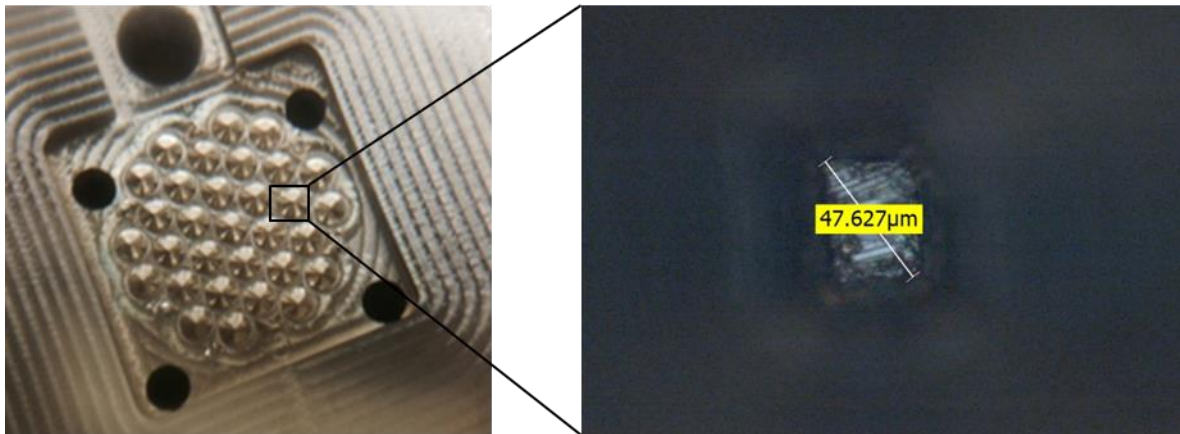
Figure 3.10: The tips of the cones were measured under a microscope to be roughly 50 µm in diameter.

3.3   Micro-mold error analysis

While the micro-cone array could be fabricated, it was important to examine the tolerance stack-up and error propagation due to the equipment and fixture errors. Error analysis is particularly important in micro-mold fabrication, as microfeatures are mating with other pieces, and small subtle errors encountered in macro-manufacturing are magnified when dealing with features on the micro scale.

For the purpose of this study, the 3D micro-cone array was used as a case study. The array was comprised of 31 cones radiating in a concentric fashion. The diameter of the base of the cones was to be 0.750 mm and the top of the cones were to be flat and have a diameter of 0.05 mm ±0.005 mm. The critical dimension for the cone was the tip radius. The geometry could accommodate any cone heights and angles that yielded the desired tip radius. A picture of the machined cone array is displayed Figure 3.11.
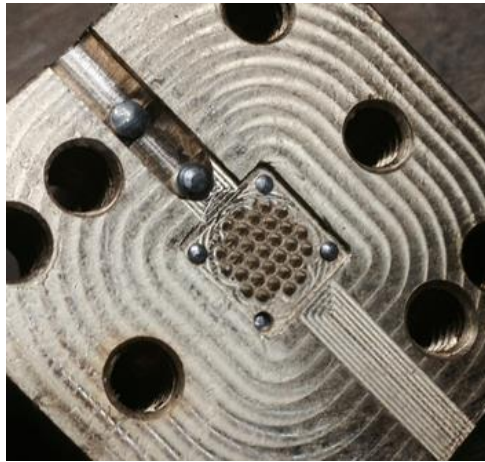
Figure 3.11: A micro-mold was fabricated with the micro-cone situated in the center of the mold cavity.

The cones were to be manufactured using CNC milling techniques. An angled cutting tool with a fixed angle would incrementally cut circular profiles while stepping downwards in the Z direction. The tool would cut a base radius of 0.375 mm and cut to a final depth that corresponds to the cone height. Because of the shape of the tool, a truncated cone with a tip radius of 0.025 mm will be left after machining a height of 0.5 mm. This process was then repeated to complete the entire microfeature array. The uncertainties that were explored were the effects of the XYZ stage resolution, the tool angle tolerance, and the flatness of workpeice.

3.3.1 Analytical Expression of the Microfeatures

To understand and quantify effects of the variations and uncertainties of the *XYZ* resolution and flatness of the workpiece, mathematical equations were developed to represent the dimensions of the cones. First, a single cone was modelled. The cone was modelled in 2D as there is radial symmetry throughout the feature. The cone comprised four variables. The tip radius (r_1), the base radius (r_2), the overall height of the cone (H_1), and the cone angle (Θ). The diagram shown in Figure 3.12 depicts the representation of the cone array.
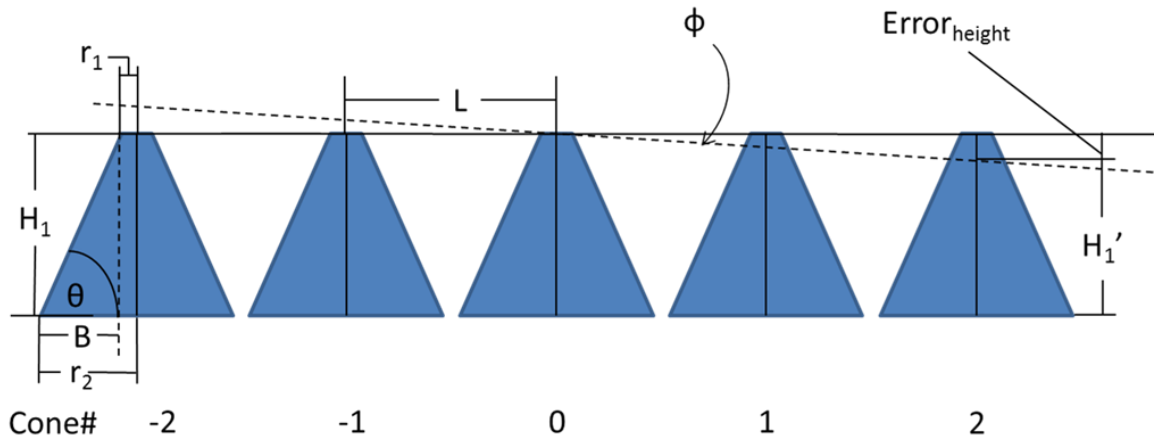
Figure 3.12: A 2D representation of the cone array was created with basic geometry.

The input variables are H_1, r_2, and θ. The output variable is the nozzle tip radius r_1. Equations (3.3) and (3.4) were developed from Figure 3.12 to calculate r_1. Inserting Equation (3.3) into Equation (3.4) yields a direct relationship between the base radius, cone height, and cone angle with the cone tip radius and is shown in Equation (3.5).

$$B = \frac{H_1}{\tan(\theta)} \tag{3.3}$$

$$r_1 = r_2 - B \tag{3.4}$$

$$r_1 = r_2 - \frac{H_1}{\tan(\theta)} \qquad (3.5)$$

While Equation (3.5) is sufficient for a single cone, it does not consider an array of cones nor the flatness error of the workpeice. To determine the cone tip radii of cones in an array, additional variables needed to be added to the equation. As shown in Figure 3.12, the additional variables are the pitch between the cones (L), the cone number, and the flatness angle error (ϕ). The flatness angle was taken as the angular error from the horizontal of the center cone. This created symmetry about the middle cone, and allowed for both positive and negative flatness error to be accounted for. The flatness error of a given cone in the array was calculated by using the cone pitch and cone number in conjunction with the flatness error angle. The method is shown in Equation (3.6).

$$E_f = \tan(\phi) \cdot L \cdot (Cone\#) \qquad (3.6)$$

After the flatness error was calculated, the new cone height ($\acute{H}_1$) was calculated using Equation (3.7). The new cone height was plugged back into Equations (3.3) and (3.4) to calculate the new nozzle tip radius. The final equation for the tip radius is displayed in Equation (3.8).

$$H_1' = H_1 - Error_{flatness} \qquad (3.7)$$

$$r_1' = r_2 - \frac{H' - \tan(\phi) \cdot (L \cdot Cone\#)}{\tan(\theta)} \qquad (3.8)$$

3.3.2 Sensitivity Model and Study

The partial derivatives of Equations (3.8) were used to determine the sensitivity of the cone tip radius to the uncertainties of the *XYZ* resolution, tool/cone angle and flatness

37

error. The partial derivatives of the tip radius are shown in Equations (3.9) through (3.12).

$$\frac{dr_2}{dr_1} = dr_2 \tag{3.9}$$

$$\frac{dH_1}{dr_1} = -\frac{1}{\tan(\theta)} dH_1 \tag{3.10}$$

$$\frac{d\phi}{dr_1} = C \cdot \sec^2(\phi) \cdot \cot(\theta) \cdot d\phi \tag{3.11}$$

$$\frac{d\theta}{dr_1} = -\csc^2(\theta) \cdot (H_1 - C \cdot \tan(\phi)) \cdot d\theta \tag{3.12}$$

The partial terms at the end of the equations (dr_2, dH_1, $d\phi$, and $d\theta$) are the uncertainties of their respective variables. The uncertainty of the cone height (dH_1) and base radius (dr_2) was imposed as the *XYZ* resolution of the CNC stage. The uncertainty of the cone angle ($d\theta$) was imposed as the tolerance of the angled tool as well as possible over or undercutting of the tool. The uncertainty of the flatness ($d\phi$) of the workpiece was taken as half of the angle (ϕ). Summing Equations (3.9) through (3.12) together yields dr_1, also known as the sensitivity or uncertainty of the tip radius. For the purpose of the study, the sensitivity was taken to be the dimensional tolerance of the feature. The formula for dr_1 is shown below in Equation (3.13).

$$dr_1 = dr_2 - \left[\frac{1}{\tan(\theta)} dH_1\right] + \left[C \cdot \sec^2(\phi) \cdot \cot(\theta) \cdot d\phi\right] - \left[\csc^2(\theta) \cdot (H_1 - C \cdot \tan(\phi)) \cdot d\theta\right] \tag{3.13}$$

The sensitivity of the tip radius is affected by the magnitudes of H_1, θ, and ϕ. The magnitude of base radius (r_2) did not affect the sensitivity of the tip radius because r_2 it a linear term in Equation (3.8).

To map dr_1, values of r_1 were first calculated and plotted over a range of increasing cone heights and cone angles using Equation (3.8). The cone heights were varied from 100 μm to 500 μm, and the cone angle ranged from 30° to 80°. The base radius was held constant to 375 μm as it did not impact the sensitivity. The plot of r_1 values are displayed in Figure 3.13.
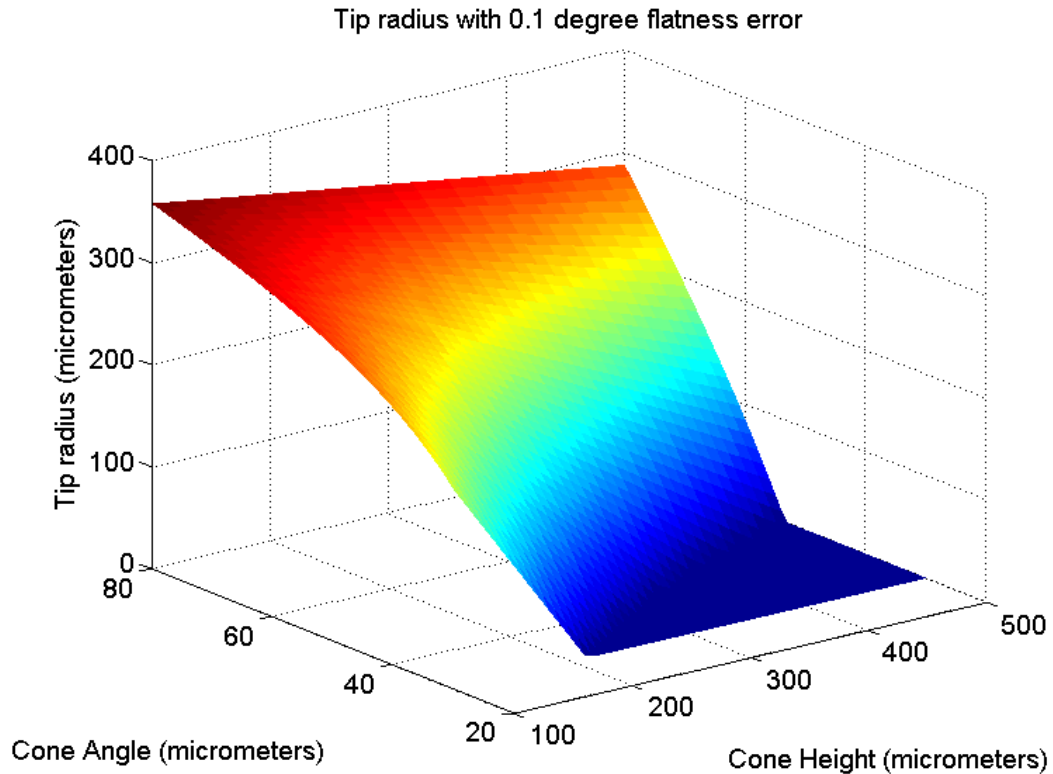
Figure 3.13: The tip radius of the cone with base radius 0.375 mm was calculated and plotted over a range of varying cone heights and cone angles.

The sensitivity at each of the points in Figure 3.13 was then calculated using Equation (3.13) and plotted. The sensitivity values of r_1 are shown in Figure 3.14. The uncertainty values for dr_2, dH_1 and $d\theta$ was 10 μm, 10 μm, and 0.1° respectively. A flatness angle error (ϕ) of 0.1° was selected with a $d\phi$ value of 0.05°.
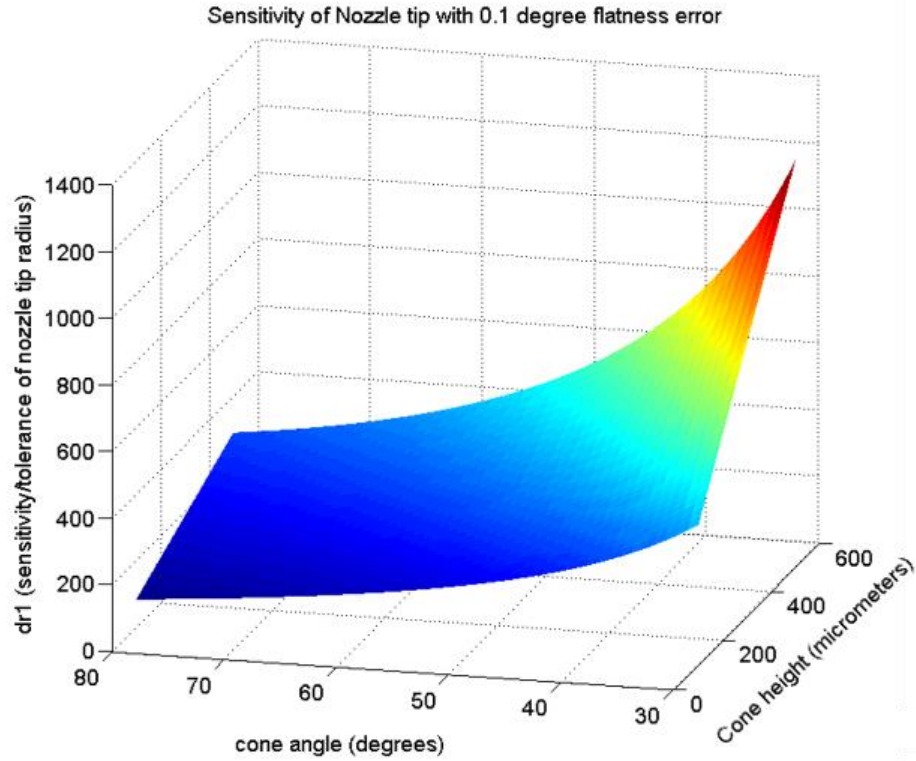
Figure 3.14: The plot shows that sensitivity of the tip radius increases as the tip radius decreases.

3.3.3 Analysis of sensitivity model

The plots in Figure 3.13 and Figure 3.14 were of a specific case. The plots had a constant base radius (r_2) of 0.375 mm. While increasing and decreasing base radius will change the tip radius values in Figure 3.13, it does not affect the sensitivity of the tip radius (dr_1). This was expected as Equation (3.13) is not affected by the base radius. The factors that affected the sensitivity of the tip radius were H_1, θ, ϕ, and the uncertainty values dr_2, dH_1, $d\phi$, and $d\theta$. Figure 3.14 shows that as cone height increases and cone angle decrease, the sensitivity of the tip radius increases. This trend was expected, as larger cone heights and smaller cone angles lead to smaller tip radii. Thus, the feature becomes smaller and is more sensitive to dimensional change due to metrological

uncertainties. When accounting for flatness error, the same trend occurs. The magnitude of the sensitivity of the tip radius is larger when flatness error increased.

The uncertainty values were altered to determine the effect of each variable as well as determine what tolerance and resolution is necessary to maintain the dimensional accuracy for the tip radius. Out of the eight variables ϕ, $d\phi$, and $d\theta$ significantly altered the sensitivity plot. Lowering $d\theta$ produced the largest drop in sensitivity, and lowering $d\phi$ produced the second lowest drop in sensitivity. The XYZ stage resolution (dr_2 and dH_1) were not significant factors towards the sensitivity of the tip radius. These trends were noted by monitoring the drop in sensitivity by one by one lowering each factor to zero. This data is displayed in Table 3.1.

Table 3.1: The sensitivity of the tip radius with flatness error

$d\phi$	dr_2	dh_1	$d\theta$	Max Sensitivity
0.05	10	10	0.5	1204.4
0.05	0	10	0.5	1214.4
0.05	10	0	0.5	1239.7
0.05	10	10	0	230.8
0	10	10	0.5	1000.1

The model and analysis were then used determine the tolerances and resolutions necessary to maintain a ±5 μm dimensional tolerance (dr_1) for a 25 μm tip radius. The parameters were determined by solving for dr_1 of a 25 μm tip radius while decreasing the values of ϕ, dr_2, dH_1 and $d\theta$ until dr_1 was less than 5 μm. It was determined that a maximum flatness error (ϕ) of 0.005°, flatness uncertainty ($d\phi$) of 0.0025°, tool angle tolerance ($d\theta$) of 0.01°, and an XYZ stage resolution (dr_2 and dH_1) of 1 μm were necessary in order to maintain dimensional tolerance (dr_1) less than 5 μm. This was represented by the black dotted line in the graph depicting displayed in Figure 3.15. In

the graph, any values of dr_1 that were below the maximum tolerance limit line consisted of uncertainty parameters that would yield parts within the dimension tolerance limit. These parameters would be the tolerances and resolutions needed to maintain the ±5 μm tolerance for a 25 μm tip radius. For reference, a ϕ value of 0.005° is equivalent to a flatness error of 0.001" over a 12" length.

Effect of flatness, tool tolerance, and CNC stage resolution on error propagation of tip radius
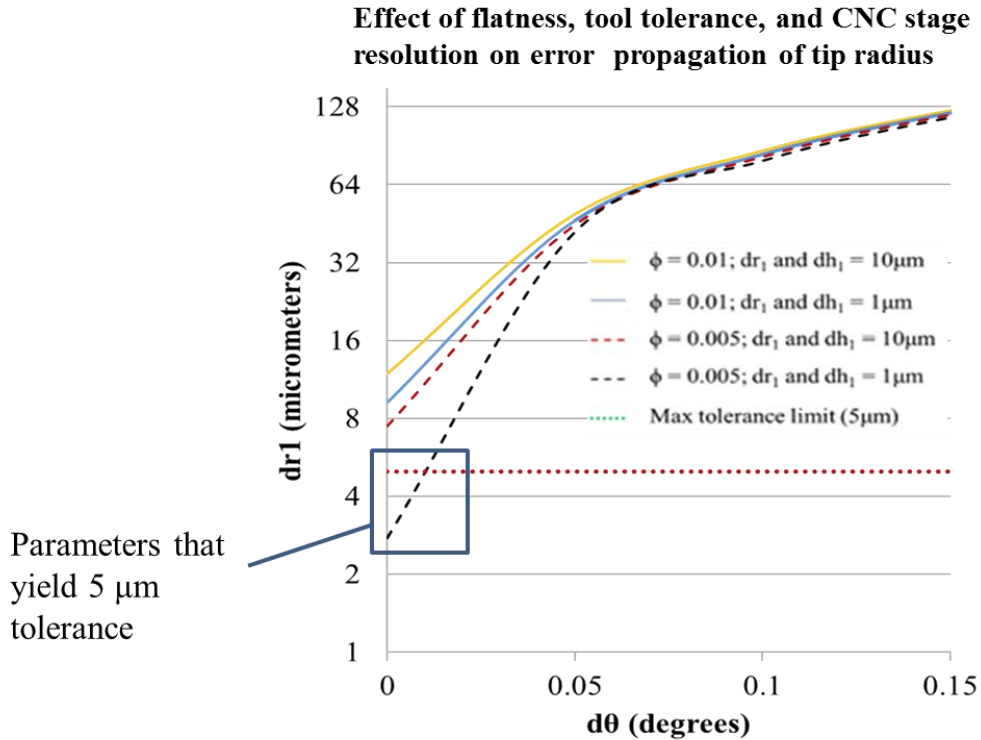
Figure 3.15: The error and tolerance analysis for a 25 μm with a ±5 μm tolerance.

3.3.4 Discussion of Sensitivity and error analysis

The sensitivity analysis of the micro-cone array shows that the error propagation used to tolerance dimensions does not scale linearly from macrofeatures to microfeatures. This trend is illustrated in Figure 3.13 and Figure 3.14. Figure 3.14 displays tip radii ranging from 375 μm down to 1 μm, demonstrating how the propagated error of the tip radius increases at a non-linear rate as the feature size decreases and approaches zero. The increase in sensitivity is primarily due the variation in tool angle, $d\theta/dr_1$. Larger values

of cone height (H_1) and smaller values of θ lead to much greater magnitudes of $d\theta/dr_1$, which contributed greatly to increasing the sensitivity of the tip radius (dr_1). This trend corresponds to the fact that smaller tip radii are associated with taller cone heights and smaller cone angles.

To further illustrate the trend of nonlinear error propagation with microfeatures, the sensitivity of a 25 μm and 350 μm feature was compared. Values of ϕ were increased and dr_1 values were recorded. The $d\phi$ values used were equivalent to half of the value of ϕ. The data from the analysis are displayed in Table 3.2.

Table 3.2: Effects of scaling feature size and flatness and error propagation

	dr_1 (μm)	
ϕ (degrees)	25 μm tip radius	350 μm tip radius
0.001	9.49	11.38
0.01	19.38	11.53
0.1	99.7	31.7

As flatness error (ϕ) increased, the sensitivity of the 25 μm feature increased at a much faster nonlinear rate as compared to the 350 μm feature. The 350μm feature saw almost no change when the flatness error changed from 0.001° to 0.01°, whereas the 25μm feature saw more than a 100% increase in sensitivity. This trend corresponds with the nonlinear scaling trends seen in Figure 3.13 and Figure 3.14.

The sensitivity analysis presented in this paper shows that while *XYZ* stage resolutions are important while fabricating microfeatures, the tolerances and errors from the tool and workpeice have significantly larger impacts on the error propagation at the micro scale. This is expected as the relative magnitude of the error compared to the feature size is much higher at the microscale versus the macroscale; thus resulting in highly sensitive feature error and tolerances.

3.4   Summary

Microfeatures were fabricated into brass workpieces using micromilling techniques. The 2D array was machined using a 3-axis mill fitted with a 150,000 RPM spindle and micro-endmills. Conductive touch-off was used to register the tools and workpiece, and the rapid movements of the machine were reduced to minimize tool breakage. The 3D array was machined using an angled cutting tool to cut the cones.

A sensitivity analysis was performed to evaluate the challenges involved with machining the 3D cones and maintaining dimensional consistency throughout the array. It was noted that as feature size decreased, the propagation of error from the tool angle, CNC stage and flatness. Tool angle was the most significant source of error followed by flatness angle.

The next step in the process was to polish the microfeatures. Reducing the surface roughness of the microfeatures was important as they are going to be used to cast the final parts, thus achieving the best surface roughness of the mold will result in a better final part.

CHAPTER 4

ELECTROPOLISHING MICRO-FEATURE MOLDS

4.1   Background to electropolishing

Once the micro-molds were fabricated, they had to be clean and polished to achieve the smoothest surface possible. This was to ensure the cast parts would retain the optimum optically transparency and surface finish as possible. Reducing surface roughness is typically is not an issue when casting macroscopic features and parts, but when dealing with an array of microfeatures, improving surface finish becomes a challenge. The most common technique used to polish metal surfaces is through mechanical abrasion. Mechanical polishing is not possible with micro-features as there is not enough space to polish in between the micro-protrusions. Also applying direct force to the microfeature array could deform the features [24].

To counter the challenges of mechanical polishing techniques, a passive form of polishing was utilized. Electrochemical polishing (Electropolishing) involves submerging the working piece (anode) and an additional piece of metal (cathode) in an ionic solution while running DC current through the system. An oxidation-reduction occurs that removes metal ions from the surface of the anode. Over time, surface roughness of the anode is smoothened by the reduction of metal ions from the microscopic peaks on the surface. While the process can polish in between narrow microchannels, it is hard to predict the rate of the reaction as well as the possible erosion of the microfeatures on the bulk surface. Thin walled microfeatures have high surface area to volume ratios. Thus, the microfeatures have higher current densities and are more prone to the reaction, causing more ions to leave and deforming and flattening the feature.

The reactions involve passing DC current through metal pieces submerged in an electrolytic solution. The current initiates an oxidation reduction reaction, which pulls electrons from the valence shells of the metal ions of the cathode [27]. The process causes positively charged metal ions to leave the anode. This reaction is illustrated in Figure 4.1.

$$Me + 2H^+ + O^{2-} \rightarrow MeO + H_2$$
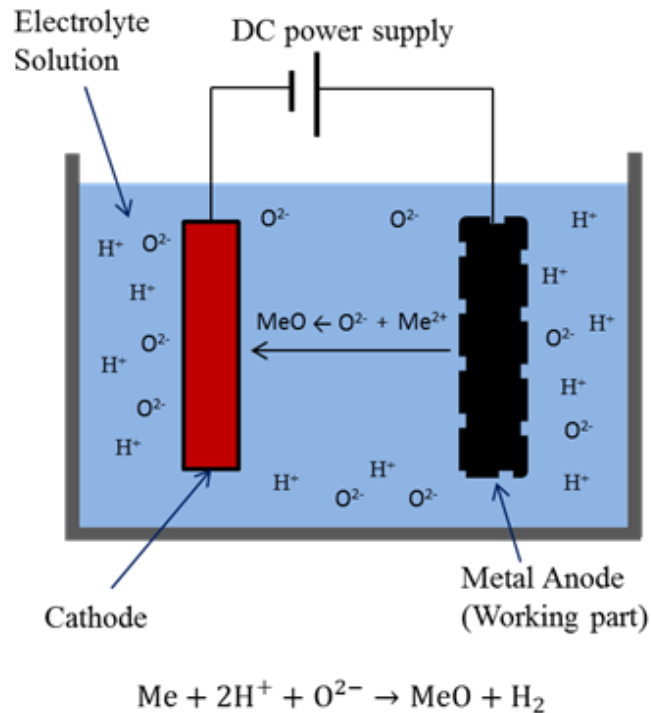
Figure 4.1: The electric current induces an oxidation reduction reaction, which takes metal ions from the surface of the anode and combines them with oxides left from the electrolyte solution. These metal salts are deposited onto the cathode.

Layers of metal are removed from the surface of the part, resulting in smoother surfaces and a reduction in surface roughness. This is useful when attempting to smooth multiple parts with nonconventional features and large surface areas. The material removal from electropolishing can be characterized by Equation (4.1) where the volume removed (V) is equal to the product of the surface area (A), voltage drop (E), time(t) and number of valence electrons(N) divided by the product of Faraday's constant (C), atomic

mass (n), density of anode (ρ), gap distance between electrodes (d), and resistivity of the solution (r) [39].

$$V = \frac{A_s \cdot E \cdot t \cdot N}{C \cdot n \cdot \rho \cdot d \cdot r} \qquad (4.1)$$

4.2 Modeling electropolishing for parameter optimization

4.2.1 Modeling Objectives

The primary goal of this study was to model the electropolishing reaction for the microfeature arrays and optimize the experimental parameters required to smoothen their surfaces. By developing a finite element model, a design of experiments was utilized to test and gather data to create a statistical model that optimized parameters based on a desired amount of material removal.

4.2.2 Finite Element Model for Electropolishing

While Faraday's law of electrolysis in Equation (4.1) calculates the amount of material removed during the electrochemical process, it does not indicate from where exactly on the anode was the material removed from [27]. This is because the equation assumes there is a uniform surface charge distribution along the surface of the anode. Thus, the reaction is assumed to be occurring equally along the surface of the workpiece, and results in material being removed evenly and equally across the work piece. Unfortunately, this assumption is not valid when dealing with sharp protrusions. Specifically, micro-feature arrays pose a challenge as they are often comprised of arrays of high-aspect ratio protrusions. The material removal rate is driven by the surface charge density of the part, thus areas with high surface charge densities will have material removed faster than those with low surface charge densities. This underlying principle is

the mechanism that allows for the process to smoothen a surface over time, as protrusion and ridges had higher surface charge concentrations and are removed. An illustration of surface charge distribution of microfeature protrusions is shown below in Figure 4.2. The higher charges densities at the top of the features causes the tips and corners of the features to etch faster than the rest of the part.
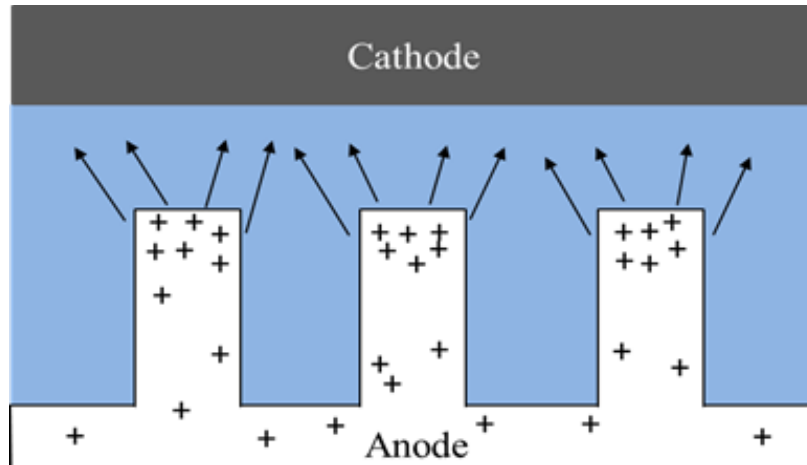
Figure 4.2: Higher surface charge densities are located at the corners and tips of features. These areas experience faster reaction rates and are eroded faster.

In order to account for the non-uniform surface charge distribution, a finite element model was created. The model would take a geometry and calculate the surface charge density along the part. The model was created using COMSOL multiphysics (Version 4.4). The electromagnetics package in COMSOL enabled the calculation of the charge concentrations along the surface of the part. The inputs for the model were the feature geometry, gap distance between the electrodes, voltage drop between the electrodes, the electrical conductivity between of the electrolyte solution, and time. The model outputs the change in surface current density over time, as well as the deformation of the features in X and Y. Deformation is output and mapped as the amount of material removed over

the part. Material removal rates of specific areas of the part could also be calculated by monitoring the amount of material that was removed over a set period of time.

The model simulates the reaction in two dimensions, thus a cross-section of the feature geometry was utilized. The anode (workpiece), cathode, and the electrolyte solution were modeled. An illustration of the model set up is depicted below in Figure 4.3. A 3D model was developed, but proved to be inefficient as computational times often took over 12 hours. This was due to the disparity in feature size between the microfeatures and the bulk surface, and the complicated mesh generation required.
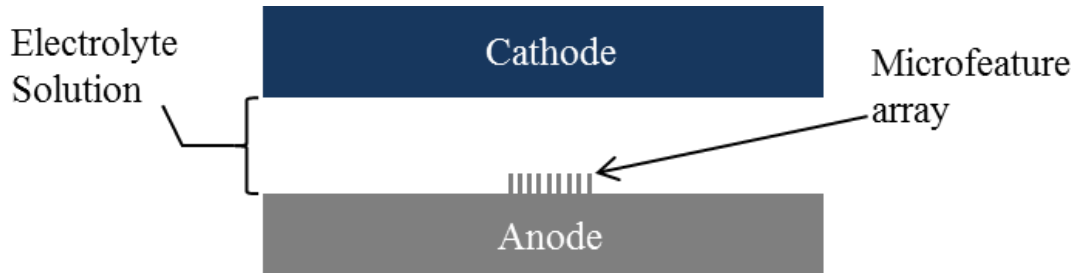
Figure 4.3: The model simulates a 2D cross-section of the microfeature mold and a flat cathode tool above it with an electrolyte solution acting as a medium.

A first order approximation was used to determine the material removal rate. Equation (4.2) states that the material removal rate (U) from the anode is proportional to the amount of current (I) and its direction relative to the surface of the anode (n) [40]. Thus in areas of high current concentration, the material removal rate will be relatively larger. The proportionality constant (K) was used to account for the material properties of the metal electrode. The proportionality constant was calculated using Equation (4.3) where u was the atomic mass of the material, C was Faraday's Constant, ρ was the density of the material, and N was the number of valence electron of the material.

$$U = -K \cdot I \cdot \bar{n} \tag{4.2}$$

$$K = \frac{u}{C \cdot \rho \cdot N} \tag{4.3}$$

The properties used to calculate the proportionality constant of 360 brass are shown in in Table 4.1 [41]. A final value of 1.17×10^{-11} m^3/(A·s) was calculated for K.

Table 4.1 Material and elemental properties of 360 brass

Property	Value
u: Atomic Weight (g/mol)	192.42
ρ: Density (g/cm^3)	8.5
N: number of valence electrons	2
C: Faraday's Constant (C/mol)	96500

A voltage drop was placed between the surface of the cathode and the surface of the anode to simulate the electrochemical reaction. This voltage drop was held constant throughout the duration of the simulation.

4.2.3 Geometries and microfeatures modeled

Two geometries will be modeled and tested in this study. The two geometries will be based on the two parts described in Chapters 1 and 2. The first geometry represents the small microchannels found in the 2D feature array. The microchannels were selected as they are the smallest and most fragile parts of the mold. The microchannels in the mold were formed by machining prismatic protrusions. The setup for the multiphysics model for the prismatic protrusion geometry is displayed below in Figure 4.4.
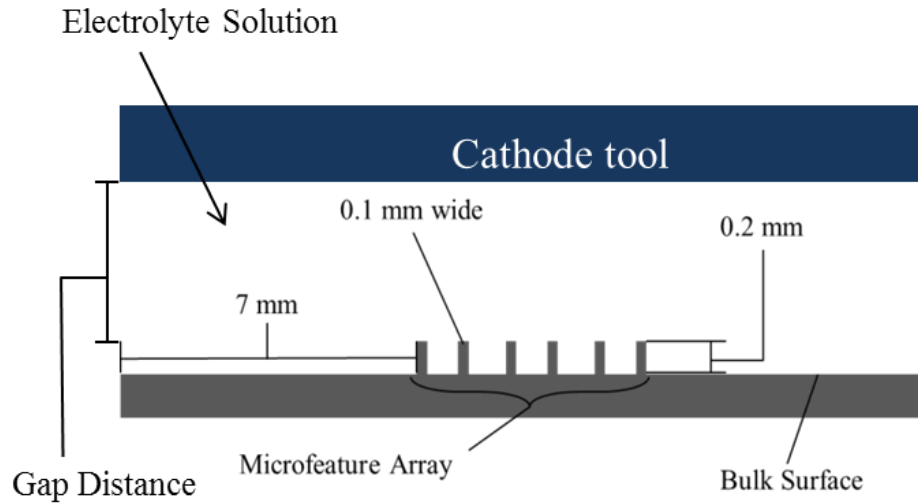
Figure 4.4: Representation of 2D microchannel geometry for electropolishing model

The second set of geometry was derived from the 3D conical feature array. The tips of the cones were the primary area of concern, as they were the smallest feature and were used to form the orifices in the cast parts. The setup for the model for the 3D conical feature array is displayed below in Figure 4.5.
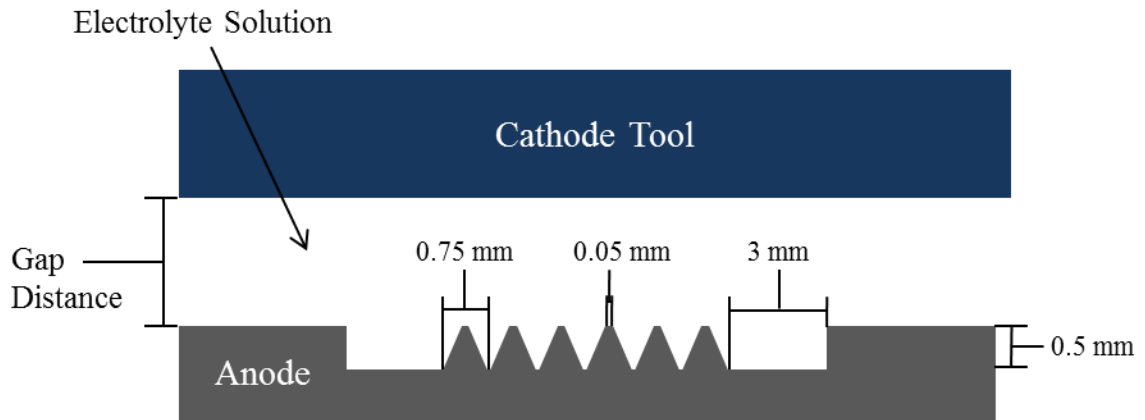
Figure 4.5: Representation of 3D conical array for the electropolishing model

4.2.4 Numerical Modeling: Mesh Analysis

A challenge encountered when modeling electropolishing is accounting for the effects from the change in geometry. As the anode is etched away, the surface charge density

changes. Thus, the gap distance and current density over the surface constantly changes as the anode geometry is constantly deforming and eroding. The problem is illustrated in Figure 4.6.
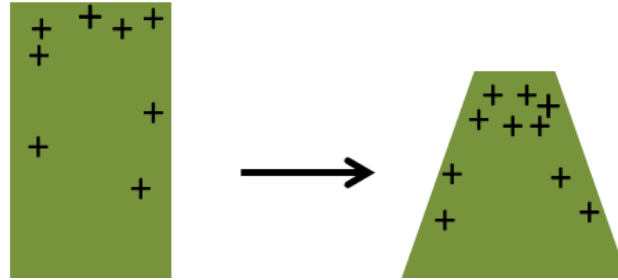
Figure 4.6: As the reaction takes place, the gesture geometry changes, which in turn alters the surface charge density.

To account for this factor, a time dependent moving mesh was utilized to account for the change in geometry overtime. The moving mesh constantly changes overtime to accommodate and comply with a change in geometry. The dynamic mesh allows for new surface charge densities to be calculated iteratively over time as the surface geometry changes.

A mesh analysis was performed to refine and optimize the mesh size by decreasing the maximum element size until results stabilized to a constant value. The parameters used to test were a gap distance of 20 mm, 5 V drop, and a conductivity of 5.94 S/m. The parameters were chosen because they were the upper bounds selected for the study. The largest gap distance yields the largest possible area for the mesh generation. The highest voltage and conductivity correspond to a higher amount of material removal as defined by Equation (3.1). The upper limit parameters provided the most complicated mesh generation for the study, making it an ideal vehicle for the mesh convergence test.

To aid the mesh generation and computation time, a mesh refinement (2nd order) was performed around the features. The refinement created a smaller and finer mesh

specifically around the microfeatures while still keeping larger mesh elements next to the cathode. This reduced the number of calculations while still increasing the mesh density.

Trials were run to test the effect of mesh size on the calculated values for change in height and width of the features (Delta Y and Delta X) after 5 seconds and 30 seconds of polishing. A maximum element size of 1.10 mm was selected as a starting point. The maximum element size was then decreased to 0.75 mm, 0.40 mm, 0.20 mm and 0.10 mm.

The results of this test are shown in Figure 4.7. After the maximum element size was decreased to 0.40 mm, the values for Delta Y and Delta X at 5 and 30 seconds began to stabilize. Running finer mesh sizes of 0.20 mm and 0.1 mm produced results that were within 3% of each other. The 0.20 mm mesh ran an order of magnitude faster than the 0.1 mm mesh, one minute versus 10 minutes. Thus a triangular mesh with refinement around the features with a maximum element size of 0.20 mm and minimum element size of 0.0015 mm was selected for the study.

Convergence plot for electropolishing FEM
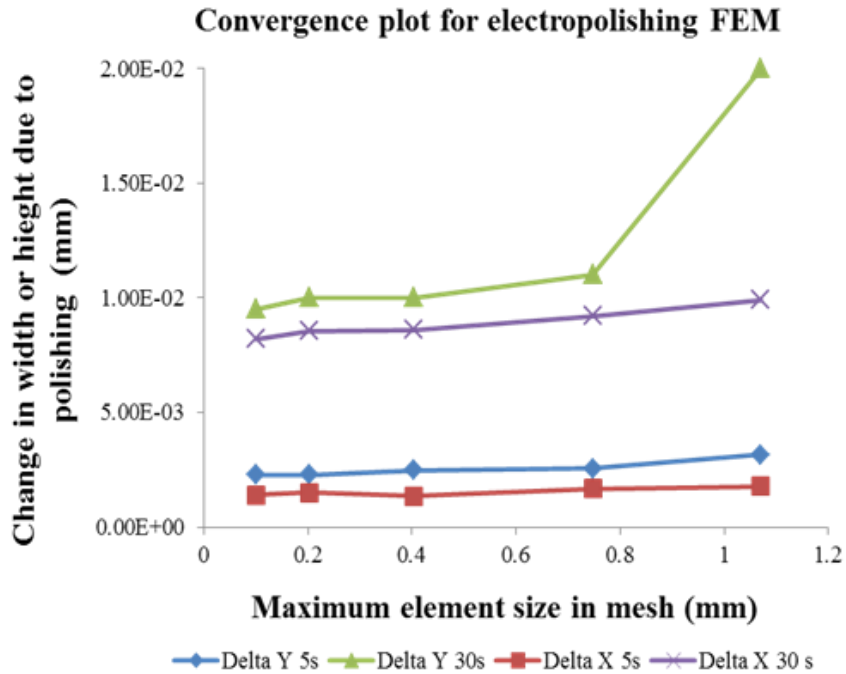
Figure 4.7: The mesh analysis was performed starting from a mesh with a maximum element size of 1.1mm and sequentially decreased it to 0.1mm. The resulting values of the deformation of the features began to converge after the third iteration at 0.40 mm element size.

The resultant mesh for both the microchannel and conical geometries are shown in Figure 4.8 and Figure 4.9.
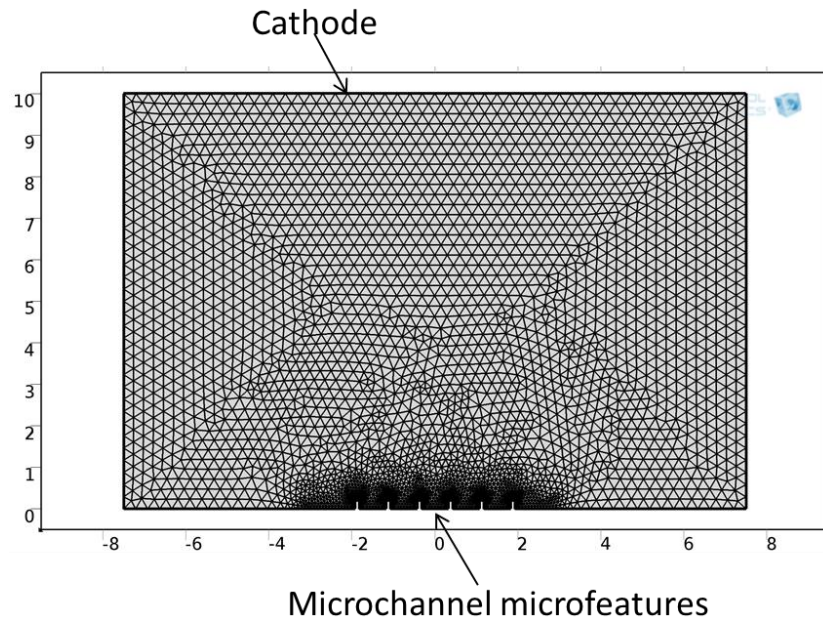
Figure 4.8: Mesh generated for the microchannel geometry. A refinement was placed around the feature array to reduce the total number of calculations while still maintaining a dense mesh around the microfeatures.
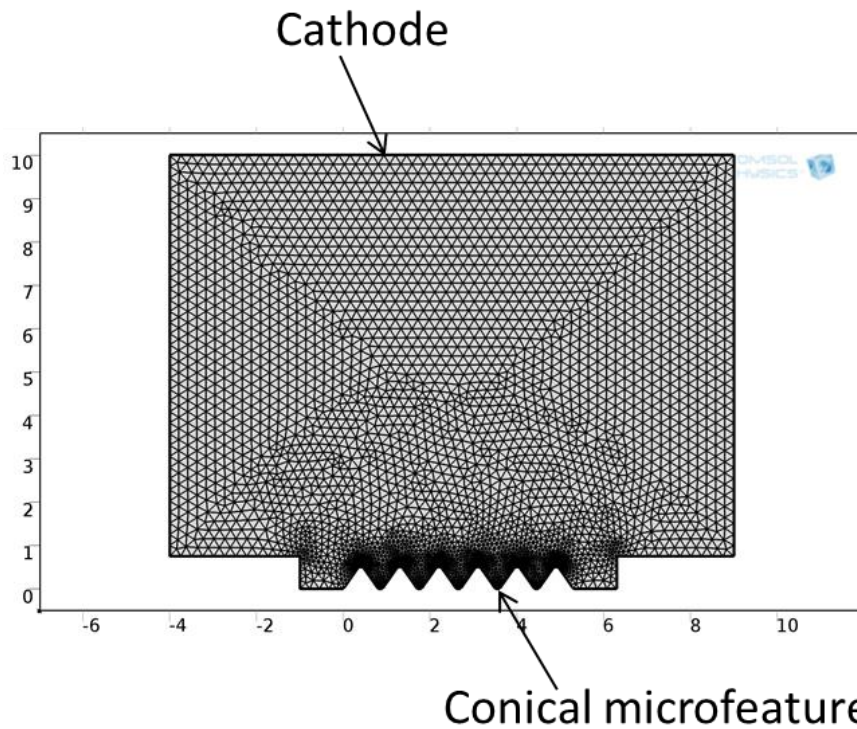
Figure 4.9: Mesh generated for the microchannel geometry. A refinement was placed around the feature array to reduce the total number of calculations while still maintaining a dense mesh around the microfeatures.

The simulation output two plots: Displacement in X, and displacement in Y (Delta X and Delta Y). The displacement in X and Y plots depict the amount of material removed (mm) by calculating the change in distance of the surface from its initial state to its final eroded state. The plots are color maps that indicate where on the part the fastest material removal rates occurred. A black outline represents the original pre-polished geometry, and the white silhouette is the final etched geometry. An example of the output plot is shown in Figure 4.10.
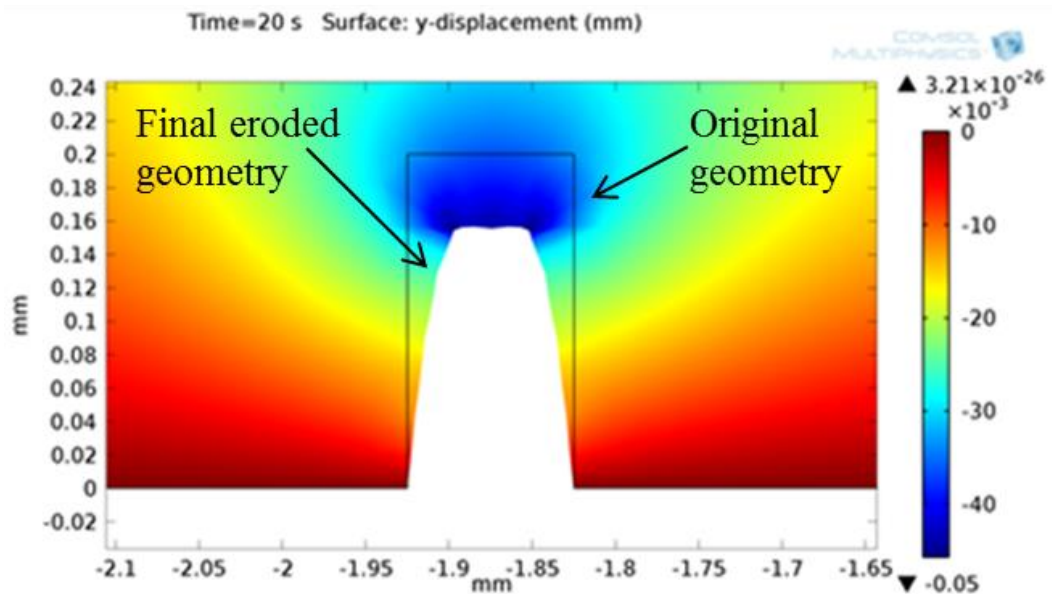
Figure 4.10: The model outputs a color map that corresponds to material removal and shows the initial and final geometry of the microfeature.

4.2.5 Model Verification

The COMSOL model was compared against Faraday's law to validate its computation. A flat plate (15 mm long) was modeled in COMSOL to predict the amount of material removal based on gap distance, conductivity, voltage and time. The amount of material removal calculated from the model was compared to the value obtained from Faraday's equation. The results are displayed in Table 4.2.

Table 4.2: Comparison of COMSOL model and Faraday's law of polishing a flat plate

Gap Distance (mm)	Cond. (S/m)	Voltage (V)	Time (s)	Faraday's-Material removal (mm)	COMSOL-Material removal (mm)	% Difference
1	1.6	1	5	1.00E-03	9.90E-04	-1.00
1	1.6	5	30	3.00E-02	3.00E-02	0.00
1	5.94	1	30	2.23E-02	2.24E-02	0.34
1	5.94	5	5	1.85E-02	1.86E-02	0.54
20	1.6	1	30	3.56E-04	3.57E-04	0.16
20	1.6	5	5	2.97E-04	2.97E-04	-0.01
20	5.94	1	5	2.21E-04	2.21E-04	-0.02
20	5.94	5	30	6.62E-02	6.62E-02	-0.02

The COMSOL model produced the same material removal rates that Faraday's law predicted for the flat plate. In order to illustrate that Faraday's law does not account for surface charge density disparities in microfeatures, the equation was compared to model with microfeatures protruding from the plate. An array of 6 microfeatures with a height of 0.2 mm and width of 0.1 mm were modeled on the same 15 mm long plate. The results from the COMSOL model and Faraday's equation are shown in Table 4.3.

Table 4.3: Comparison of COMSOL model to Faraday's law of polishing of microfeature protrusions on a flat plate

Gap Distance (mm)	Cond. (S/m)	Voltage (V)	Time (s)	Faraday's-Material removal	COMSOL-Material removal	% Difference
1	1.6	1	5	1.16E-03	1.95E-03	68.21
1	1.6	5	30	3.48E-02	6.60E-02	89.66
1	5.94	1	30	2.58E-02	6.00E-02	132.21
1	5.94	5	5	2.15E-02	4.80E-02	122.92
20	1.6	1	30	4.13E-04	1.13E-03	174.27
20	1.6	5	5	3.45E-04	8.38E-04	143.10
20	5.94	1	5	2.56E-04	7.07E-04	176.28
20	5.94	5	30	7.67E-03	1.63E-02	112.48

The COMSOL model resulted in higher levels of material removal compared to Faraday's law. COMSOL accounted for the change in surface charge density along the workpiece resulting in more material removal calculated than Faraday's law. Faraday's law assumes a uniform distribution of surface charge density along the part.

4.3   Electropolishing Process Model

Comparing the COMSOL model to Faraday's law shoed that accounting for surface charge density is required when predicting material removal rates for electropolishing. Thus a design of experiments (DOE) was used to learn and study the effect of surface charge density on material removal. The DOE was then used to develop a regression model to optimize process parameters.

Normally to understand and test five parameters, a three level, full factorial matrix is utilized. The test requires 243 trials, which while very through and detailed, can be very costly in terms of time and money. Instead, a three level central composite design (CCD) half factorial matrix was used to reduce the number of trials to 27 [42]. The CCD half factorial matrix is able to reduce the number of trials by focusing on first and second level interactions and omitting third fourth and fifth level interactions [42]. Omitting higher level interactions will introduce error into the model, but was justified by the time saved from omitting 216 trials. The trials were setup to test the upper and lower bounds of each parameter as well as the midpoints. The upper and lower bounds of each variable are listed in Table 4.4. The bounds of the conductivity of the solution were based on using 5% − 20% aqueous solutions of phosphoric acid [43]. Feature height was bounded based on the geometry of the test piece. Voltage drop, gap distance, and time were

bounded based on previous experiments performed by Jeong, Matsamura, Kissling, and

Bhuyan [29, 30, 33, 44].

Table 4.4: Upper and lower bounds for input parameters of FEM model

Parameter	Lower bound	Upper bound
h: Feature height (mm)	0.05	0.2
d: Gap distance of electrodes (mm)	1	20
c: Conductivity of solution (S/m)	1.66	5.94
E: Voltage drop (V)	1	5
t: Time (s)	5	30

4.3.1   Simulation Results

The simulation was run for both the prismatic protrusions and conical microfeature

geometries. The results of the 54 trials were compiled to be statistically analyzed. The

results of the trials are separated by geometry and shown in Table 4.5 and Table 4.6.

Each trial had an output of Delta *X* and Delta *Y*, which corresponded to the amount of

material removed in the *X* and *Y* direction from the tip of the microfeature. The larger the

delta value was the greater the material removal.

Table 4.5: COMSOL simulation results for prismatic protrusions

Feature Height (mm)	Gap Distance (mm)	Conductivity (S/m)	Voltage (V)	Time (s)	Delta Y (mm)	Delta X (mm)
0.05	1	1.6	1	30	8.96E-04	6.04E-03
0.05	1	1.6	5	5	7.50E-03	5.21E-03
0.05	1	5.94	1	5	5.58E-03	3.90E-03
0.05	1	5.94	5	30	4.00E-02	3.00E-02
0.05	20	1.6	1	5	8.87E-05	7.45E-05
0.05	20	1.6	5	30	2.66E-03	2.36E-03
0.05	20	5.94	1	30	1.98E-03	1.56E-03
0.05	20	5.94	5	5	1.65E-03	1.52E-03
0.2	1	1.6	1	5	2.32E-04	1.51E-03
0.2	1	1.6	5	30	5.00E-02	3.00E-02
0.2	1	5.94	1	30	4.00E-02	3.00E-02
0.2	1	5.94	5	5	4.00E-02	2.00E-02
0.2	20	1.6	1	30	8.00E-04	5.45E-04
0.2	20	1.6	5	5	6.66E-04	3.65E-04
0.2	20	5.94	1	5	4.94E-04	3.42E-04
0.2	20	5.94	5	30	1.00E-02	8.59E-03
0.05	10.5	3.77	3	17.5	4.13E-03	3.10E-03
0.2	10.5	3.77	3	17.5	5.88E-03	3.57E-03
0.125	1	3.77	3	17.5	4.00E-02	2.00E-02
0.125	20	3.77	3	17.5	2.53E-03	1.93E-03
0.125	10.5	1.6	3	17.5	2.03E-03	1.41E-03
0.125	10.5	5.94	3	17.5	7.56E-03	4.96E-03
0.125	10.5	3.77	1	17.5	1.59E-03	1.16E-03
0.125	10.5	3.77	5	17.5	7.99E-03	5.49E-03
0.125	10.5	3.77	3	5	1.37E-03	9.98E-04
0.125	10.5	3.77	3	30	8.22E-03	5.64E-03
0.125	10.5	3.77	3	17.5	4.79E-03	3.39E-03

Table 4.6: COMSOL simulation results for 3D cones

Tip Diameter (mm)	Gap Distance (mm)	Conductivity (S/m)	Voltage (V)	Time (s)	Delta Y (mm)	Delta X (mm)
0.05	1	1.6	1	30	1.50E-02	7.50E-03
0.05	1	1.6	5	5	1.00E-02	5.00E-03
0.05	1	5.94	1	5	7.50E-03	1.00E-02
0.05	1	5.94	5	30	1.20E-01	0.02
0.05	10	1.6	1	5	2.00E-03	1.00E-04
0.05	10	1.6	5	30	1.50E-02	4.00E-03
0.05	10	5.94	1	30	5.00E-03	4.00E-03
0.05	10	5.94	5	5	4.00E-03	3.50E-03
0.15	1	1.6	1	5	5.00E-03	2.00E-03
0.15	1	1.6	5	30	4.50E-02	0.04
0.15	1	5.94	1	30	5.00E-03	0.003
0.15	1	5.94	5	5	2.75E-02	0.03
0.15	10	1.6	1	30	5.00E-04	0.00E+00
0.15	10	1.6	5	5	6.00E-04	0.00E+00
0.15	10	5.94	1	5	0.00E+00	0.00E+00
0.15	10	5.94	5	30	0.017	1.50E-02
0.05	5.5	3.77	3	17.5	1.50E-02	8.00E-03
0.15	5.5	3.77	3	17.5	6.00E-03	5.00E-03
0.1	1	3.77	3	17.5	0.04	0.03
0.1	10	3.77	3	17.5	0.00E+00	0.00E+00
0.1	5.5	1.6	3	17.5	5.00E-03	5.00E-04
0.1	5.5	5.94	3	17.5	1.20E-02	5.00E-03
0.1	5.5	3.77	1	17.5	7.50E-03	0.00E+00
0.1	5.5	3.77	5	17.5	1.25E-02	7.50E-03
0.1	5.5	3.77	3	5	5.00E-03	4.00E-03
0.1	5.5	3.77	3	30	1.30E-02	1.75E-02
0.1	5.5	3.77	3	17.5	6.00E-03	2.50E-03

4.3.2 Linear Regression Model

A linear regression was performed to determine which parameters and first order interactions were statistically the most significant. Running a linear regression on the data outputs the P-values each parameter and interaction. The P-value indicates the level of confidence of the significance of a parameter to the dependent variable in the experiment. The smaller the P-value, the more significant the parameter is. A P-value under 0.05 was considered significant and worth keeping in the model. P-values that were higher than 0.05 were omitted from the optimization model as they were deemed insignificant [45]. The regression also calculated coefficients for each parameter to give a weight of importance to each parameter. The coefficients were based on the magnitude of change the parameter created on the simulation. Thus, the simulation was much more sensitive to parameters with larger magnitude coefficients as they caused more change in the output of the model. The regression data of each parameter are displayed in Table 4.7 and Table 4.8. The data from the linear regression was then used to develop an optimization model that would provide process parameters for a desired material removal.

Table 4.7: P-Values and coefficients for process parameters and interactions for
microchannel protrusion geometry

Parameter	Delta Y		Delta X	
	Coefficient	P-Value	Coefficient	P-Value
Feature Height	0.0046	0.0008	0.0023	0.0002
Gap Distance	-0.0113	0.0000	-0.0072	0.0000
Cond.	0.0046	0.0009	0.0030	0.0000
Voltage	0.0060	0.0001	0.0032	0.0000
Time	0.0054	0.0003	0.0045	0.0000
Feature Height* Gap Distance	-0.0044	0.0018	-0.0020	0.0008
Feature Height *Cond.	0.0000	0.9671	0.0002	0.6567
Feature Height *Voltage	0.0010	0.3783	-0.0001	0.8943
Feature Height *Time	0.0018	0.1253	0.0011	0.0291
Gap Distance *Cond.	-0.0036	0.0071	-0.0020	0.0008
Gap Distance *Voltage	-0.0049	0.0008	-0.0021	0.0006
GD*Time	-0.0041	0.0031	-0.0034	0.0000
Cond.*Voltage	-0.0010	0.3978	-0.0003	0.4546
Cond.*Time	-0.0001	0.9274	0.0008	0.1010
Voltage*Time	0.0010	0.3875	0.0007	0.1296
Feature Height * Feature Height	-0.0018	0.5373	-0.0004	0.7071
Gap Distance * Gap Distance	0.0145	0.0003	0.0072	0.0000
Cond.*Cond.	-0.0020	0.4907	-0.0006	0.6139
Voltage*Voltage	-0.0020	0.4896	-0.0004	0.7007
Time*Time	-0.0020	0.4907	-0.0004	0.6969

Table 4.8: P-Values and coefficients for process parameters and interactions for 3D conical geometry

Parameter	Delta Y		Delta X	
	Coefficient	P-Value	Coefficient	P-Value
Tip Diameter	-0.0048	0.003	0.0018	0.144
Gap Distance	-0.0128	0.000	-0.0067	0.000
Conductivity of Solution	0.0056	0.001	0.0017	0.162
Voltage	0.0113	0.000	0.0055	0.000
Time	0.0097	0.000	0.0031	0.016
Tip Diameter*Gap Distance	0.0039	0.016	-	-
Tip Diameter*Cond.	-0.006	0.001	-	-
Tip Diameter*Voltage	-	-	0.0043	0.003
Tip Diameter*Time	-0.0061	0.001	-	-
Gap Distance*Cond.	-0.0048	0.004	-	-
Gap Distance*Voltage	-0.0088	0.000	-0.0034	0.015
Gap Distance*Time	-0.0065	0.000	-	-
Cond.*Voltage	0.0064	0.000	-	-
Cond.*Time	0.0031	0.045	-0.0029	0.035
Voltage*Time	0.009	0.000	-	-
Gap Distance*Gap Distance	0.0097	0.000	0.0052	0.009

The coefficients from the linear regression were used to develop two transfer functions to model the material removal of the features. The transfer functions were built upon the relevant process parameters and their coefficients. The function would output an amount of material removal based on the process parameters that were chosen. The transfer functions could also be used to optimize and generate process parameters for a desired amount of material removal. In addition to the parameter optimization, the transfer functions provide extremely quick calculations compared to finite element processes. The transfer functions for material removal in Y and in X for the prismatic protrusions are listed in Equations (4.4) and (4.5). The transfer functions for the conical features are shown in Equations (4.6) and (4.7). Only the statistically relevant parameters (P-values less than 0.05) were used for this model. The variables displayed in the following equations are the same that were used in Equation (4.1).

$$\Delta Y = 0.0048 + 0.0046h - 0.0113d + 0.0046\,r + 0.006E + 0.0045t$$
$$- 0.004hd - 0.0036dr - 0.0049Ed - 0.0041dt + 0.0088d^2 \tag{4.4}$$

$$\Delta X = 0.003 + 0.23h - 0.0072d + 0.003r + 0.0032E + 0.0045t + 0.002hd$$
$$+ 0.0011ht - 0.002dr - 0.0021dE - 0.0034dt + 0.0058d^2 \tag{4.5}$$

$$\Delta Y = 0.008 - 0.0048h - 0.0128d + 0.0056\,r + 0.0113E + 0.0097\,t$$
$$- 0.0039hd - 0.006hr - -0.0061ht - 0.0048dr - 0.0088dE \tag{4.6}$$
$$- 0.0065dt + 0.0064rE + 0.009Et + 0.0097d^2$$

$$\Delta X = 0.0045 + 0.0018h - 0.0067d + 0.0017r + 0.0055E + 0.0031t$$
$$+ 0.0043hE - 0.0034dE - 0.0029rt + 0.0052d^2 \tag{4.7}$$

4.3.3   Regression Model Verification

The statistical model was used to optimize process parameters for a desired amount of material removal. The parameters were then input into the FEM model to compare the difference.

A desired amount of material removal in X and Y was calculated using the transfer functions (Equations (4.4) through (4.7)). The values for the five parameters were optimized to achieve the best surface finish without the destruction or harm of the microfeature array. This was tested by optimizing various sets of parameters to remove a layer thickness of 0.5 μm and 1.0 μm. The optimized parameters were then plugged into the finite element model to compare the computed layer thickness removal to the desired amount. The prismatic protrusion geometry was tested. The optimized parameters from the transfer functions are displayed below in Table 4.9, along with the computed material removal from the COMSOL model.

Table 4.9: Optimized parameters from transfer function tested against finite element model for prismatic protrusions

| Optimized Parameters | | | | | | Calculation From Model | | | |
Feature Height (mm)	Gap Distance (mm)	Conductivity of Solution (S/m)	Voltage (V)	Time (s)	Desired layer thickness removal (μm)	Thickness removed in FEM model in Y (μm)	Thickness removed in FEM model in X (μm)	Magnitude difference for Y (μm)	Magnitude difference for X (μm)
0.2	19.62	1.62	1.25	20	0.5	0.60	0.41	0.10	-0.09
0.2	19.24	1.6	3.18	7	0.5	0.51	0.37	0.01	-0.13
0.2	19.14	4.87	1.7	9	1.0	1.01	0.579	0.01	-0.421
0.2	20	1.69	2.1	17	1.0	1.12	0.972	0.12	-0.028
0.05	20	3.76	1.01	15	0.5	0.552	0.349	0.052	-0.151
0.05	20	4.39	1	10	0.5	0.427	0.271	-0.073	-0.229
0.05	9.42	2.85	4.83	7	1.0	1.06	0.803	0.06	-0.197
0.05	20	2.55	2.24	17	1.0	0.95	0.596	-0.05	-0.404

The COMSOL simulation on average calculated a 0.03μm difference in layer thickness removal than the transfer functions predicted in the Y and -0.20 μm difference in the X direction. The X-axis and Y-axis have different material removal rates due to high aspect ratio of the microfeature. There is a higher potential difference at the tips of the microfeatures than at the base. The difference in potential created higher surface charge densities at the tips compared to the base or the sides of the feature leading to more material leaving from the top of the feature (in the Y- axis).

4.3.4 Key Process Parameters and Trends

The current density on the anode surface was highest at the corners of the protrusions and negligible along the bulk surface. Thus, over time the high current density caused the corners to erode away faster than the rest of the surface, and transforming the rectangular prisms into triangular and pyramidal shapes. The largest amount of feature deformation

was 0.05 mm in the Y and 0.03 mm in the X, which occurred at low gap distances and high voltages. The 0.2 mm tall protrusions had higher material removal rates than the 0.05 mm features. The increase in surface area allows for more metal ions to react with the electrolyte solution, as well as providing areas of higher current density. It is worth noting that **w**hile the 0.2 mm features had higher material removal rates, it only had a reduction in height of 25%, whereas the shorter 0.05 mm feature had a reduction in height of 60%..

The length of time and conductivity of the solution had increasing effects on the deformation of the features. This was expected, as the longer the workpeice underwent the electropolishing process, the more material would be removed over time. Also, with a higher conductivity solution, larger current densities appeared on the features which eroded them faster.

While all five factors had extremely low P-values and affected the amount of erosion of the microfeatures, gap distance was by far the most significant. As gap distance decreased, the material removal rate increased more so than when any other variable was increased independently. This occurred because the interactions between gap distance and any other variable were the only interactions with a P-value less than 0.05. This information is noted in Table 4.7. To further illustrate the significance of gap distance, the interactions between gap distance, feature height, and voltage are shown below in Figure 4.11 and Figure 4.12.

Interaction between gap distance and feature height on deformation in Y
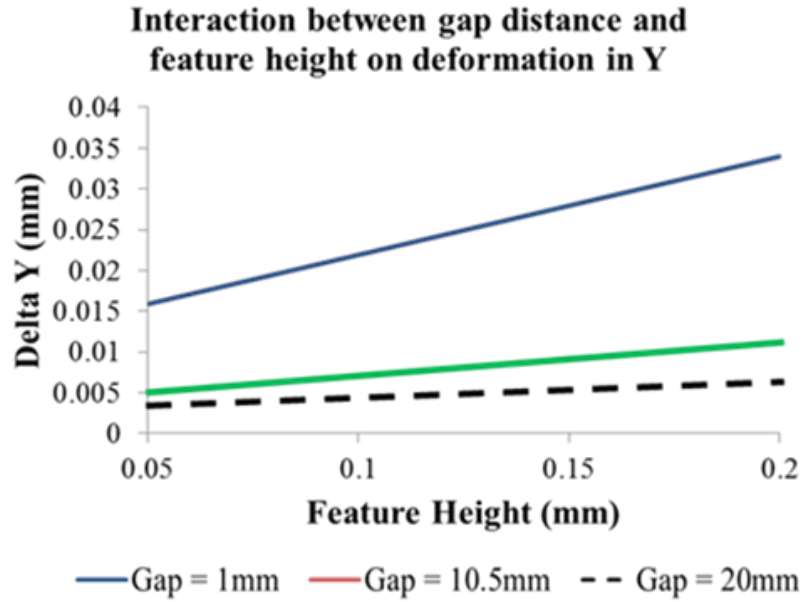
Figure 4.11: The plot shows that as gap distance decreases, the effect of feature height on material removal increases.

Interaction between gap distance and voltage on deformation in Y
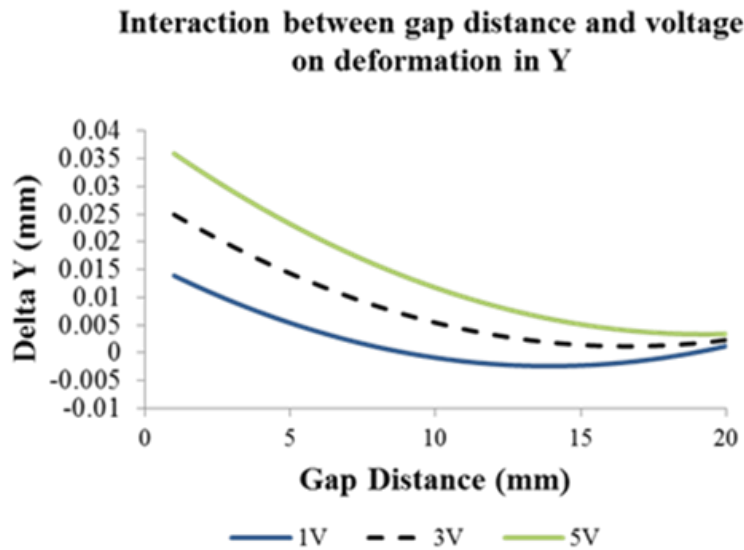
Figure 4.12: The plot shows that as gap distance increases, the effect of increasing voltage on material removal becomes negligible.

The effect that feature height and voltage had on the material removal rate increased as the gap distance shrunk. As gap distance increased, the effects of varying voltage converged and became negligible. The decreasing effect of voltage was predicted as increasing gap distance reduces the effective drop between the electrodes, which in turn

reduce the current density in the workpiece. The effect of feature height on material removal nearly tripled as gap distance changed from 20 mm to 1 mm. The reduced effect of feature height is explained by the fact that the electrochemical reaction occurs at a faster rate when the electrodes are closer to each other. As the electrodes get farther away from each other, the potential drops dramatically causing the reaction rate slows down to such a slow rate that increasing feature height became negligible compared to the drop in potential. When the electrodes were 20mm apart, the effects of feature height, voltage, conductivity of the solution, and time were negligible because the reaction rate was so slow. When the electrodes were 1 mm apart the reaction rate was very high, thus making it also much more sensitive to the effects of the other parameters.

This study shows that while material removal can be quantified by an equation, it is not effective at the microscale. Specifically, while the volume removed can be calculated, the exact area from where the material is removed is not stated or quantified by the equation. The problem is derived from the fact that the equation assumes a uniform surface charge density along the workpiece. This assumption is then coupled with the fact that microfeature arrays on bulk surfaces have extremely high surface charge concentration at the tip of the features relative to the rest of the workpiece. Also, the equation assumes each parameter is equally significant to the material removal rate, but this is not true. The trials show that gap distance is not only the most important factor in material removal, but is also co-related to the other parameters. Thus, as gap distance changes, the effects of the other variables change as well.

4.4   Electropolishing experimentation

Once the electropolishing model was developed, it was used to optimize parameters to polish the micro-molds. Both the 2D and 3D array micro-molds were machined using the techniques found in Chapter 3. Several tests were performed with both geometries to examine the effectiveness of electropolishing as a polishing technique as well as the accuracy of the model. The surface roughness of microfeatures was measured before and after the polishing to test the polishing technique. For the 2D geometry, the microchannels were examined, as those were the most delicate features. For the 3D conical geometry, the roughness of the tips of the cone was the most important features, as the tips were used to form the orifices in the mold, and were also the smallest feature of the part.

4.4.1   Electropolishing Setup

The electropolishing was performed using a setup developed in the lab. A 5V DC power supply (Topward 6303D) was used to provide current to the system. The positive terminal was connected to the anode workpiece. The workpiece was a piece of machined 360 brass. The negative terminal was connected to the cathode tool. The tool was a machined piece of machined copper with a flat face that faced the workpiece. The workpiece was situated in a glass beaker that was filled with an electrolyte solution (Aqueous H_3PO_4). The cathode tool was fixed to a motor controlled linear stage (Sherline 8540). The stage was raised and lowered through computer control. The linear stage allowed for precise control over the gap distance between the cathode and anode (0.001" resolution). An illustration of the setup is depicted in Figure 4.13.
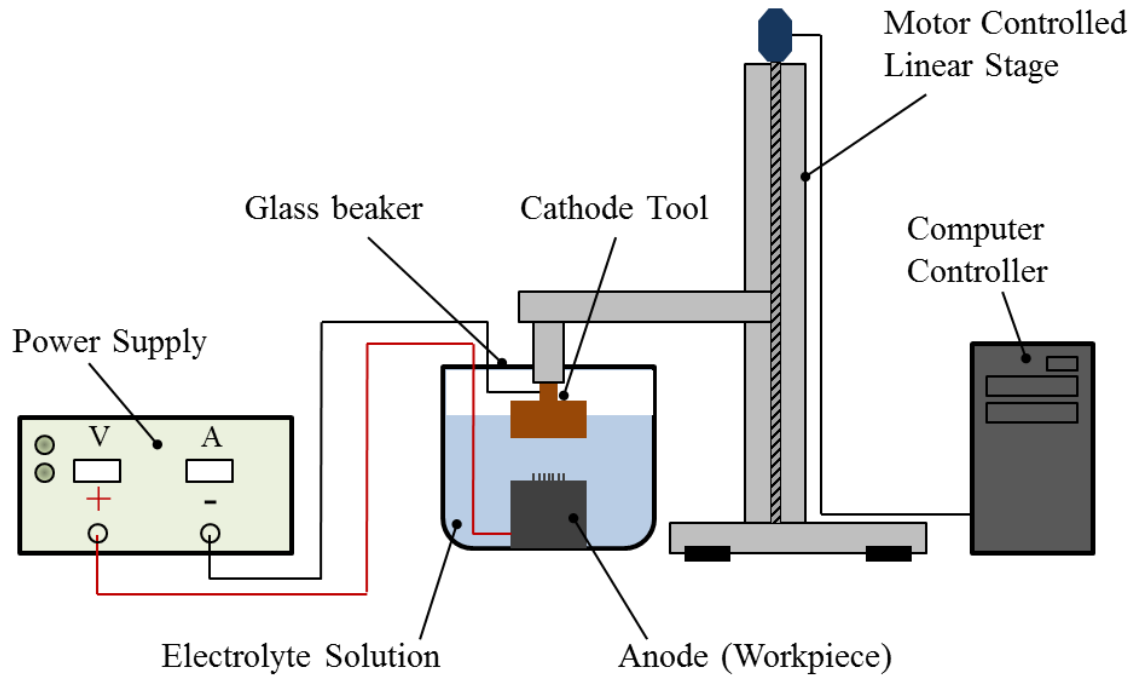
Figure 4.13: The electropolishing setup consisted of a power supply, electrolyte solution, and linear motion controlled stage to hold precise gap distances between the tool and workpiece.

4.4.2 Electropolishing Experimental Procedure

The electropolishing experiments were performed using the setup shown in Figure 4.13. The setup was performed under a ventilated fume hood. This was a safety precaution that was taken because noxious gasses are emitted during the reaction. The actual setup used for experimentation is shown below in Figure 4.14.
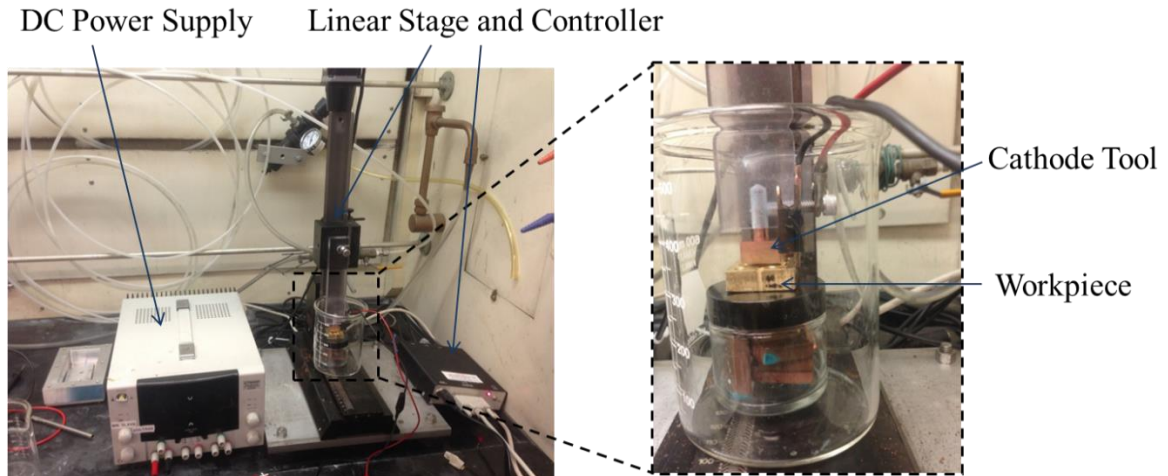
Figure 4.14: The electropolishing setup used to perform the polishing experiments in the study was conducted under a fume hood.

The first step was to fix the workpiece to the glass beaker. A piece of double sided tape was placed at the bottom of the part and attached to the glass beaker to prevent movement during the experiment. The cathode tool was fixed into the linear stage and held with a set screw. The same conductive touch-off technique used to zero tools for micromachining in Chapter 3 was used to zero the cathode tool to the top of the workpiece. Once the tool was registered, it was raised to the desired gap distance height. Afterwards, the electrolyte solution was prepared. The solution was an aqueous H_3PO_4 mixture. This meant that the solution was comprised only of water and H_3PO_4. The two components were poured and measured separately in separate beakers to create the desired concentration. The acid was then added to the water and mixed together with a glass stirring rod very slowly for 1 minute. The electrolyte solution was then poured slowly into the beaker until both the tool and the workpiece were submerged in the solution. The DC power supply was then set to the desired testing voltage. Next, the terminals from the DC power supply were connected to complete the circuit. Alligator clips were used to positive terminal to the workpiece, and the negative terminal to the

cathode tool. The experiment was timed using a stopwatch. The power supply was turned on and simultaneously the stopwatch was started. Once time was up, the power supply was turned off and the cathode tool was raised out of the electrolyte solution. The electrolyte solution was poured into a waste beaker, and the workpiece and cathode tool were placed into a bath to be cleaned.

To remove debris and clean the parts, the workpiece and tool were placed in a beaker of isopropyl alcohol that was placed in an ultrasonic cleaner (Fischer Scientific FS6) for 5 minutes. Afterwards, the items were dried using compressed air. The cathode tool was placed back into the fixture to be used for the next experiment, and the workpiece was stored to be measured later.

4.4.3   Process parameter generation

To test the 2D geometry, small test coupons containing the microchannel protrusions were fabricated. The coupons were 18.8 mm long and 8 mm wide and contained six 100 μm protrusions. The features were created using the same micromachining techniques used in Chapter 3. Eight coupons were tested; four with 200 μm tall features and four with 50 μm tall features.

The ZYGO was used to measure the initial surface roughness of the microchannel protrusions. The initial surface roughness of the 2D microchannel protrusion coupons are listed in Table 4.10.

Table 4.10: Initial surface roughness of 2D array coupons

Coupon	Feature height (µm)	Average Ra (µm)
1	200	1.762
2	200	2.369
3	200	1.539
4	200	2.194
5	50	1.195
6	50	1.255
7	50	1.258
8	50	1.146

SPI surface roughness standards for mold cavities were used as the specifications to characterize the parts. The SPI standards are displayed below in Table 4.11. For the purpose of this study, an SPI level of B-1 was set as a target. Levels above B-1 were typically obtained using diamond scribes on stainless steels, and were deemed not attainable through electropolishing brass molds [11].

Table 4.11: SPI mold finish standards

SPI Finish	Ra (µm)
A-1	0.0254
A-2	0.0508
A-3	0.127
B-1	0.254
B-2	0.254
B-3	0.381
C-1	0.304
C-2	0.762
C-3	1.066

A B-1 SPI level requires a R_a value of 0.25 µm. Thus, the desired amount of material removal determined by subtracting 0.25 µm from the surface roughness measured from the coupons prior to polishing. The desired volume removal was determined by

calculated by multiplying average material removal (MR_a) by the surface area of the features. The expression is derived from Faraday's law and is shown in Equation (4.8).

$$Vol_{removed} = MR_a \cdot A_S = \frac{A_s \cdot E \cdot t \cdot N}{C \cdot n \cdot \rho \cdot d \cdot r} \tag{4.8}$$

The average material removal (MR_a) is derived through by subtracting the measured R_a and the desired R_a. The equation for R_a is displayed below in Equation (4.9), where n is the number of sampled points, and y_i is the height from the mean line of the surface. Thus, R_a is the arithmetic average of the heights from the mean line of the surface. Assuming that the material removal from the polishing process will occur on the peaks of the surface, the y_i values will decreases by the desired material removal (MR). Thus the desired surface roughness can be expressed by Equation (4.10). Subtracting Equations (4.9) and (4.10) yields the average material removal, which is expressed by Equations (4.11) and (4.12). The MR_a value was then multiplied by the surface area of the features to determine the volume removal. The MR_a value was inserted into the statistical to determine corresponding process parameters.

$$R_a = \frac{1}{n}\sum_{i=1}^{n} y_i \tag{4.9}$$

$$R_a desired = 0.25 = \frac{1}{n}\sum_{i=1}^{n}(y_i - MR) \tag{4.10}$$

$$R_a - R_a desired = \frac{1}{n}\sum_{i=1}^{n} y_i - \frac{1}{n}\sum_{i=1}^{n}(y_i - MR) \tag{4.11}$$

$$R_a - R_a desired = \frac{1}{n}\sum_{i=1}^{n} MR = MR_a \tag{4.12}$$

75

Once the desired material removal was calculated, the electropolishing model was used to calculate process parameters to be used to polish the parts to the desired surface roughness. The calculate process parameters for the desired amount of material removal for the 2D coupons are listed below in Table 4.12.

Table 4.12: Optimized parameters generated from model for 2D coupons

| Coupon | Feature height (µm) | Desired Material Removal (µm) | Calculated Parameters | | | |
			Gap Distance (mm)	Conductivity of Solution (S/m)	Voltage (V)	Time (s)
1	200	1.512	19.72	2.15	2.42	22.92
2	200	2.119	1.12	5.94	2.70	16.32
3	200	1.2889	9.88	3.16	1.29	23.53
4	200	1.944	7.37	1.60	2.44	30
5	50	0.945	20.00	5.94	3.61	30
6	50	1.005	10.73	1.60	1.74	18.75
7	50	1.008	12.80	3.59	1.13	27.91
8	50	0.896	1.50	3.55	2.70	12.00

4.4.4 Error propagation analysis

The error propagation of the average material removal (MR_a) during the experiments was calculated and evaluated using Kline Mcclintock's uncertainty propagation [46]. The partial derivatives of Faraday's law, Equation (4.8), were computed to calculate the uncertainties of each experimental variable. The equation has a total of 4 variables that were manipulated experimentally: Voltage (E), time (t), gap distance (d), and resistivity of the solution (r). The variables $N, C, n,$ and ρ were material or physics based constants and were combined together to form the proportionality constant (K). The resulting equation is shown below in Equation (4.13).

$$MR_a = \left(\frac{E \cdot t}{d \cdot r} \right) K \tag{4.13}$$

Taking the five partial derivatives of the variables in the parentheses of Equation (4.13) yields the equations that were used to calculate the amount of error from each part of the experimentation. The partial derivatives are displayed below in Equations (4.14) through (4.17).

$$\frac{\partial E}{\partial MR_a} = \frac{t}{d \cdot r} K \cdot \partial E \tag{4.14}$$

$$\frac{\partial t}{\partial MR_a} = \frac{E}{d \cdot r} K \cdot \partial t \tag{4.15}$$

$$\frac{\partial d}{\partial MR_a} = -2 \cdot \frac{E \cdot t}{d^2 \cdot r} K \cdot \partial d \tag{4.16}$$

$$\frac{\partial r}{\partial MR_a} = -2 \cdot \frac{E \cdot t}{d \cdot r^2} K \cdot \partial r \tag{4.17}$$

The partial terms at the end of each equation represents the uncertainty associated with the respective variable. The voltage had an error of 0.02 V based on the resolution of the power supply. The time was given an uncertainty of one second. The gap distance had an uncertainty of 0.0025 mm based on the resolution of the linear motion controller. The resistivity of the electrolyte solution was determined by the concentration of the electrolyte solution. The uncertainty was determined by calculating the propagated error from measuring the acid and water components of the solution. The equation for the resistivity of the solution is shown in Equation (4.18), where v_a is the volume of acid (ml), and v_w is the volume of water (ml).

$$r = -3044.3 \left(\frac{v_a}{v_a + v_w} \right) + 777.22 \tag{4.18}$$

The partial derivatives of Equation (4.18) were calculated and shown in Equations (4.19) and (4.20). The uncertainty values, dv_a and dv_w, were the uncertainty of from measuring the volume of the liquids using a graduated cylinder (1ml). The uncertainty of the

resistivity was the square root of the sum of the squares of the variables and is shown in

Equation (4.21).

$$\frac{\partial v_a}{dr} = -3044.3 \left(\frac{v_w}{(v_w + v_a)^2} \right) dv_a \tag{4.19}$$

$$\frac{\partial v_w}{dr} = -3044.3 \left(\frac{v_a}{(v_w + v_a)^2} \right) dv_w \tag{4.20}$$

$$dr = \sqrt{ \left(-3044.3 \frac{v_a}{(v_w + v_a)^2} dv_w \right)^2 + \left(-3044.3 \frac{v_w}{(v_w + v_a)^2} dv_a \right)^2 } \tag{4.21}$$

The total propagated error for MR_a was calculated by taking the square root of the sum of

the squares of Equations (4.14) through (4.17). The uncertainty for each experimental

item is listed in Table 4.13.

Table 4.13: Uncertainties for experimental apparatus

Apparatus	Model	Uncertainty
DC Power Supply	Topward 6303D	0.02 V
3 Axis CNC mill	Prototrak SMX	0.01 mm
Graduated Cylinder(50 ml)	Fischer Scientific 50 ml	1 ml
Motion Controller Stage	Sherline 8540	0.0025 mm
Digital Stopwatch	iPhone 5	1 s

4.4.5 Results

Each test coupon was subjected to the polishing test outlined in section 4.4.2, and was

measured on the ZYGO to determine the surface roughness of the polished part. Before

and after images of the sample parts are shown below in Figure 4.15. An example of the

surface profile from the ZYGO is shown below in Figure 4.16.
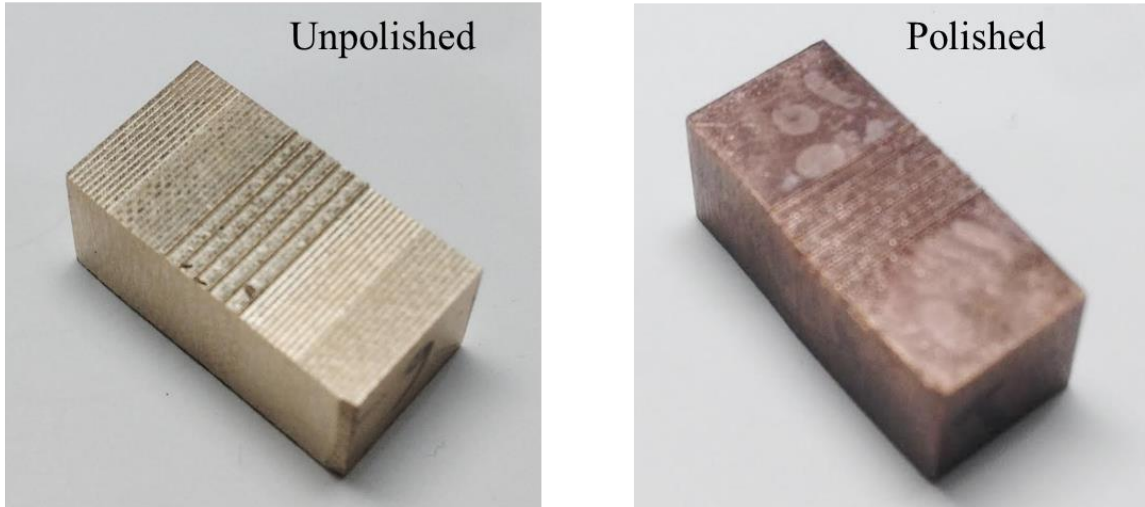
Figure 4.15: After polishing, the part became smoother. The machine marks were removed while keeping the microchannels intact.
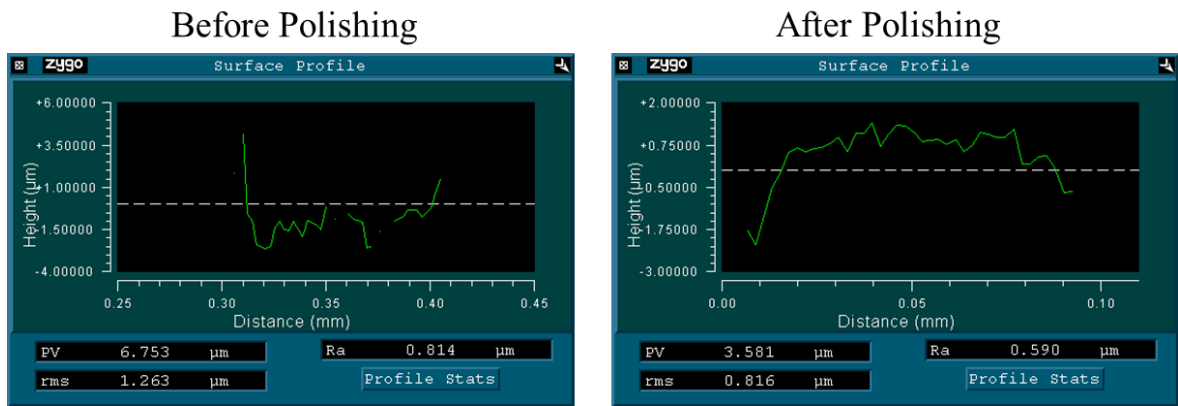
Figure 4.16: The surface profile of the tip of the microfeature was smoothened by the polishing process. Also, the burr on the edges was removed.

The average surface roughness of the tips of coupons before and after polishing is displayed in Figure 4.17 and Figure 4.18. The calculated experimental errors for each trial are listed in Table 4.14 and Table 4.15. The propagated experimental errors vary from trial to trial based on the process parameters used. Higher experimental errors were observed during trials at smaller gap distances. The error from the uncertainty of the gap distance was magnified at smaller gap distances and caused larger experimental error

calculations.
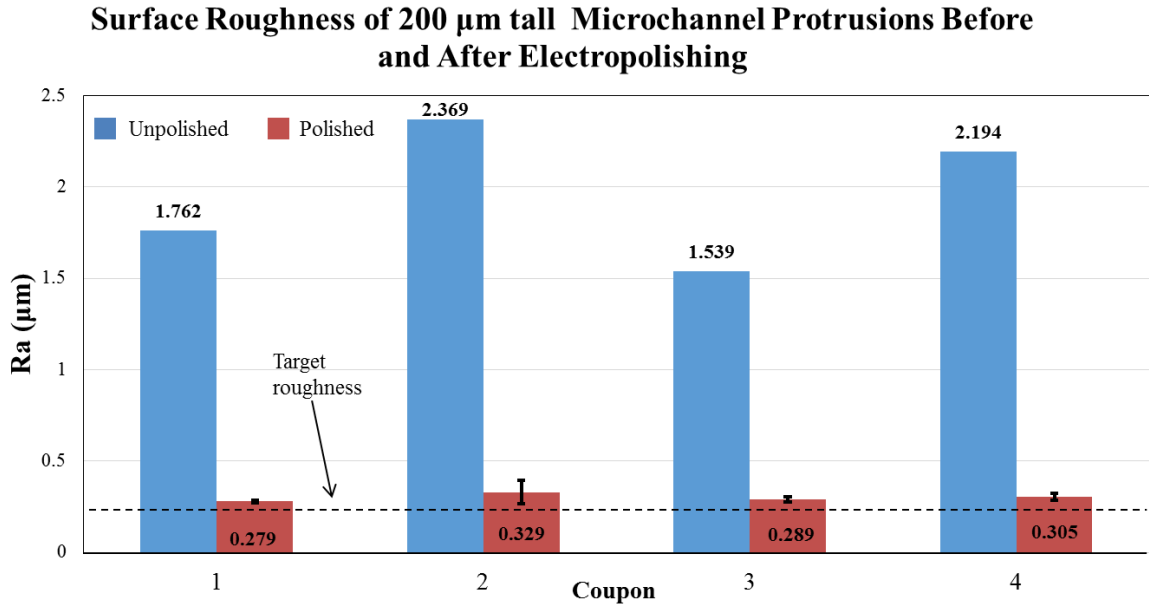
Figure 4.17: The surface roughness of the 200 μm tips was reduced to an average of 0.300 μm. The numerical values listed are the surface roughness values.

Table 4.14: Experimental error values for 200 μm protrusions

Coupon	Error (μm)
1	8.41E-03
2	6.43E-02
3	1.40E-02
4	1.80E-02
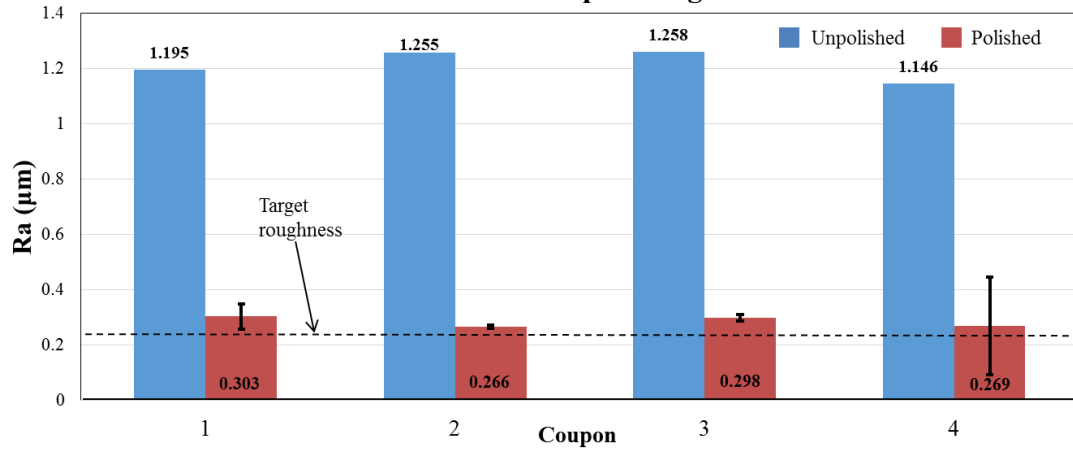
Figure 4.18: The surface roughness of the 50 µm tips was reduced to an average of 0.284 µm. The numerical values listed are the surface roughness values.

Table 4.15: Experimental error values for 50 µm protrusions

Coupon	Error (µm)
1	4.55E-02
2	7.08E-03
3	1.13E-02
4	1.76E-01

4.4.6 Comparison of material removal predictions and experiments

After the coupons were polished, they were measured on the microscope (Nikon microphoto FXL) to measure the final shape of the microfeatures, as well as compare the material removal loss to the predictions from Faraday's law and the COMSOL model. Faraday's law assumed a uniform surface charge distribution, thus the material removal was constant along the feature. The COMSOL model accounted for a distribution of surface charge density and therefore predicted higher material removal rates near the tips of the features. The experimental results showed the tips of the features experienced higher material removal rates, but at larger magnitudes than what COMSOL predicted. A

comparison of material removal predictions between Faraday's law, COMSOL, and experimental results is illustrated in Figure 4.19.

Faraday's Law   COMSOL Model   Experimental result
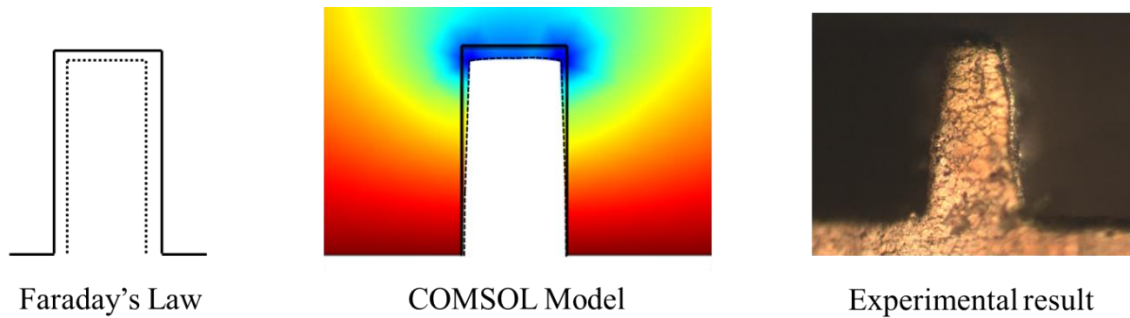
Figure 4.19: Comparison between the material removal results from experimentation and the predictions by Faraday's law and the COMSOL model.

The widths of the channel were measured periodically every 50 μm from the base, and compared to the final microchannel widths predicted by the COMSOL model and Faraday's law. Faraday's law computed an overall volume of material removal over the entire workpiece. The overall material removal was assumed to be evenly distributed about the surface. Thus, the thickness reduction stayed constant as height increased. The data was normalized to illustrate the effect of microfeature height and material removal. The results of the four trials of the 200 μm tall features are shown in Figure 4.20.
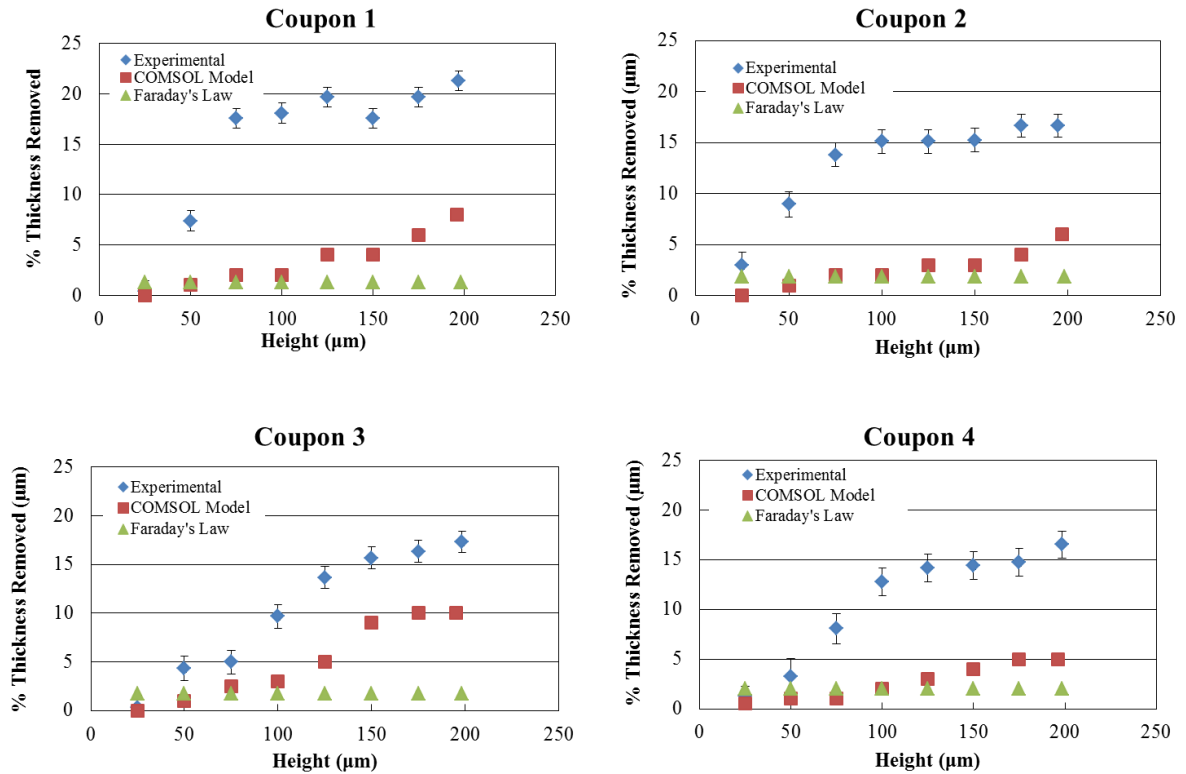
Figure 4.20: Thickness removal vs height comparison between Faraday's law, COMSOL model, and experimental results for 200 μm coupons.

In each of the cases, the material removal during the experiments was higher than the predicted amount from the COMSOL model and Faraday's law. Both the model and experiments show that more material is removed from the top of the feature compared to the bottom of the feature. The trend was expected as microfeatures have higher surface charge densities near the top of the feature compared to the bottom of the feature. Near the base of the features both the model and the experiments followed similar trends. After a height of 100 μm the material removal in the experiments increased by a factor of 2 to 3 compared to the expected material removal calculated by the model. While the magnitude of material removal increased, the experiments still followed the same increasing trend that the COMSOL model predicted.

4.5   Discussion of Experimental Results

4.5.1   Material Removal

The COMSOL model and Faraday's law underestimated the amount of material removal on the features. The model underestimated the amount of material removal by a factor of 2 at the top of the microfeatures. Errors attributed to the disparity between the two can be explained by a number of factors. Firstly, the COMSOL model also assumes perfect geometry in the microfeature array. The microfeatures in the array are comprised of perfectly straight edge and flat surfaces. There was no initial surface roughness or variation among the microfeatures. The machined features exhibited quite the contrary. In addition to having burr and an initial surface roughness, the machined features also exhibited variation from feature to feature within the same array. The variation is due to the resolution of the CNC stages (0.005 mm), tool wear, thermal effects and heat generation, and vibrations and chatter. The widths of the microfeatures were 100 μm ± 5 μm within a feature array. The variation in material removal from feature to feature is observed visually in Figure 4.21, and illustrated graphically in Figure 4.22.
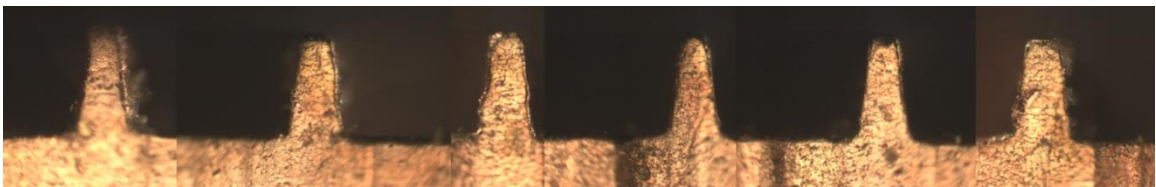
Figure 4.21: Side view of 200 μm tall microfeature array after polishing
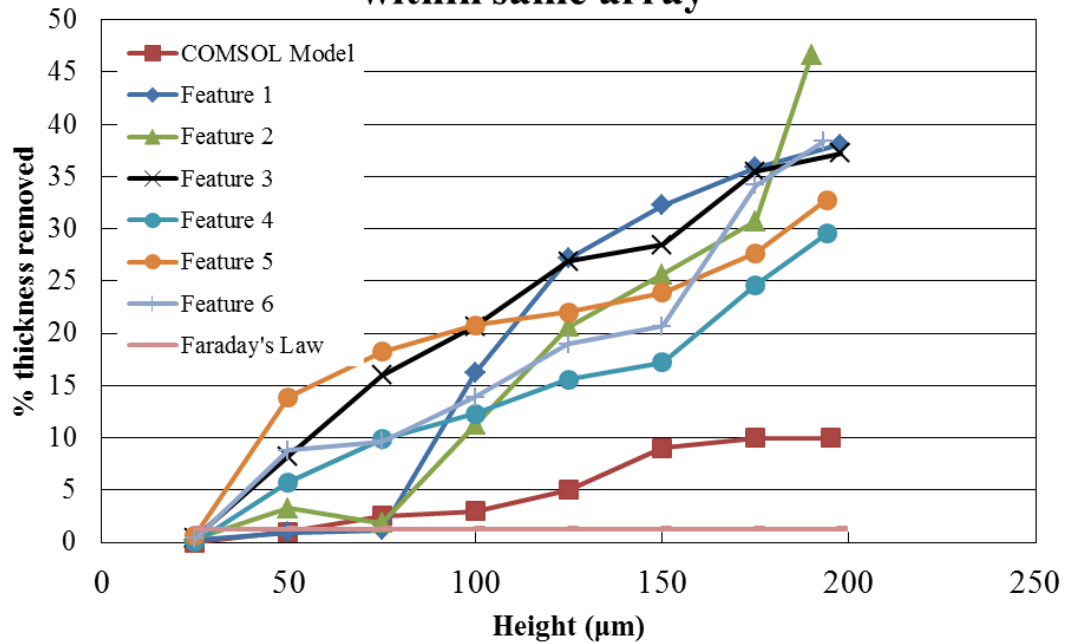
Figure 4.22: Thickness removal vs height comparison between COMSOL model and 200 µm tall microfeatures in same array

The variation from feature to feature due to the stochastic nature of the fabrication method makes it difficult to relate the COMSOL model predictions. However, even though the features vary from each other, all of the microfeatures experienced material removal rates two to four times larger in magnitude than the model predicted. Also, the COMSOL model was more accurate than Faraday's Law as it predicted higher material removal rates near the top of the features. Reasons for the higher levels of material removal encountered during experimentation can be attributed to the grain structure and molecular make up of the material.

The COMSOL model does not take into account the molecular make-up of the workpiece material. Two-phase brass (360 brass) was used for experimentation. The brass contains a 61.15% copper, 35.5% zinc, 3% lead, and 0.35% iron. The addition of

lead into the workpiece is used to aid in machinability, but complicates reaction rate of the polishing process. The addition of lead makes the metal two-phase, introducing different material properties that alter the electrochemical reaction rate. With the alloy in two phases, ions from each phase have different valence shell properties. The different ions have different and unpredictable material removal rates that are not accounted for in the model.

In addition, the model did not take into account the grain structure of the material. Grain structure is an important aspect in electrochemical polishing as both the size and orientation of the grains can affect the material removal rates. Smaller grain sizes lead to faster etching rates as there are more active grain boundaries that allow more metal ions to leave easier [47]. Atoms on the grain boundaries share loose bonds that require lower activation energies to leave. Also, the grain orientation affects the etching rate, as different crystal directions can etch orders of magnitude faster than others. The anisotropy of brass poses a huge challenge. The average grain size for two phase brass was found to be between 55 μm and 200 μm [48-50]. Because the grain size is on the same order of magnitude as the microfeatures, it is difficult to obtain a large distribution of different grain orientations along the surface of the feature. Thus, the effect that anisotropy has on etching rate is magnified as there are fewer grains on the feature. This would explain the large increases in material removal experienced during experimentation. The COMSOL model did not account for the anisotropic behavior of the material, and therefore underestimated the material removal. The scaling effect of anisotropy on the microfeatures is illustrated in Figure 4.23
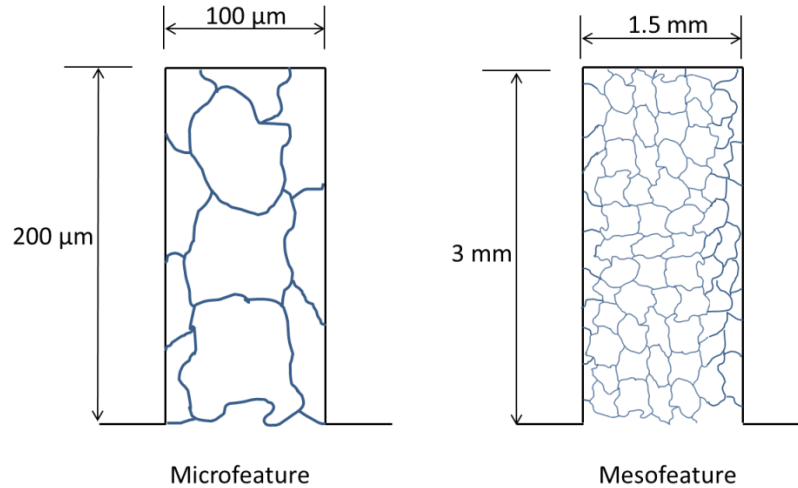
Figure 4.23: Illustration of the anisotropic scaling effects with microfeatures. Microfeatures have fewer grains along the surface and are susceptible to radical material removal rates during electropolishing.

The model was computed in 2D as opposed to 3D in an effort to reduce computational time. A drawback from modeling in 2D was that the model does not take into account the corner edges of the feature in and out of plane. Higher current densities are located on these edges and corners and lead to higher material removal rates, but are not accounted for in the model. The difference between modeling in 2D and 3D is illustrated below in Figure 4.24. Also shown in the figure is a top view of a microchannel that depicts how the ends of the feature experienced more material removal due to the higher current densities in those areas. This characteristic was not able to be captured in the 2D model.
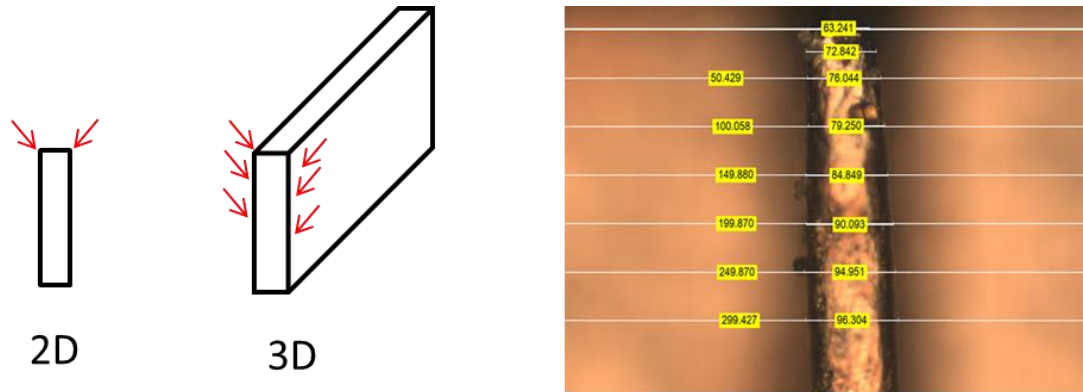
Figure 4.24: Modeling in 2D versus 3D neglects the high surface charge densities (noted by red arrows) on the edges and ends of the feature (in and out of plane). The experiments confirm this as more material was removed from the ends of the feature as opposed to the middle (right).

The COMSOL model is a more accurate alternative to Faraday's law when predicting material removal in high aspect ratio microfeature arrays. This is due to the fact that it accounts for the charge distribution along the surface of the part. However, the model's omission of material composition and grain structure lead to underestimation of the material removal rates. In addition, the 2D model does not capture variations in surface charge densities in and out plane, leading to lower predicted material removal. The model does however serve as a basis for modeling and predicting electropolishing and illustrates the challenges involved with forecasting a complex multiphysics reaction.

4.5.2 Surface roughness enhancement

The results from the experiments showed that the surface roughness of microfeature molds can be reduced through electropolishing. The statistical model generated parameters that were used to polish the microfeatures to a B-1 SPI rating (R_a of 0.25 μm). While the model did provide process parameters that lowered the surface roughness without altering or damaging the tips of the microfeatures, the surface roughness of the

arrays never got to a B-1 rating. The smoothest surface attained over any of the features was a R_a of 0.266 µm. An average error of 0.042 µm was found for the 2D arrays.

Not only did the electropolishing process smooth the surface of the micro features, it also removed the burr. Burr removal was evident from the ZYGO images and is exemplified in Figure 4.25.
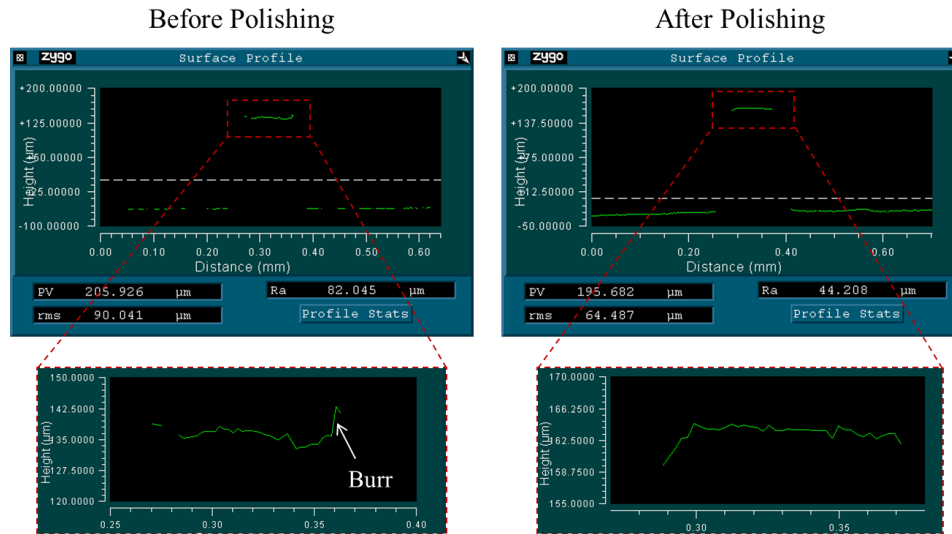
Figure 4.25: Electropolishing was shown to be an effective burr removal technique for the microfeatures.

In addition to smoothing the tips of the microfeatures, the base surface of the part was also smoothened. The reduction in surface roughness was observed through the disappearance of the machine marks after polishing and is show below in Figure 4.27.

Before Polishing   After Polishing
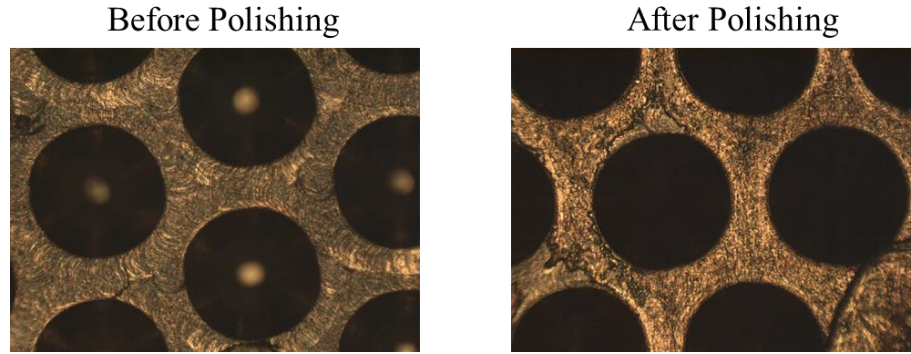
Figure 4.26: The machine marks left by the cutting tools disappeared after the polishing process and left a smoother surface.

The process parameters generated from the model did not cause any harm or deformation to the features. As a quick test, a sample part was polished for 2 minutes at 5V, 20% H_3PO_4 solution, with a 1 mm gap distance (Highest process parameters for an extended period of time). The corners of the microfeature were etched away and were deformed. A surface profile of the part is shown below in Figure 4.27.
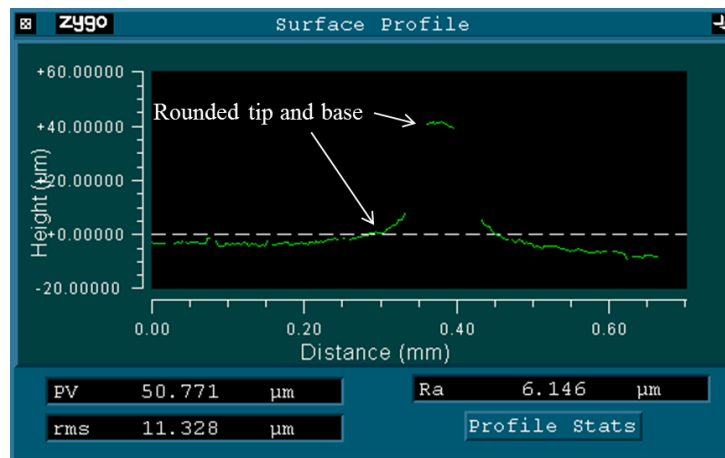
Figure 4.27: The tip and corners of the 50 µm feature deformed and rounded over due to being over-polished.

In addition to being modeled in 2D, the model also did not encompass the surface profile of the machined parts. As depicted below in Figure 4.28, the computational model simulates the surface of the features as perfectly straight lines and flat surfaces. It was not

possible to incorporate the actual roughness into model as a mesh would not generate in the microscopic hill and valleys that comprise the surface.
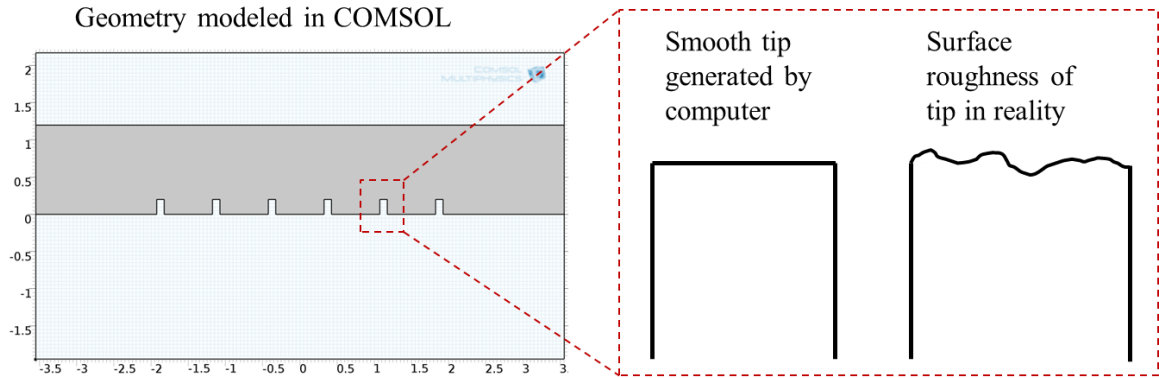
Figure 4.28: The microscopic peaks and valleys on the tip of the microfeatures could not be generated in the computer model.

4.6   Application to conical array

The model and methods used to polish the coupon were implemented and used to polish the tips of the 3D conical array. The 3D conical array was machined as a set of 31 cones. The initial surface roughness of the tips of the cones was measured using the ZYGO. In an effort to save time, tips were numbered and randomly selected for measurement. Measurements were taken until the confidence interval of the measurements had a percent change less than 5%. The mean of the surface roughness measurements was used to calculate the desired material removal. Two arrays of 50 μm wide tips and 85 μm were cut and measured for their initial surface roughness. The average surface roughness of the tips is shown in Table 4.16.

Table 4.16: Average surface roughness of tips of cones before polishing

Coupon	Tip Radius (μm)	Average Ra (μm)
1	50	0.456
2	50	0.482
3	85	0.474
4	85	0.466

The model was then used to generate process parameters to achieve a B-1 SPI rating (0.25μm). The process parameters for the 3D conical test pieces are shown in Table 4.17.

Table 4.17: Optimized parameters generated from model for the 3D cones

Coupon	Tip Radius (μm)	Desired Material Removal (μm)	Gap Distance (mm)	Conductivity of Solution (S/m)	Voltage (V)	Time (s)
1	50	0.206	19.72	2.15	1.00	22.92
2	50	0.232	20	2.99	1.38	28.15
3	85	0.224	20	4.42	3.81	16.52
4	85	0.216	12.97	1.60	1.25	12.54

The surface roughness of the tips of the cones before and after polishing is displayed in Figure 4.29. The calculated experimental error values are listed in Table 4.18.
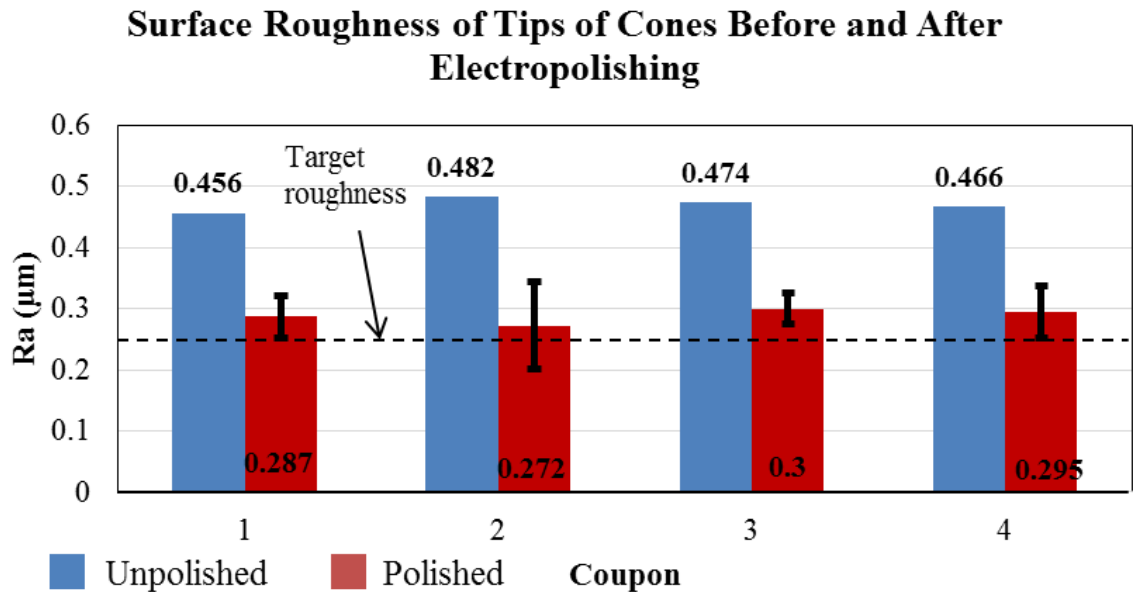
Figure 4.29: The surface roughness of the tips of the cone was reduced to an average R_a of 0.289 μm. The numerical values are the surface roughness values.

Table 4.18: Experimental error values for the conical polishing experiments

Coupon	Error (μm)
1	3.45E-02
2	7.07E-02
3	2.44E-02
4	4.30E-02

The model had an average error of and 0.038 μm when compared to the experimental results. The error can primarily be attributed to the calculated experimental uncertainties. In addition, the model assumed the array of cones to be arranged in straight lines. In reality, each row of cones were offset laterally from the previous row. The offset from row to row could have affected the charge density of neighboring cones differently than what was predicted in the COMSOL model.

4.7   Summary

A multiphysics model was developed to simulate an electropolishing process for micro-feature arrays. The COMSOL model was compared to Faraday's law of electrolysis and showed that Faraday's law is not sufficient when predicting material removal rates of high aspect ratio microfeatures. The simulation was used to develop a statistical model that was used to optimize and output process parameters based on microfeature geometry and desired material removal. The model was used to polish sample parts and micro-molds. Results showed that both the COMSOL model and Faraday's law underestimated the material removal rates exhibited during the experiments. COMSOL did however predict the trend that taller microfeatures will experience higher material removal rates. Possible sources of the error were attributed to the fact that the model did not consider molecular composition of the workpiece, grain structure and orientation, and surface charge densities in and out of plane.

CHAPTER 5

CASTING OPTICALLY TRANSPARENT MICRO-FEATURES

5.1   Introduction

Injection molding is commonly used process to enable high volume production of plastic parts. The benefits of using injection molding over hot embossing or direct machining pertain to the cost savings from low wastage and low process times. This is demonstrated through the face that injection molding utilizes the shortest process chain of the mentioned processes.

To show a proof-of-concept and feasibility, the molds were designed to be used for low pressure single cavity casting. Low pressure casting was utilized as only small quantities (~10) parts were to be fabricated and brass could still be utilized as the material for the molds. For injection molding, the material would have been changed to a mild steel or aluminum.

5.2   Mold Design

5.2.1   2D array Open Mold

The first mold design consisted of a two-part assembly. The drag was the brass piece that contained the microfeature geometry. The cope was a piece of aluminum that fit around the drag to form the cavity. Dowel pins were inserted and used to form the through holes in the part. The fully assembled mold is shown below in Figure 5.1.
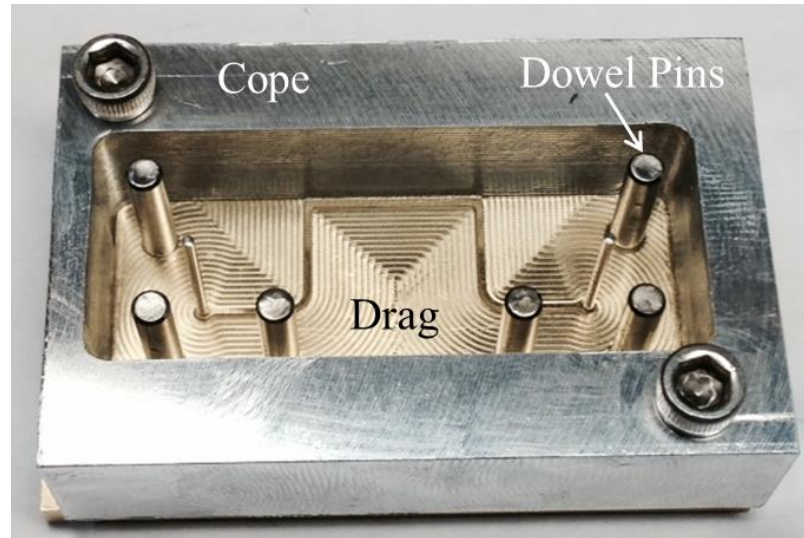
Figure 5.1: The assembled open mold was comprised of a cope, drag, and dowel pins.

The fully assembled mold created an open cavity where plastic resin was injected and allowed to cure. To aid in ejection of the part, a 1° draft angle was added to the cope to allow the part to slide out easier.

An issue that occurred while casting parts with the open mold was that the back surface was not flat. Due to capillary forces, the resin would adhere to the walls of the cope, in turn not creating a flat back surface.

5.2.2 2D array three part mold

In order to ensure the backside of the part was flat and had the best surface finish possible, a backplate was added to mold. The mold consisted of three parts: The drag, cope, and backplate. Having a separate backplate provided two advantages. The first was that it allowed for the backplate to be polished to a mirror finish with a buffing pad. Second, having three separate pieces still allowed the part to be ejected easily. If the mold was only two parts, ejection pins would have been required to release and push the cast part out of the mold cavity.

The drag contained the microfeature protrusions as well as a gate to allow for resin to be injected into the mold cavity. Dowel pins were inserted into the holes to form the through holes in the part. The drag is shown below in Figure 5.2.
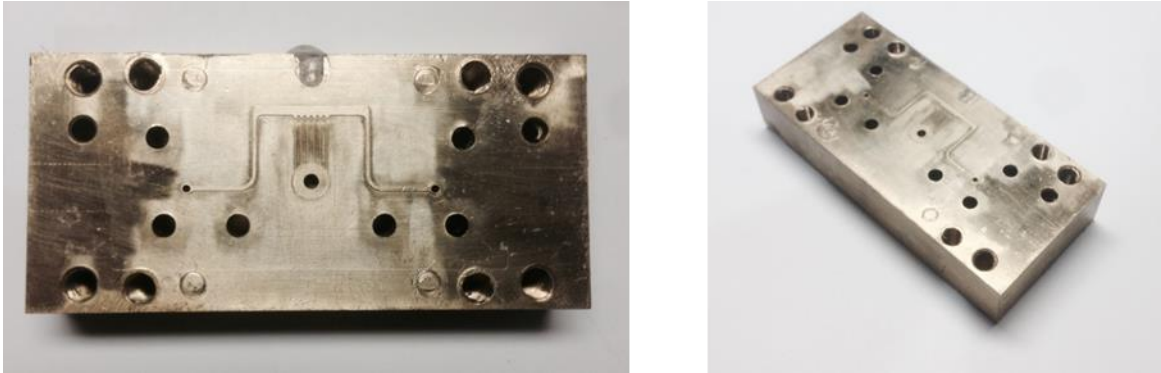
Figure 5.2: The drag contained the microfeature protrusions and holes for alignment and through hole features.

The cope was an 11 mm deep cavity machined out of a single piece of brass. A 1° draft angle cutting tool was used on the inner edges to allow for mold ejection. Alignment pins were used to ensure proper orientation between the drag and back plate. In addition, the cope also contained vents to allow air and bubbles to escape. The cope is shown below in Figure 5.3.
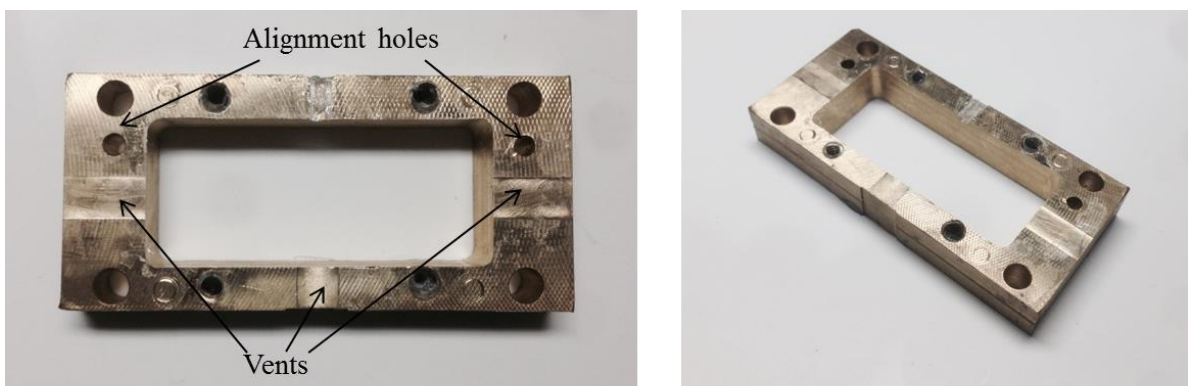
Figure 5.3: The cope was the middle piece of the mold that formed the cavity for the mold.

The backplate was machined flat to a surface roughness of 0.35 μm using a 2 mm 4 flute endmill. The backplate ensured the back face of the part was cast flat. By completely enclosing the cavity, both the front and back face of the part were able to be cast against flat polished surfaces, allowing for optimum surface finish. The backplate is shown below in Figure 5.4.
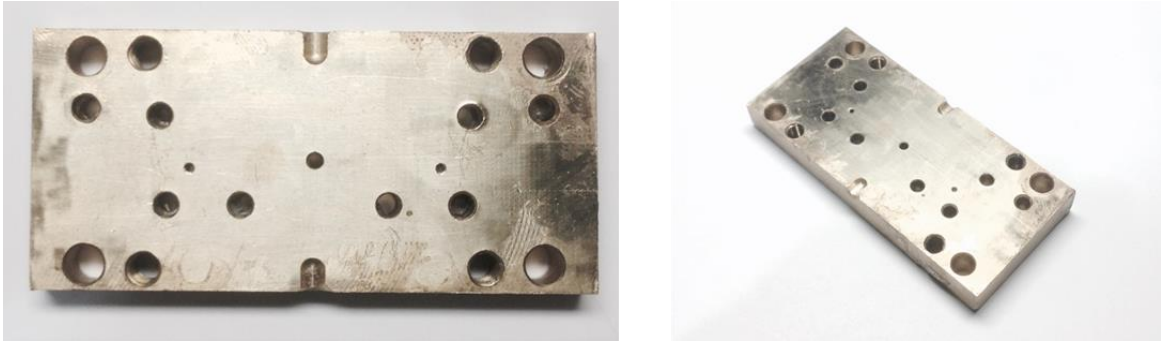
Figure 5.4: The backplate was flat piece that was polished to a mirror finish to fully enclose the mold and provide optimum surface finish for the part.

A gate was added to the top of the mold to allow for resin to be injected into the cavity. The assembly was fastened together using four 1.5 inch 10-32 screws, and 1 inch long dowel pins were inserted into the through holes afterwards to create the through hole features. The assembled parts of the closed mold are displayed in Figure 5.5.
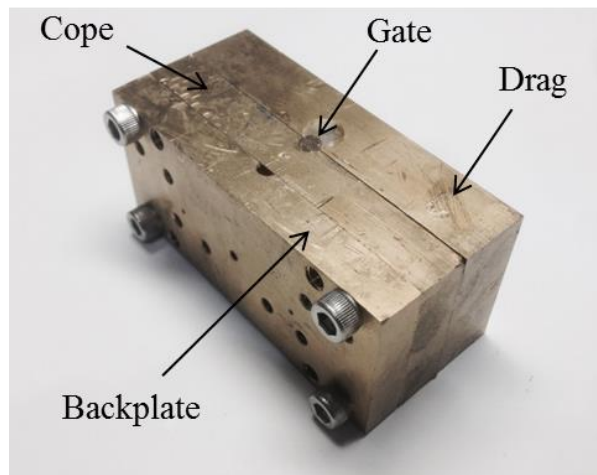
Figure 5.5: The three part mold was assembled and fastened with bolts and dowel pins.

5.2.3   3D conical array mold

Casting the 3D conical array provided more challenges than casting the 2D arrays. One challenge sprouted from the fact the part is only 0.5 mm thick while remaining 7 mm by 7 mm wide. This made it extremely fragile and hard to eject out of the mold. The other issue was orifices at the tips of the nozzles. Forming consistent 50 μm holes across the 31 nozzle array was a challenge.

Because the part was only 0.5 mm thick, a three part mold could not be used as it was too thin to fit a cope in between. Thus, a two part mold consisting of a drag and backplate was created. Ejection pins were placed in the corners of the mold cavity to release the part from the mold once cured. Images of the unassembled and assembled mold are shown below in Figure 5.6.
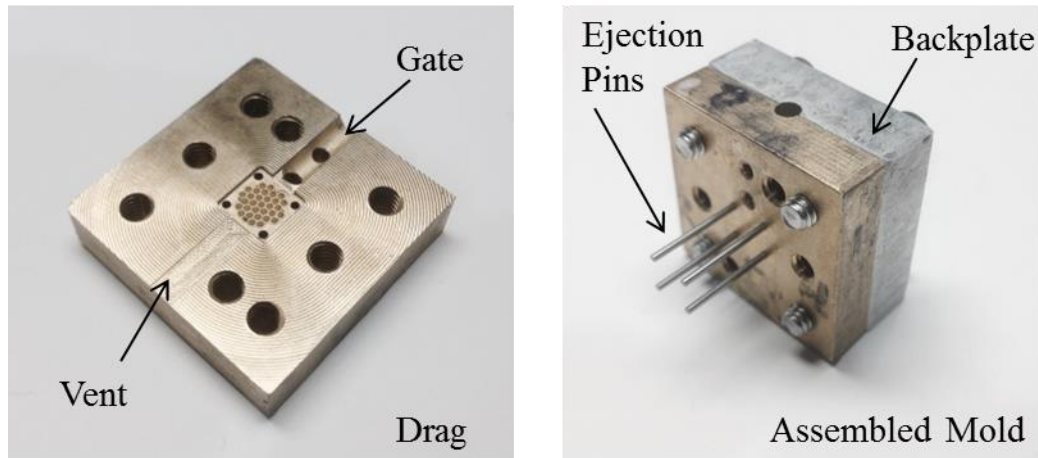
Figure 5.6: The mold for the 3D array was comprised of a drag and backplate. Because of thinness of the part, ejection pins were utilized to release the part.

In order to form the holes for the orifices, a seal between the tips of the cones and the surface of the backplate had to be formed. To ensure a seal was formed, a 0.01 mm interference fit between cones and the backplate was created. A diagram illustrating the interference fit is shown below in Figure 5.7.
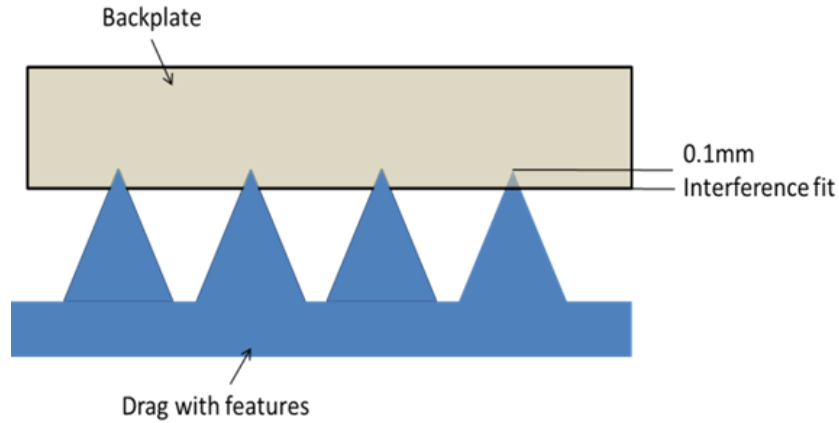
Figure 5.7: An interference fit between the tips of the cones and the backplate was created to ensure the orifices would be created during the molding process.

The interference fit was created by facing the mating surface of the drag and the tips of the cones at the same time. Afterwards, the material surrounding the cones was machined down another 0.01 mm. This ensured the tips of the cones were protruding 0.01 mm past the mating surface, creating a 0.01 mm interference with the back plate. The process is shown below in Figure 5.8.
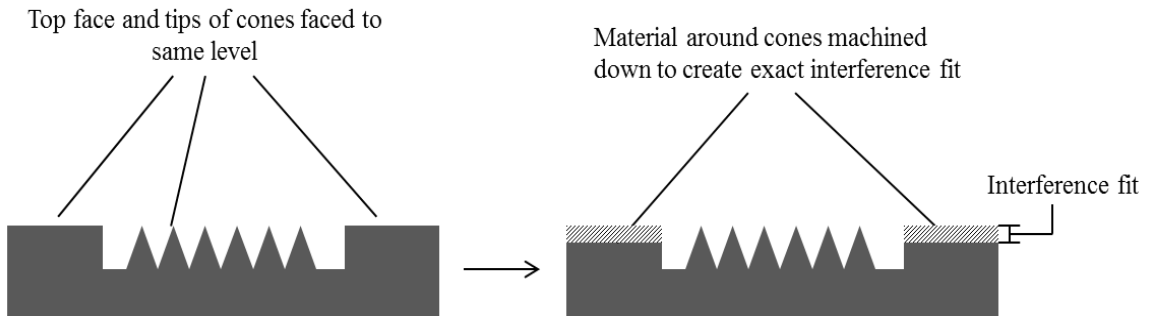
Figure 5.8: The interference fit was created by machining the tips of the cones

5.3 Low Pressure Casting

In order to explore and determine the optimum casting parameters for the parts, process parameters were varied and tested to minimize bubble propagation, maximize optical transparency, and create parts with the correct dimensional geometry. The process

parameters explored were the casting resin, curing pressure, and post-curing temperature. The specific process parameters are listed below in Table 5.1.

Table 5.1: Process parameters used during casting experimentation

Casting Resin	Curing Pressure (kPa)	Post-Curing Temperature (C)
PMMA (Acrylic)	Vacuum (0)	Ambient
Polyester	Ambient (101.3)	80
Urethane	Positive (241.3)	120

5.3.1 Materials and casting setup

The resins used to cast were a low viscosity (600 cps) urethane (Smooth On Crystal Clear-200), a polyester resin (TAP Clear-Lite casting resin), and casting Poly-methyl-methacrylate (Electron Microscopy Science Acrylic Plastic Casting). The resins were placed into a syringe and injected into the mold. Curing pressure was controlled through the use of a vacuum chamber (Fisher Scientific 01-060D) and weights placed on the plunger of the syringe. Post-curing temperature was controlled through the use of an oven (HAFO 1600).

5.3.2 Mold preparation

The machined molds were prepared and treated before casting by polishing and applying mold release to ensure proper surface finish and ease mold ejection. Soft polishing pads of 1200, 1500, and 2000 grit were incrementally applied to the backplate surfaces at 10,000 RPM. The process reduced surface roughness to a Ra of 0.05 μm. The smoother surface allowed for clearer and cleaner cast products.

Mold release was then applied to the casting surfaces of the molds to aid in mold ejection. Initially a liquid epoxy mold release (Slide Expoxease) was applied by spraying on a thin coat to the mold. Afterwards, compressed air was applied lightly to blow off any excess fluid that pooled on the surface. This method resulted in numerous small bubbles

on the surface of the cast because of the remnants from the mold release on the mold surface. To counter this effect, a bake-on mold release (Stoner A353 Endurance Mold Release) was utilized. A fine paintbrush was used to spread the mold release evenly on the surface, and then the mold was placed in an oven at 60°C for 15 minutes to bond the mold release to the surface as well was evaporate any excess fluid. This removed any residual mold release and created a cleaner surface which improved the clarity and reduced the number of bubbles in the cast.

5.3.3 Low pressure casting

Once the molds were assembled, the resins were prepared. The multiple parts of each resin were measured using a scale, and mixed together slowly for 90 seconds with a glass stirring rod. The resin was then poured into a syringe, and placed onto a fixture in a vacuum chamber to degas and remove any bubbles that were formed from mixing. The syringe was sealed at the bottom (tip) to prevent any leaks while degassing. The vacuum pump was left on for 5 minutes or until the resin began to foam up. The vacuum was then turned off and the resin sat in the chamber for a maximum of 10 minutes until the bubbles disappeared. Once degassed, the plunger was carefully inserted into the syringe. The syringe was then inserted into the mold and the resin was injected into the cavity. A vacuum was pulled again for 20 seconds to ensure proper filling. If the curing pressure was to be 0 kPa, then the vacuum would be left on. If the curing pressure was 35 kPa, a 5 kg weight was placed on top of the syringe to hold the positive pressure. A diagram of the setup and the actual experimental setup is shown in Figure 5.9.
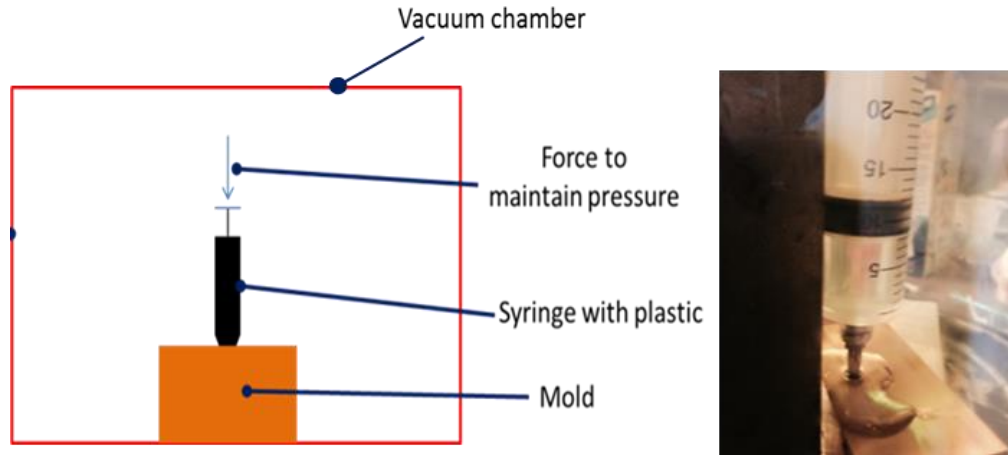
Figure 5.9: The plastic resin was injected into the mold and was kept under a vacuum chamber. A weight was placed on top of the plunger to maintain pressure if necessary.

The molds were then left to cure overnight. After done curing for 24 hours, they were placed in an oven for 60 min to postcure. Postcuring at higher temperature ensured the resin came out rigid as well as enhanced the optical clarity of the cast compared to curing at room temperature.

5.4   Casting Results

Once the molds were finished curing and the parts were ejected, they were viewed under the microscope to validate dimensions as well as observe if the piece was optically transparent. Parts were deemed transparent if the features were visible from the back side when viewed under the microscope. The parts were also checked for bubbles and voids, as those would hinder performance of the part. The Urethane produced the most optically clear pieces with correct dimensions followed by the PMMA and the Polyester. A comparison of the three resins' results is shown in Figure 5.10. A summary of the results of varying curing pressure and postcuring temperature are broken down and displayed in Figure 5.2 and Table 5.3.

Urethane	PMMA	Polyester

- Most transparent with correct geometry transfer
- Appeared and felt glass-like. Bubbles were mitigated due to its low viscosity (600 cps)
- Overall produced the best parts

- Produced correct dimensions and geometry
- Contained larger bubbles and voids compared to the urethane because of it's higher viscosity
- Not as transparent as Urethane

- Parts were hazy and translucent, not allowing visibility through the piece.
- The cast parts were extremely brittle and often times cracked and fractured when ejected from the mold.
- Critical dimensions were not held as there was noticeable shrinkage, particularly around the 0.1 mm microchannels

Figure 5.10: A comparison of the resins showed that Urethane produced the best parts in terms of clarity, geometric replicability, and stiffness.

Table 5.2: The effects of curing pressure on cavity filling and bubble propagation

	Curing pressure (kPa)	Filled Cavity	Bubble (Number and size)
PMMA	0	Voids at the top	1-10 (1mm)
	101.3	Yes	1-10 (1mm)
	241.3	Yes	none
Polyester	0	Voids at the top	1-10 (up to 2 mm)
	101.3	Yes	11-20 (up to 2 mm)
	241.3	Yes	none
Urethane	0	Voids at the top	50+ (up to 4 mm)
	101.3	Yes	20-50 (up to 2 mm)
	241.3	Yes	1-10 (1 mm)

Table 5.3: The effects of post-curing temperature on clarity and surface finish of the cast parts.

	Oven Temp (°C)	Validation of Dimension	Rigidity	Optical Clarity	Surface Finish
PMMA	20	No	Amorphous	No	Wavy and warped
	80	Yes	Rigid (holds form under pressure	Yes	Flat and smooth
	120	Yes	Stiff and brittle	No	Burnt with bubbles
Polyester	20	No	Amorphous	No	Wavy and warped
	80	No	Stiff and brittle	Yes	Flat and smooth
	120	No	Stiff and brittle	No	Burnt with bubbles
Urethane	20	No	Amorphous	Yes	Wavy and warped
	80	Yes	Rigid (holds form under pressure	Yes	Flat and smooth (glass like)
	120	Yes	Rigid (holds form under pressure	Yes	Flat and smooth (glass like)

Both the 2D array and the 3D array parts were cast successfully using the urethane under positive pressure with a post-cure for 1 hour at 80°C. The final parts are shown in Figure 5.11 through Figure 5.13.

2D array   3D array
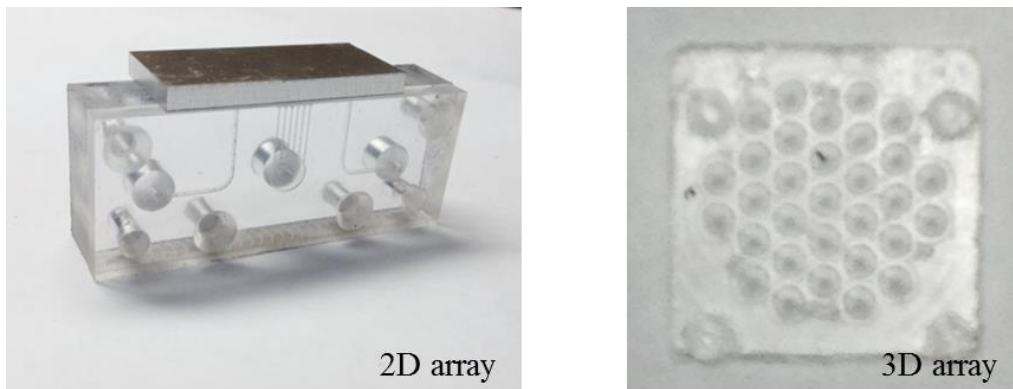
Figure 5.11: The 2D and 3D microfeature parts were cast successfully while retaining optical clarity.
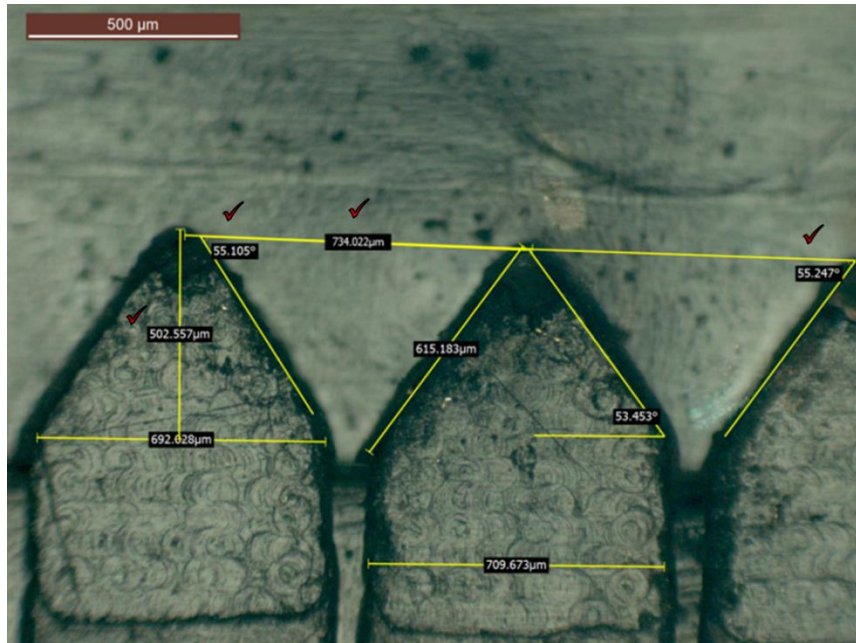
Figure 5.12: The dimensions of the 2D cast parts were verified under a microscope.
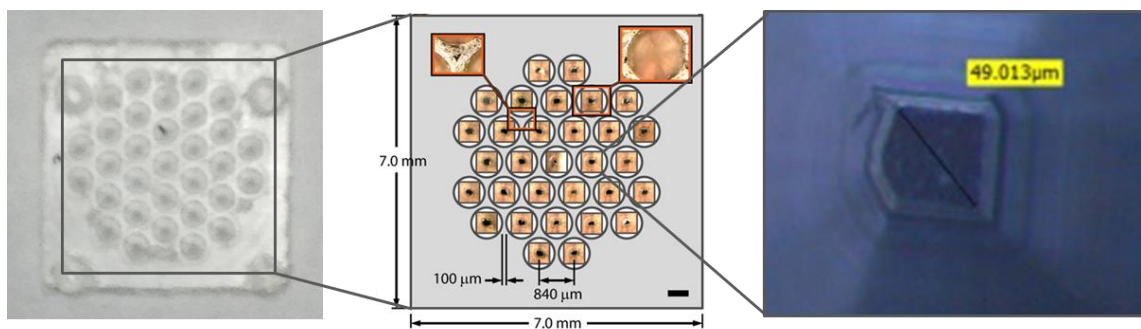
Figure 5.13:The orifice hole geometry was transferred correctly into the cast parts for the 3D nozzle array.

5.5   Discussion of Casting Results

5.5.1   Effects of casting pressure

The curing pressure used in the closed mold significantly affected the number of bubbles in the final part as well as affected how well the mold cavity was filled. The PMMA and polyester produced the best parts when under positive pressure. The mold cavity was able to be completely filled and no bubbles were apparent. Under a vacuum, large voids were left at the top of both resins' casts as well as some small bubbles scatter

throughout the parts. Voids were possibly caused by some resin leaking out from the vents due to the vacuum, and the resin in the gate curing before any more could be pulled from the syringe. An example of a void is shown below in Figure 5.14.
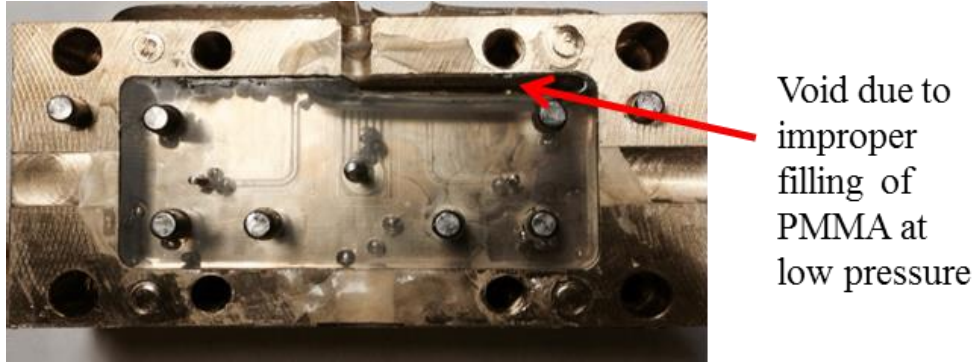
Figure 5.14: Casting at lower pressures caused voids to occur because the resin could not fill the mold cavity.

The Urethane also performed best under positive pressure, as very few bubbles appeared, and the mold cavity was filled. When placed under a vacuum, many more bubbles appeared. A comparison of casting pressures and bubble propagation is illustrated in Figure 5.15.
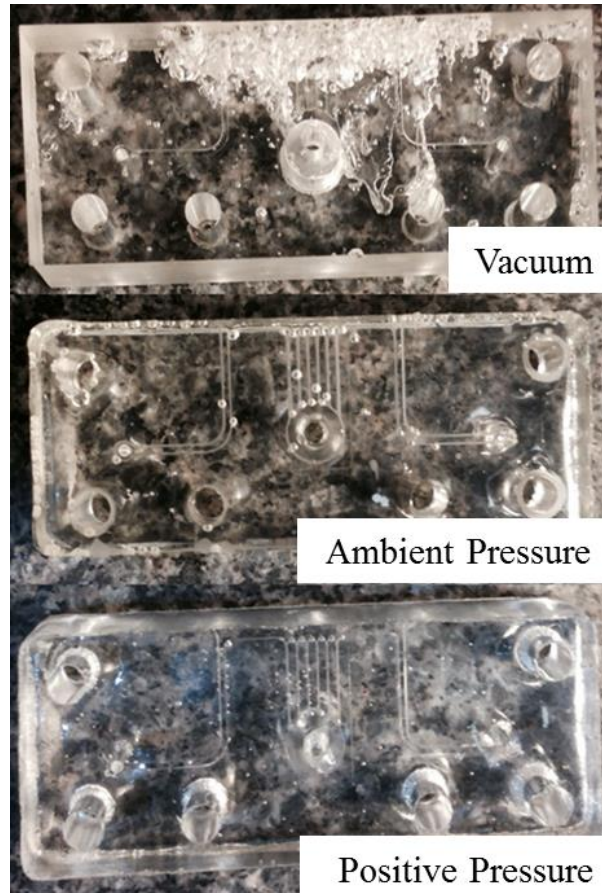
Figure 5.15: As the curing pressure increase, the bubble propagation in the part decreased.

The bubble propagation was explained by the chemical reaction that the urethane undergoes during its curing process. As the urethane polymerizes, carbon dioxide is released as by product. At higher pressures, this gas is more soluble in the resin preventing bubbles to form [51]. While the curing pressure affected the bubble propagation in the urethane, it had no effect on the transparency.

The data provide ample evidence that higher pressure yields less bubble propagation. Thus, it is possible to say that with injection molding, bubble propagation should not be a significant issue as the injection pressures can reach 32,000 psi (Sumitomo SG75). The high pressure involved with injection molding will ensure fully filled cavities and mitigate bubble formation.

5.5.2 Effects of post-curing temperature

The optimal oven curing temperature for PMMA, Polyester, and Urethane was 80°C. This temperature yielded parts that remained firm and rigid when ejected. When no oven post cure was applied the parts were amorphous and deformed while handling. At 120°C, the parts were extremely hard and brittle, and often times would fracture during the mold ejection process. Also, at 120°C, the polymers burnt on the surface and developed bubbles due to pyrolysis.

Figure 5.16: Parts post-cured at 120°C experienced pyrolysis and became extremely brittle, often breaking during the mold release.

The optical transparency varied between the three polymers. PMMA achieved optical transparency at 80°C. With no postcuring heat applied, the surface was translucent and hazy. At 120°C, the surface was blackened and burnt. The polyester resin achieved its best optical clarity at 80°C as well. The oven temperature had no effect on the urethane's optical transparency, as it always obtained a glass like clarity. The urethane produced the cleanest and clearest images under the microscope compared to the other two resins.

Both the PMMA and urethane replicated the correct geometry and dimensions. The polyester experienced shrinkage effects that caused the high aspect ratio 0.10 mm wide microchannel features to deform.

5.5.3 Mold ejection

Dividing the mold into three parts proved to be an effective strategy for both mold ejection as well as maintaining clear flat surfaces on the front and back faces of the part for the 2D arrays. Ejecting the part out of the mold for the 3D array was challenging. Even with mold release, the part often broke when released due to how thin and brittle it was. To counter this issue, the mold was taken apart and placed in the oven at 60°C for 5 minutes to heat the plastic and have the mold expand. In doing so, the part was less brittle and easier to eject.

5.5.4 Scalability of low pressure casting

In order to scale this low cost process up for larger batch productions, multiple cavity molds could be introduced to allow for more parts to be cast simultaneously. Also, simple automation with lead screws and stepper motors could be implemented to facilitate resin mixing and injection, as well as hold constant pressure during the curing process in more robust and repeatable fashion. It is important to note that low pressure casting was used as a stepping stone and proof of concept for injection molding. It is entirely possible and understandable to scale up directly to injection molding for higher volume production.

5.6 Summary

Molds were designed and machined for both the 2D and 3D microfeature arrays. A low pressure casting setup was developed as a cost alternative to injection molding. Different polymers, casting pressures and post curing temperatures were explored to determine which would yield the best parts. Casting urethane under positive pressure and post-curing at 80°C produced parts with correct geometry and optical transparency. The 3D conical mold utilized an interference fit to ensure the formation of the orifices in the

microfeature array. The final parts were checked and validated for dimensional accuracy and consistency throughout the microfeature arrays.

CHAPTER 6

CONCLUSIONS

6.1   Summary and Conclusions

The work presented in this thesis addressed the need for the development of a scalable manufacturing process for optically transparent microfeatures. A set of biomedical MEMS devices was used as a case study to test and experiment with the proposed processes. The devices required micro-feature arrays were to act as nozzles to focus ultrasonic waves to aid in cell transfection. The geometries required consisted of planar protrusions as well as 3D conical arrays, and were to be optically transparent to allow for visual inspection through a microscope. Dimensions, as small as 50 μm diameters, were required to be fabricated for the parts. The process developed involved the micro-milling of a mold, the polishing of the mold, and injection molding. To show proof of concept of the process, brass molds were machined, polished, and used for low pressure casting. Micro-milling tools and techniques were utilized to machine the micro-feature geometries into brass. An error propagation analysis was performed to explore and illustrate the challenges involved with fabricating and assembling microfeature components.

After the molds were machined, they were polished through electropolishing. A computational and statistical model was developed to optimize and generate process parameters to polish the mold surface to a roughness of 0.25 μm. Experimentation was performed and showed that the model successfully reduced surface roughness of the features from R_a values as high as 2.369 μm down to R_a values as low as 0.266 μm with an average experimental error of .04 μm. The study also showed that Faraday's law is

not the most accurate method for predicting material removal for high aspect ratio microfeatures. The COMSOL model predicted that the higher material removal rates would occur at the tops of the features, but underestimated the magnitude of the material removal. The COMSOL model was more accurate than Faraday's Law at predicting material removal at higher parts of the microfeatures. Estimation errors were attributed to the anisotropy and scaling effects of grain size of the microfeatures.

The polished molds were used for low pressure casting. Experimentation showed that urethane cast under positive pressure along with post cure at 80°C yielded transparent parts with correct geometry. The brass molds for the 3D conical geometry only were able to produce 10 cast parts before needing to be remachined due to the tips of the cones being damaged from the interference fit. Low pressure casting proved to be a stepping stone and proving grounds for injection molding. Based on the results from the present, the final proposed process chain to for high volume production of optically transparent materials is displayed below in Figure 6.1.
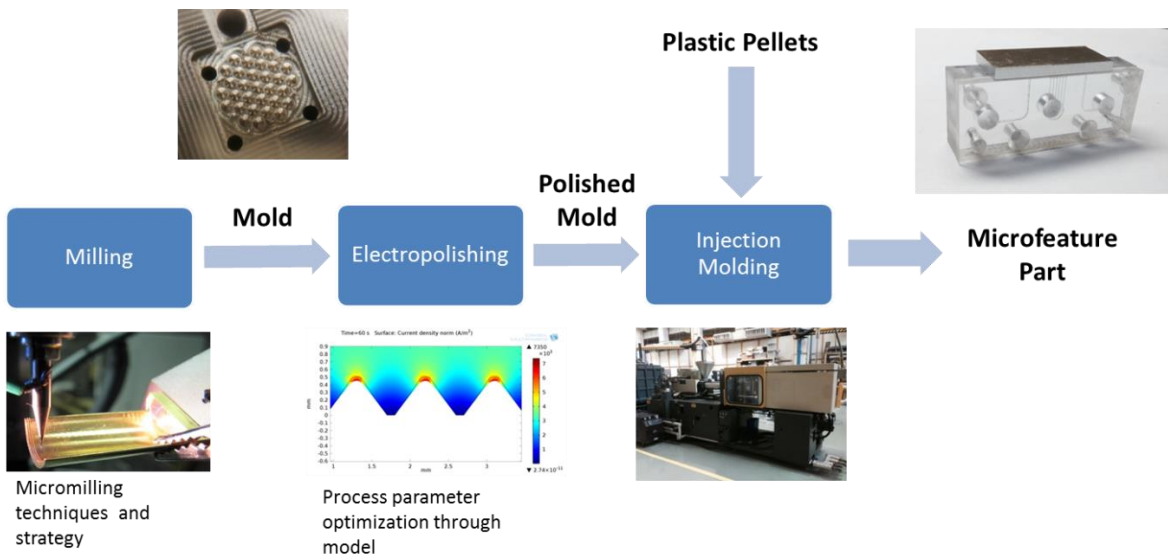
Figure 6.1: Proposed process chain for high volume production of transparent microfeatures.

Pursuant to work summarized here and presented in the previous chapters, the following conclusions can be made:

- Direct machining into plastic is not an effective method to produce optically transparent microfeatures.

- Finite element modeling of electropolishing predicted material removal 15.67% more accurately than Faraday's law fo electropolishing of the microfeature arrays.

- Modeling just the geometry and surface charge density is not sufficient to accurately predict material removal of microfeature arrays due to scaling affect with grain size.

- Low pressure casting is a viable low cost alternative for low unit production of optically transparent micro-feature parts.

6.2   Contributions

Pursuant to the work presented in the previous chapters, the following contributions were made:

- A micro-machining strategy for non-uniform microfeature arrays through the utilization of high-speed spindles and micro tools fitted on standard CNC mills.

- A modeling approach to aid in the prediction of material removal rates during the electropolishing of microfeatures.

- A casting method for low unit production of polymer parts without the use of expensive industrial equipment.

- The following papers have been published:

1. Nishant Srinivasan, J. Rhett Mayor, "Microfeature Production in Optically Transparent Materials," International Workshop for Microfactories, October 5-8, 2014.

2. Nishant Srinivasan, J. Rhett Mayor, "Superfinishing of Microfeature Arrays using Electrochemical Techniques," International Workshop for Microfactories, October 5-8, 2014.

3. Nishant Srinivasan, J. Rhett Mayor, "Design for Micromanufacturing: A Scaling Study on Tolerance Analysis," International Conference on Micromanufacturing, March 31 – April 2, 2015.

6.3 Recommendations and Future Work

Possible future extensions of this work were identified during the course of this study. The paths are presented here as recommendations for future work.

- Direct machining of transparent plastic using cryogenics

The preliminary machining study in the introduction showed that direct machining plastics is challenging due to its material properties. By cooling the working piece to cryogenic temperatures, the plastic would become more brittle and could aid in chip formation during micromachining. The new process could enable another pathway for low volume production of plastic microfeatures.

- Microfeature production in hard metals for injection molding

The work in this study focused on machining brass molds to identify the plausibility for injection molding as a possible pathway towards high volume production. In order to move towards injection molding, machining the microfeatures into a harder metal such as a mild steel or nickel could be attempted. Tools such as a plunge EDM could be utilized

to machine the hard metal. The molds could then be tested under high pressure injection molding machines to determine the quality and replicability of the microfeature parts.

- Further modeling and prediction for electropolishing of microfeatures

The effects of grain structure and anisotropy were not accounted for in the COMSOL model. Work could be done to explore the effects grain orientation and size on material removal rates for microfeature arrays. The knowledge could then be incorporated into the model to aid in material removal prediction. Furthermore, the micromachining could be optimized to generate desired grain structures to aid in electropolishing and optimize surface roughness.

APPENDIX A

PRELIMINARY DEVICE FABRICATION STUDY

This appendix details the work performed to direct machine the micro-feature geometry in plastic. The first method utilized to fabricate the part was the direct machining of the features into polycarbonate. For single unit production, this was the fastest and cheapest form of fabrication. Micromilling techniques were used to machine pockets to form the features into the polycarbonate.

A.1   Direct machining plastic

The primary challenge with machining optically clear materials is that it is difficult to tune the spindle speed and feedrates. The two most common optically clear materials are glass and plastic. Machining glass is difficult as it is extremely brittle and takes too long to etch. Plastic is on the other end of the spectrum; as it gets hot while machining it becomes ductile and deforms, thus making it hard to produce chips. The effect of temperature on the toughness of plastic is shown below in Figure A.6.2 [10].
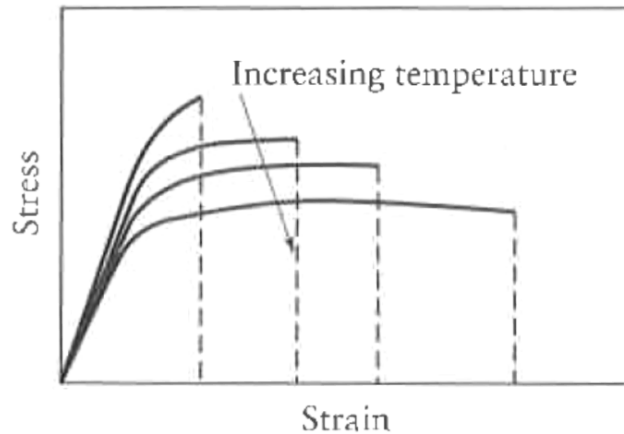
Figure A.6.2: Increasing temperatures affects the modulus of elasticity and overall toughness

A 3-axis CNC mill (Prototrak DPM SX2) coupled with a 150000 RPM air spindle (Nakanishi HTS15001S-M2040) was used to machine the microfeatures. Two flute micro-endmills were used to machine the nozzle and microchannel features. All tools used an electronic touch off method to register and zero the Z-Axis. A precision gage block was used as an offset for nonconductive plastic parts. The tools, speeds and feeds used to machine the features are listed in Table A.6.1.

Table A.6.1: Micromilling feeds, speeds and tool size for direct machining

Order used	Diameter (mm)	Spindle Speed (RPM)	Feedrate (mm/min)	Feature created
1	.100	150000	250	Nozzles and channels
2	.500	150000	300	0.5 mm width channels
3	.794	150000	500	Microchannels (only used on mold)

A.2   Direct Machining Results

Machining into plastic proved not to be a viable solution, as critical dimensions could not be held. The angles of the nozzle shaped features were 45° instead of 54°, and the tips of the features were blunt and rounded points instead of sharp edges. The errors are attributed to the heat generation during the process. The tool began to melt and deform the plastic due to the high speed and slow feedrate. Also, there was some tool deflection at the corners of the nozzles which prevented the tool from creating sharp edges. Upon inspection, the final machined surface contained burr, appeared hazy, and was not optically transparent through the microscope. To compare the challenges of direct machining plastic, the same features were machined into brass utilizing the same strategy as stated prior. The features were placed under a microscope to measure their dimensions. The features machined into brass had straighter edges, fewer burr, correct 54° angle, and were overall more consistent across the array. A comparison between machining the brass and plastic is shown below in Figure A.6.3.
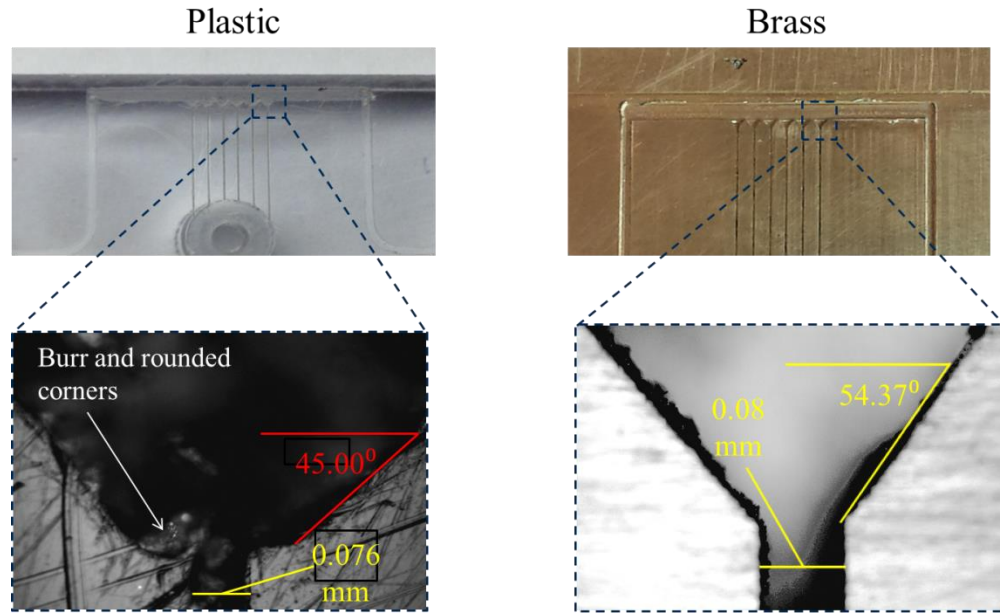
Figure A.6.3: Direct machining plastic yielded poor results, as dimensions could not be held and optical clarity was lost. Machining brass yielded correct dimensions with sharp edges.

The difference between machining the two materials is due to the endmill and workpeice getting extremely hot during the machining process. As the polycarbonate heated up during the process, the energy required to fracture increased much more so than when machining the brass. Thus the tool could not cut the plastic as cleanly and formed the errors.

A.3   Summary and next steps

The direct machining of plastic was a vital step in the progression of the development of a sustainable manufacturing process. Results proved that direct machining plastic is not a viable process. Machining brass provided positive results, and lead to the possibility of machining a mold to cast the part in resin.

REFERENCES

[1]   S. A. Semidey and J. R. Mayor, "Experimentation of an electric machine technology demonstrator incorporating direct winding heat exchangers," *IEEE Transactions on Industrial Electronics,* vol. 61, pp. 5771-5778, 2014.

[2]   B. M. Senderling, H. M. Mortell, J. L. Cezeaux, R. T. Gettens, and M. J. Rust, "Design of a microfeature scaffold for tissue engineering," in *2011 37th Annual Northeast Bioengineering Conference (NEBEC 2011), 1-3 April 2011*, Piscataway, NJ, USA, 2011, p. 2 pp.

[3]   G. Yuan, R. Yun-Jiang, G. Yu, W. Yu, and R. Zeng-Ling, "Micro fiber-optic Fabry-Perot interferometer fabricated by chemical etching of Er-doped fiber," in *20th International Conference on Optical Fibre Sensors, 5 Oct. 2009*, USA, 2009, p. 75033A (4 pp.).

[4]   E. J. Tremblay, R. D. Beer, A. Arianpour, and J. E. Ford, "Telescopic vision contact lens," in *Ophthalmic Technologies XXI, 22-24 Jan. 2011*, USA, 2011, p. 788510 (8 pp.).

[5]   E. J. Tremblay, I. Stamenov, R. D. Beer, A. Arianpour, and J. E. Ford, "Switchable telescopic contact lens," *Optics Express,* vol. 21, pp. 15980-15986, 2013/07/01 2013.

[6]   Microunit, "Glass microreactor chip," Glass-microreactor-chip-micronit.jpg, Ed., ed, 2006.

[7]   L. D. C. Casa and D. N. Ku, "High Shear Thrombus Formation under Pulsatile and Steady Flow," *Cardiovascular Engineering and Technology,* vol. 5, pp. 154-163, 2014.

[8]   L. Hyun Ho and P. Yager, "Microfluidic Lab-on-a-chip for Microbial Identification on a DNA Microarray," *Biotechnology and Bioprocess Engineering,* vol. 12, pp. 634-9, 12/ 2007.

[9]   V. G. Zarnitsyn, J. M. Meacham, M. J. Varady, H. Chunhai, F. L. Degertekin, and A. G. Fedorov, "Electrosonic ejector microarray for drug and gene delivery," *Biomedical Microdevices,* vol. 10, pp. 299-308, 04/ 2008.

[10]   S. S. S. Kalpakjian, *Manufacturing Processes for Engineering Materials*, 4th ed., 2003.

[11]   D. R. D Rosato, M Rosato, *Injection Molding Handbook*: Springer Science & Buisness Media, 2000.

[12]   T. Lomas, S. Mongpraneet, A. Wisitsoraat, K. Jaruwongrungsee, A. Sappat, T. Maturos*, et al.*, "Low cost hot embossing process for plastics microfluidic chips fabrication," in *2009 6th International Conference on Electrical Engineering/Electronics, Computer,*

Telecommunications and Information Technology, ECTI-CON 2009, May 6, 2009 - May 9, 2009, Chonburi, Thailand, 2009, pp. 462-464.

[13]	J. M. Meacham, "A Micromachined Ultrasonic Droplet Generator: Design, Fabrication, Visualization, and Modeling," Mechanical Engineering, Georgia Institute of Technology, 2006.

[14]	R. M. DJ Lipomi, LCademartiri, GM Whitesides, "Soft Lithographic Approaches to Nanofabrication," presented at the Harvard University, 2012.

[15]	C. A. Mills, E. Martinez, A. Errachid, E. Engel, M. Funes, C. Moormann*, et al.*, "Nanoembossed polymer substrates for biomedical surface interaction studies," 25650 North Lewis Way, Stevenson Ranch, California, 91381-1439, United States, 2007, pp. 4588-4594.

[16]	J. Friend and L. Yeo, "Fabrication of microfluidic devices using polydimethylsiloxane," *Biomicrofluidics,* vol. 4, 2010.

[17]	J. C. Lotters, W. Olthuis, P. H. Veltink, and P. Bergveld, "Mechanical properties of the rubber elastic polymer polydimethylsiloxane for sensor applications," *Journal of Micromechanics and Microengineering,* vol. 7, pp. 145-147, 1997.

[18]	T. S. Hug, T. Biss, N. F. de Rooij, and U. Staufer, "Generic fabrication technology for transparent and suspended microfluidic and nanofluidic channels," in *TRANSDUCERS '05. The 13th International Conference on Solid-State Sensors, Actuators and Microsystems. Digest of Technical Papers, 5-9 June 2005*, Piscataway, NJ, USA, 2005, pp. 1191-4.

[19]	J. Vivanco, B. Smith, A. Blake, J. Williams, K. Turner, and H. Ploeg, "3D elastomeric scaffolds fabricated by casting in micro end milled moulds," *Journal of Biomimetics, Biomaterials, and Tissue Engineering,* vol. 9, pp. 17-23, / 2011.

[20]	Y.-c. Wang, D. Xie, and H.-h. Zhang, "Manufacture of microlens arrays based on contactless embossing," *Mechanical & Electrical Engineering Magazine,* vol. 27, pp. 13-16, 11/ 2010.

[21]	C. Iliescu, H. Taylor, M. Avram, J. Miao, and S. Franssila, "A practical guide for the fabrication of microfluidic devices using glass and silicon," *Biomicrofluidics,* vol. 6, p. 016505 (16 pp.), 03/ 2012.

[22]	W. Pfleging, R. Kohler, P. Schierjott, and W. Hoffmann, "Laser patterning and packaging of CCD-CE-Chips made of PMMA," *Sensors and Actuators, B: Chemical,* vol. 138, pp. 336-343, 2009.

[23]	K. Sugioka, K. Obata, M. H. Hong, D. J. Wu, L. L. Wong, Y. F. Lu*, et al.*, "Hybrid laser processing for microfabrication of glass," *Applied*

Physics A (Materials Science Processing), vol. A77, pp. 251-7, 07/ 2003.

[24]   E. Brinksmeier, O. Riemer, A. Gessenharter, and L. Autschbach, "Polishing of structured molds," *CIRP Annals - Manufacturing Technology,* vol. 53, pp. 247-250, 2004.

[25]   T. L. Perry, D. Werschmoeller, X. Li, F. E. Pfefferkorn, and N. A. Duffie, "The effect of laser pulse duration and feed rate on pulsed laser polishing of microfabricated nickel samples," *Journal of Manufacturing Science and Engineering, Transactions of the ASME,* vol. 131, pp. 0310021-0310027, 2009.

[26]   H. Suzuki, R. Kawamori, M. Miyabara, T. Okino, Y. Hijikata, Y. Yamamoto*, et al.*, "Ultra-precision finishing of micro aspherical surface by ultrasonic vibration assisted polishing," *Key Engineering Materials,* vol. 291-292, pp. 349-54, / 2005.

[27]   G. Tlusty, *Manufacturing and Process*, 1 ed. Upper Saddle Rive, NJ: Prentice Hall, 2000.

[28]   B. H. Kim, C. W. Na, Y. S. Lee, D. K. Choi, and C. N. Chi, "Micro electrochemical machining of 3D micro structure using dilute sulfuric acid," *CIRP Annals - Manufacturing Technology,* vol. 54, pp. 191-194, 2005.

[29]   Y. H. Jeong, B. HanYoo, H. U. Lee, B.-K. Min, D.-W. Cho, and S. J. Lee, "Deburring microfeatures using micro-EDM," *Journal of Materials Processing Technology,* vol. 209, pp. 5399-5406, 2009.

[30]   S. Kissling, K. Bade, M. Borner, and D. M. Klymyshyn, "Electropolishing as a method for deburring high aspect ratio nickel RF MEMS," Tiergartenstrasse 17, Heidelberg, D-69121, Germany, 2010, pp. 1361-1367.

[31]   T. Gietzelt, L. Eichhorn, and K. Schubert, "Material and micromachining aspects of manufacturing micromolds for replication techniques," *Advanced Engineering Materials,* vol. 8, pp. 33-37, 2006.

[32]   V. K. Jain, S. Kalia, A. Sidpara, and V. N. Kulkarni, "Fabrication of micro-features and micro-tools using electrochemical micromachining," The Guildway, Old Portsmouth Road, Artington, Guildford, GU3 1LP, United Kingdom, 2012, pp. 1175-1183.

[33]   A. Bhuyan, B. Gregory, H. Lei, Y. Y. Seow, and Y. B. Gianchandani, "Pulse and DC electropolishing of stainless steel for stents and other devices," in *Fourth IEEE Conference on Sensors 2005, October 31, 2005 - November 3, 2005*, Irvine, CA, United states, 2005, pp. 314-317.

[34] E. J. F. Dickinson, H. Ekstrom, and E. Fontes, "COMSOL Multiphysics: Finite element software for electrochemical analysis. A mini-review," *Electrochemistry Communications,* vol. 40, pp. 71-74, 2014.

[35] C.-J. Kim, J. R. Mayor, and J. Ni, "A static model of chip formation in microscale milling," *Journal of Manufacturing Science and Engineering, Transactions of the ASME,* vol. 126, pp. 710-718, 2004.

[36] "General Machining Guidlines," ed: Harvey Tool, 2015.

[37] C. Zwyssig, J. W. Kolar, and S. D. Round, "Megaspeed drive systems: Pushing beyond 1 million r/min," *IEEE/ASME Transactions on Mechatronics,* vol. 14, pp. 564-574, 2009.

[38] A. A. Sodemann and J. R. Mayor, "Parametric investigation of precision in tool-workpiece conductivity touch-off method in micromilling," in *37th Annual North American Manufacturing Research Conference, NAMRC 37, May 19, 2009 - May 22, 2009*, Greenville, SC, United states, 2009, pp. 565-572.

[39] G. Tlusty, *Manufacturing Process and Equipment*. Upper Saddle River, NJ: Prentice Hall, 2000.

[40] R. Pryor, *Multiphysics Modeling Using COMSOL: A First Principles Approach*, 1 ed. Sudbury, Ma: Jones and Bartlett Learning, 2009.

[41] T. R. Briggs, "Electrolytic Solution and Deposition of Copper," in *American Electrochemical Society*, Lake Placid, 1922, p. 84.

[42] G. E. Box, Hunter, W.G., and Hunter, S.J., *An Introduction to Design, Data Analysis, and Model Building*: John Wiley & Sons, 1978.

[43] A. V. Wolf, *Aqueous Solutions and Body Fluids*. New York: Harper and Row, 1966.

[44] T. Matsumura, T. Konno, S. Tobe, and T. Komatsu, "Deburring of micro-scale structures machined in milling," in *ASME 2010 International Manufacturing Science and Engineering Conference, MSEC 2010, October 12, 2010 - October 15, 2010*, Erie, PA, United states, 2010, pp. 105-112.

[45] R. H. Myers, *Classical and Modern Regression with Applications*, 2nd ed.: Duxbeury Press, 1990.

[46] S. J. Kline and F. A. McClintock, "Describing uncertainties in SingleSample experiments," *Mechanical Engineering,* vol. 75, p. 38, 1953.

[47] H. Seidel, *Journal Electrochemical Society,* pp. 3612-3626, 1990.

[48] J. Matsumoto, H. Anada, and M. Furui, "The effect of grain size and amount of phase on the properties of back-torsion working in 60/40 brass," in *5th International Conference on Processing and*

Manufacturing of Advanced Materials - THERMEC 2006, July 4, 2006 - July 8, 2006, Vancouver, BC, Canada, 2007, pp. 661-666.

[49] R. i. Murakami, K. Nakane, and K. Akizono, "Influence of grain size on near threshold fatigue crack grow   th behavior in 60-40 brass," *Journal of the Society of Materials Science, Japan,* vol. 32, pp. 389-94, 04/ 1983.

[50] X. D. Cao, B. H. Kim, and C. N. Chu, "Micro-structuring of glass with features less than 100 m by electrochemical discharge machining," *Precision Engineering,* vol. 33, pp. 459-465, 2009.

[51] V. P. Sarzhevskaya, K. A. Kornev, S. E. Lysobyk, and N. I. Shchepetkina, "Polyester urethane casting compositions with long pot life," *Plasticheskie Massy,* pp. 44-46, 1968.